

**Applications of Semiclassical Theory in Statistical and
Quantum Mechanics**

**A THESIS
SUBMITTED TO THE FACULTY OF THE GRADUATE SCHOOL
OF THE UNIVERSITY OF MINNESOTA
BY**

Michael Janas

**IN PARTIAL FULFILLMENT OF THE REQUIREMENTS
FOR THE DEGREE OF
DOCTORATE OF PHILOSOPHY**

Professor Alex Kamenev

June, 2018

© Michael Janas 2018
ALL RIGHTS RESERVED

Acknowledgements

I first and foremost want to thank my advisor Alex Kamenev for his continued support, encouragement, and above all patience as I have progressed throughout graduate school.

I want to thank my fellow graduate students for their help in this process. in particular, I'm grateful to my collaborators Tobias Gulden, Peter Koroteev, Yuting Wang, and Baruch Meerson for keeping me focused and engaged on our common projects.

I also want to thank Dan Cronin-Hennessy, Michel Jansson, and Aleksey Cherman for their intellectual contributions and personal encouragement.

Outside of the department, I am grateful to Mary Roske-Groth and Brianna Verheyen at the Boynton Mental Health Clinic, for helping me to continue progress on a more stable trajectory.

Finally, I want to thank my parents Robert and Lorita Janas for supporting me through these last eight years in graduate school.

Dedication

To the staff at Al's Breakfast, for many days of great food, coffee, and conversation

Abstract

Since the initiation of quantum theory in the early 20th century, semiclassical methods have been a perenniel source of insight into a diverse range of phenomena. In spite of this history, however, there remain interesting and insightful applications of semiclassical theory to physics. This thesis advances this programme in several directions. First, we consider the statistical mechanics of multivalent 1D Coulomb gases and demonstrate how the semiclassical WKB method may be used to expose its thermodynamic properties. In doing so, we develop ideas from algebraic topology and complex Riemann surfaces. Moving to quantum theory proper, these tools are applied fruitfully to the phenomenon of spin tunneling oscillations in magnetic molecules with large intrinsic spin. Moving away from the WKB approximation, these ideas from complex analysis also proved crucial in exposing universal finite-size scaling effects in 1D lattice systems such as the Su-Schrieffer-Heeger model of polyacetylene and the Kitaev chain. Finally, we end by considering the the weak noise theory of the KPZ equation and thereby discover a novel phase transition in its large deviation statistics.

Contents

Acknowledgements	i
Dedication	ii
Abstract	iii
List of Figures	vi
1 Introduction	1
2 Multivalent Coulomb gases	3
2.1 Introduction	3
2.2 Mapping of Coulomb gases onto quantum mechanics	6
2.2.1 \mathcal{PT} Symmetry	8
2.2.2 Isospectrality	9
2.3 Numerical Analysis	10
2.4 Monovalent (1,1) gas	13
2.4.1 Integration and topology on torus	15
2.4.2 Picard-Fuchs equation	17
2.4.3 Structure of $S_j(u)$ near $u = -1$	20
2.4.4 Semiclassical results	22
2.4.5 Neighborhood of $u = \infty$	23
2.5 Divalent (2,1) gas	25
2.6 Trivalent (3,1) gas	31
2.7 Higher valence gases	38

3 Spin tunneling oscillations of single molecule magnets	41
3.1 Introduction	41
3.2 Single molecule magnets and spin-coherent states	42
3.3 Riemann surface calculations	44
3.3.1 Analysis of the Riemann surface	45
3.3.2 Evaluating action integrals	47
4 Universal finite-size scaling in 1D lattice models	56
4.1 Introduction	56
4.2 Universality of the scaling function	58
4.3 Different symmetry classes	60
4.4 Analytic properties of the scaling function	62
5 Large deviation statistics of the KPZ equation with weak noise	67
5.1 Introduction	67
5.2 Weak noise theory	69
5.3 Derivation of the minimization problem	71
5.4 Small- H expansion	73
5.5 Phase transition at $H < 0$: numerical evidence	75
5.6 Negative- H tail	77
6 Conclusion and Discussion	80
References	84
Appendix A. Cole-Hopf transformation, kinks, solitons and ramps	93

List of Figures

2.1	Complex plane of normalized energy $u = 2\epsilon_m(q)/3\alpha$ for $(2, 1)$ gas. The color corresponds to different values of quasimomentum q ; blue stands for $q = 0$ and red for $q = \pm 1/2$. The dotted circle is $ u = 1$, the dashed lines connect between $u = 1$ and $u = e^{\pm i\pi/3}$, indicating positions of the narrow complex bands in the limit of large α .	11
2.2	Band structure for $(2, 1)$ gas with $\alpha = 1$, cf. Fig. 2.1b, vs. boundary charge (quasi-momentum) q . For the complex bands the real part of $\epsilon_m(q)$ is shown in dashed blue.	12
2.3	Complex plane of normalized energy u , Eq. (2.11), for $\alpha = 200$ and various valences (n_1, n_2) . The dotted circle is $ u = 1$, the dashed lines connect spectrum termination points $u = -(1)^{1/(n_1+n_2)}$ and $u = 1$, indicating positions of narrow complex bands.	13
2.4	(a) Complex z -plane with two cuts. (b) It compactifies to Riemann sphere with two cuts.	14
2.5	Construction of Riemann surface of genus 1. Two Riemann spheres with two cuts each are deformed into tubes to make the gluing in the final step more clear.	15
2.6	Riemann surface of genus-1 with two basic cycles δ_0 and δ_1 on it. In the limit $u \rightarrow \mp 1$ the torus degenerates into a singular surface. This coincides with the loop δ_0 (but not δ_1) becoming contractible to a point.	16
2.7	The classically allowed (forbidden) region at energy $2u$ are shown by the solid (dashed) gray line. A classical (instanton) periodic orbit, in the complex θ -plane, leads to $\gamma_0(\gamma_1)$ cycles.	17

2.8	Cycles γ_0 and γ_1 on the complex z -plane for $u = -0.9$. Notice that cycle γ_1 crosses twice the two cuts from first branch (solid blue line) to second branch (dashed red line) and back.	18
2.9	The two cycles $\gamma_{0,1}$ for $u = 0$. Here γ_1 may be mapped to γ_0 by rotating 180°	20
2.10	Monodromy transformation $(u + 1) \rightarrow (u + 1)e^{2\pi i}$ rotates the branch cut between $[z_-, z_+]$ by 180° counter-clockwise. This changes the cycle $\delta_1 \rightarrow \delta'_1 = \delta_1 - \delta_0$ along with it.	21
2.11	(Color online) Complex z -plane with two branch cuts, shown in gray. (a) Three integration cycles $\gamma_0, \gamma_1, \gamma_2$ are displayed for $u = 0$. (b) The instanton cycle $\Gamma = -\gamma_1 + \gamma_2$. The solid blue (dashed red) lines denote parts of the cycles going over the first (second) branch.	26
2.12	(Color online) Narrow energy bands (red dots) in the upper half-plane of complex energy u for $\alpha = 200$, cf. Fig. 2.3a. $Im S_0(u) = 0$ along the real axis, where the small lines mark $Re S_0(u) = 2\pi\alpha^{-1/2}(m + 1/2)$. The line $Im S_1(u) = 0$ emerges from $u = e^{i\pi/3}$ and intersects the real axis at $u \approx 0.96$. To the right of this point we observe bands with narrow gaps and use the same coloring convention as in FIGs. 2.1, 2.3. The small perpendicular lines mark $Re S_1(u) = 2\pi\alpha^{-1/2}(m + 1/2)$	29
2.13	(Color online) Analytic (numerical) results for the logarithm of the bandwidth of the lowest band, $\ln(\Delta\epsilon)_0$, versus square-root of the charge concentration, $\sqrt{\alpha}$, with (1, 1) as dotted (circles), (2, 1) dashed (diamonds) and (3, 1) as solid line (stars).	30
2.14	(Color online) (a) Double torus curve \mathcal{E}_u for $u^4 \neq 1$, having four basic cycles. (b) When $u^4 = 1$ the $g = 2$ torus degenerates into a singular $g = 1$ surface. This makes one of the basic cycles to pass through the singularity, and renders another cycle contractible to a point.	32
2.15	(Color online) The Riemann surface is doubly branched with a total of three cuts, shown in gray. The four cycles γ_j with $j = 0, 1, 2, 3$, along with the instanton cycle Γ (defined for later reference) are displayed for $u = 0$. The solid blue (dashed red) lines denote parts of the cycles going over the first (second) branch.	33

3.16 (Color online) Narrow energy bands in the upper half-plane of complex energy u for $\alpha = 200$, cf. Fig. 2.3b. $\text{Im } S_0(u) = 0$ along the real axis, where the small lines mark $\text{Re } S_0(u) = 2\pi\alpha^{-1/2}(m + 1/2)$. The line $\text{Im } S_1(u) = 0$ emerges from $u = i$ and intersects the real axis at $u \approx 1.09$. To the right of this point we observe bands with narrow gaps and use the same coloring convention as in FIGs. 2.1, 2.3. The small perpendicular lines mark $\text{Re } S_1(u) = 2\pi\alpha^{-1/2}(m+1/2)$; red dots, numerically computed narrow bands.

3.1 Energy levels for $\lambda = 0.728$ and $J = 10$ versus applied magnetic field. The red-dashed line marks the critical value for the field, underneath it pairs of levels are nearly degenerate. The splitting is caused by instantons and oscillates with applied field, the inset shows the example for the sixth pair of levels.

3.2 (Color online) Left: Plane of complex q for $\lambda = 0.5$, $h = 0.4$ and $\epsilon = 0.1$. The black points are the singularities $\pm i$ and q_{\pm} , where a full (open) point means the non-zero residue is only on the first (second) sheet. The blue lines are the branch cuts, the outer branch cut, along the imaginary axis, is continued to $\pm i\infty$. The instanton trajectories γ_1 ($\bar{\gamma}_1$) in light (dark) red connect two classical turning points (endpoints of inner branch cut) on opposite sheets, where a solid (dashed) line is on the first (second) sheet. Right: The Riemann surface of genus 1 can be seen as a torus. The green trajectory is the classical cycle around the inner branch cut. Combining $\gamma_1 + \bar{\gamma}_1 = \Gamma$ gives a closed instanton trajectory.

3.3 Schematics of a monodromy transformation where two branch points (blue) are exchanged. Left: original cycle (red), where the solid (dashed) part is on the first (second) sheet. Middle: The two branch points to the right exchanged counter-clockwise. Right: Constructing the original cycle from the transformed cycle introduces an additional cycle around the branch cut (claret-red).

3.4	Schematics of a monodromy transformation where the branch cut (blue) entangles singularities (black). Left: original branch cut structure, where full (empty) circle is a singularity on first (second) sheet. Middle: The branch cut moved around the singularities counter-clockwise. Right: The branch cut is brought to its original position. During this process both singularities cross the branch cut to the respective other sheet. To restore the initial singularities the notion of first and second sheet is inverted.	51
3.5	Analytic results (dashed, different colors) for the logarithm of the level splitting, compared to numeric calculations (solid-black). Here $\lambda = 0.728$ for the Fe_8 molecule [56].	53
4.1	(Color online) Numerical results for $f(w)$, where $w = Nm$ and $N = 100$ for 5 topologically non-trivial symmetry classes in one spatial dimension. (a) The case for open boundary conditions which is sensitive to topology, the solid line is the scaling function given by Eq. (4.15). (b) In periodic boundary conditions the results are independent of the topological index and the scaling function Eq. (4.16) is symmetric. There is a difference between even ($f(w)$ negative) and odd ($f(w)$ positive) number of sites $N = 100, 101$	57
4.2	(Color online) SSH model (AIII symmetry class): (a) Visualization of the phase shift across the transition. For a fixed $w = Nm$, a state exists with energy $\epsilon^\pm(k)$ if $w = kN \cot(kN)$, Eq. (4.11). In both limits $w \rightarrow \pm\infty$ there are states at $kN = n\pi$, however one pair of states collides at $w = 1$ (blue) and obtains imaginary k , shown as dashed line. (b) Energy spectrum near the gap for a $N = 50$ SSH Hamiltonian (black), with a pair of evolving edge states (blue). The edge state crosses the bulk Dirac cone (thin red) at $w = 1$, where the momentum becomes imaginary. (c) Comparison of numerical results for SSH Hamiltonians with the scaling function (4.15) for system sizes $N = 50, 100, 200$ and three transitions in a 2-chain SSH model with topological indexes $Z = 0 \rightarrow 1, 1 \rightarrow 2, 0 \rightarrow 2$	59

4.3	Integration contour in the complex k plane for $N = 10$ and $w = 1.1$. The contour (red) encloses all zeroes of the argument of the logarithm (blue) and is to be taken counter-clockwise. After a change of variable $z = Nk$ and taking the scaling limit $N \rightarrow \infty$ the contour runs along the entire real line, above and below. These two parts of the contour are now deformed (purple) to run along the branch cuts of $\sqrt{m^2 + k^2}$ (green).	63
5.1	The optimal path in the linear approximation, as described by Eqs. (5.25) and (5.26) for $H < 0$, at $t = 0, 0.25, 0.5, 0.75$ and 1 (top panel, from top to bottom) and $t = 0, 0.5$ and 0.95 (bottom panel).	74
5.2	The optimal path for $\Lambda = -6.3$ computed numerically. Shown are h (top) and ρ (bottom) vs. x at $t = 0$ (solid line), 0.5 (short dash) and 1 (long dash).	76
5.3	Same as in Fig. 5.2 but for $\Lambda = -10$	76
5.4	Top: Δ vs. $ H $ at $H < 0$. Symbols: numerical results, solid line: Eq. (5.28), dashed line: the $ H \gg 1$ asymptotic $ \Delta = H $. Bottom: s vs. $ H $ at $H < 0$: The asymmetric and symmetric branches are shown by the solid and empty symbols, respectively. Also shown are the small- and large- $ H $ asymptotics of s	77
5.5	The optimal path, $h(x, t)$ and $\rho(x, t)$, for $H < 0$ and $ H \gg 1$, see Eqs. (5.29)-(5.31), for $t = 0, 1/2$ and 1	78
A.1	Example of exact two-ramp/two-soliton solutions (A.7) and (A.7) for $h(x, t)$ and $\rho(x, t)$, respectively. Shown (for $c = 8$) are h and ρ versus x for $N = 3, c_1 = X_1 = 0, c_3 = -c_2 = c$ and $X_3 = -X_2 = -(3/8)c$. Top panel: $t = 0$ (solid), $1/4$ (dashed), $3/4$ (dash-dotted) and 1 (solid). Bottom panel: $t = 0$ (solid), $1/4$ (dashed) and 1 (dash-dotted). Inset: ρ versus x at $t = 1/2, 4/5$ and 1 . At $c \gg 1$ and $t > \tau$, ρ approaches the exact stationary one-soliton solution [112, 115, 118].	95
A.2	Same as in Fig. A.1 but for $X_3 = -X_2 = -c$ (that is, $\tau = 1$) and $t = 0$ (solid), $1/2$ (dashed) and 1 (dash-dotted). The inset shows a blowup of the collision and merger of the two solitons at $t = 0.95, 0.965$ and 1	96

Chapter 1

Introduction

To motivate the analyses that will be presented in this thesis, it is worth discussing why semiclassical theory has been and remains a source of interesting physics. Modern quantum and statistical physics are formulated within the language of functional integrals i.e. integrals of an appropriate space of paths. But while such spaces include an infinity of such paths, they are not all treated equal.

In particular, we expect those paths which pass through saddle points of the classical action to dominate. Within the Feynman path integral formulation of quantum mechanics in particular, we obtain in this manner formula such as the Bohr-Sommerfeld quantization condition for bound states and the Gamow formula for the tunneling amplitude between regions which would otherwise be classically forbidden. This can be extended further in many different directions: For instance, we can consider systems whose paths display interesting interference effects (e.g. multivalent Coulomb gas, large magnetic molecules), or systems where the weighting over paths is stochastic in origin rather than quantum-mechanical (e.g. the weak-noise theory of the Kardar-Parisi-Zhang equation). In this way we begin to see both the complexity and depth that the semiclassical method has to offer in modern physics.

As a secondary theme, the classical and instanton actions in these systems can be naturally obtained in terms of contour integrals in an appropriate complex phase space. This has the virtue that the values of these integrals only depend on the topology of such contours rather than their particular details; in this manner we may avoid worrying about detailed trajectories and instead make use of tools from complex algebraic

geometry such as the Picard-Fuchs equation and monodromy.

With these goals in mind, we briefly elaborate the structure of this thesis. Each chapter is adapted from a publication of the author over the course of his graduate school career.

In chapter 2, we consider 1D multivalent Coulomb gas as a non-Hermitian spectral problem. We will find that thermodynamic and transport properties of the system can be computed by means of the WKB approximation, in particular Bohr-Sommerfeld quantization and the Gamow tunneling formula. Furthermore, we show the applicability of Riemann surface and algebraic topology in order to make these calculations tractable. The chapter is adapted from the 2013 paper of Gulden, Kamenev, Koroteev, and the author [1].

In chapter 3, we move to the purely quantum-mechanical problem of the energy spectrum of single-molecule magnets. These are known to exhibit interesting features of oscillatory level splitting as a function of applied magnetic field, and the semiclassical analysis of such is facilitated by the same analytic techniques as developed in chapter 1. In particular, we focus on the application of the monodromy concept in this setting. The chapter is adapted from the 2015 paper of Gulden, Kamenev, and the author [3].

In chapter 4, we depart from the WKB method used of the preceeding chapters and instead consider the large-size asymptotics of certain 1D lattice models such as polyacetylene and the Kitaev chain. We find that, in the vicinity of a topological phase transition, the finite-size corrections to free energy are universal and are uniquely described by the central charge of the corresponding conformal field theory of the critical system. The chapter is adapted from the 2016 paper of Gulden, Wang, Kamenev and the author [4].

In chapter 5, we consider a purely stochastic system in the form of the large deviation statistics of the Karder-Parisi-Zhang equation in 1+1 dimensions at short times; the weak noise theory of this equation is the analogue of the semiclassical method in this setting. By applying this analysis to a certain two-sided Brownian motion we discover a novel dynamical phase transition whereby the reflection symmetry of optimal paths is spontaneously broken. The chapter is adapted from the 2016 paper of Kamenev, Meerson, and the author [5].

In chapter 6 we close by surveying the results and methods of this thesis.

Chapter 2

Multivalent Coulomb gases

2.1 Introduction

One of the very last works of Anatoliy Larkin[6] was devoted to transport through ion channels of biological membranes. An ion channel may be roughly viewed as a cylindrical water-filled tube surrounded by a lipid membrane. Its typical radius $a \approx 6\text{\AA}$ is much smaller than its length $L \approx 120\text{\AA}$. The important observation with far reaching consequences, made in Ref. [6], is that the dielectric constant of water $\epsilon_{\text{water}} \approx 80$ is significantly larger than that of the surrounding lipid membrane $\epsilon_{\text{lipid}} \approx 2$. This defines a new length scale $\xi \approx a\sqrt{\epsilon_{\text{water}}/\epsilon_{\text{lipid}}}\ln(\epsilon_{\text{water}}/\epsilon_{\text{lipid}}) \approx 140\text{\AA}$ over which the electric field stays inside the channel and does not escape into the surrounding media. Since $\xi \gtrsim L$, the ions inside the channel interact essentially through the 1D Coulomb potential $U(x_1 - x_2) \approx eE_0|x_1 - x_2|$, where $E_0 = 2e/a^2\epsilon_{\text{water}}$ is a discontinuity of the electric field created by a unit charge. This fact dictates a significant energy barrier $U(L/4) \approx 4k_B T_{\text{room}}$ for moving a single ion through the channel. If indeed present, such a barrier would essentially impede ion transport, preventing the channel from performing its biological functions.

Nature removes such Coulomb blocking by screening. A moving ion is screened either by mobile ions of dissociated salt[6], or by immobilized charged radicals attached to the walls of the channel [7, 8, 9, 10, 11, 12, 13, 14]. Nevertheless, due to the peculiar nature of the long-range 1D Coulomb potential, the transport barrier proportional to the channel length L is always present. Its magnitude, though, is typically suppressed[6]

down to about $k_B T_{\text{room}}$, allowing for a relatively unimpeded transport of ions. These considerations call for development of a transport theory of 1D Coulomb gases. Following the celebrated mapping of 1D statistical mechanics onto an effective quantum mechanics, pioneered by Edwards and Lenard [15] and Vaks, Larkin and Pikin[16], reference [[6]] mapped the problem onto quantum mechanics of a cosine potential (we briefly review this mapping in Sec. 2.2). The ground state energy of such quantum mechanics is exactly the equilibrium pressure in the Coulomb plasma. Moreover the width of the lowest Bloch band is a specific energy barrier for ion transport through the channel.

It is instructive to notice that $2\alpha \cos \theta = \alpha(e^{i\theta} + e^{-i\theta})$ potential describes a mixture of positive, $e^{i\theta}$, and negative, $e^{-i\theta}$, *monovalent* ions with concentration α . One may also consider a situation when the channel is filled with a solution of dissociated *multivalent* salt, such as e.g. divalent CaCl_2 or trivalent AlCl_3 . In these cases the corresponding 1D statistical mechanics is mapped onto the quantum problem with a *non-Hermitian* potential such as $\alpha(\frac{1}{2}e^{2i\theta} + e^{-i\theta})$ or $\alpha(\frac{1}{3}e^{3i\theta} + e^{-i\theta})$ [15, 7].

Our particular focus here is on a *semiclassical* treatment, applicable in the regime of sufficiently large salt concentration α . In its framework the energy spectrum (thus the pressure) is determined by the Bohr-Sommerfeld quantization condition for the action of classical periodic orbits. On the other hand, the bandwidth (and thus the transport barrier) is given by the exponentiated action accumulated on the *instanton* trajectory, running through the classically forbidden part of the phase space. The traditional techniques of Hermitian quantum mechanics call for finding classical and instanton trajectories by solving equations of motion in real and imaginary time and evaluating corresponding actions. This route can't be straightforwardly applied to non-Hermitian quantum problems arising in the context of multi-valent Coulomb gases. Even leaving aside the technical difficulties of solving complex equations of motion, there are conceptual difficulties with identifying periodic orbits as well as the meaning of classically allowed vs. forbidden regions and with the imaginary time procedure.

In this chapter we borrow from the algebraic topology methods developed in the past decades in the context of the Seiberg-Witten solution [17, 18] and its applications to integrable systems[19, 20, 21] (and many follow-up contributions). The central idea is to consider both coordinate θ and corresponding canonical momentum p as *complex* variables. This leads to *four*-dimensional (4D) phase space. Then (complex) energy

conservation restricts the trajectories to live on 2D Riemann surfaces embedded into 4D phase space. The dynamics of the system are essentially determined by the topology, i.e. genus g , of such Riemann surfaces. We show that e.g. mono- and divalent gases are described by tori, while trivalent and 4-valent lead to genus-2 surfaces, etc. The Cauchy theorem and the resulting freedom to deform the integration contour in the complex space allows to avoid finding specific solutions of the equations of motion. Instead one identifies the homology cycles on the Riemann surface and finds the corresponding action integrals, which depend only on the topology of the cycles and not on their specific shape. For example, the cosine potential of monovalent gas leads to a torus, which obviously has two topologically distinct cycles, Fig. 2.6. The two turn out to be related to classical and instanton actions correspondingly. The genus $g \geq 1$ Riemann surfaces admit $2g$ topologically distinct cycles. Below we identify and explain the meaning of the corresponding action integrals.

The shape of the specific Riemann surface depends on the parameters of the problem, e.g. salt concentration α in our case. Such parameters are called moduli of the Riemann surface. It turns out that the action integrals, being functions of the moduli, satisfy closed ordinary differential equation (ODE) of the order $2g$, known as the Picard-Fuchs equation. The actions may be found as solutions of this ODE in the moduli space, rather than performing integrations over cycles on the surface. Below we derive and solve Picard-Fuchs equations for several (positive, negative) ionic charge combinations, such as genus $g = 1$ cases $(1, 1), (2, 1)$ and genus $g = 2$ cases $(3, 1), (3, 2), (4, 1)$. We then discuss how to connect the principal classical actions with the spectra of the corresponding quantum problem. The key observation is that in the moduli space the actions exhibit a few isolated branching points. Going around such a branching point transforms the actions into their linear combinations – the $Sp(2g, \mathbb{Z})$ monodromy transformation. The invariance of quantum observables under monodromy transformations dictates Bohr-Sommerfeld quantization for one of the principal classical actions. The remaining actions may be identified with the instanton processes, related to e.g. Bloch bandwidth.

Statistical mechanics of 1D Coulomb gases may seem to be an isolated problem, not worthy of developing an extensive mathematical apparatus. Our goal here is to use it as a test-drive example, grounded into a well-posed physics problem, to develop

a machinery applicable in other setups. Recently the so-called \mathcal{PT} symmetric non-Hermitian quantum mechanics attracted a lot of attention for its application in active optics[22] and open quantum systems[23], as well as in the description of antiferromagnetic lattices[24] and calculating energy states in larger molecules[25]. Our examples also belong to the class of \mathcal{PT} symmetric problems. It seems likely that the methods developed here may be applied to advance analytical understanding of a broader class of \mathcal{PT} symmetric quantum mechanics. Another context, where complexified quantum mechanics was proven to be extremely useful, is dynamics of large molecular spins[26, 27]. Indeed functional integral representation of the spin dynamics leads naturally to the Hamiltonian formulation, where the projective coordinates (z, \bar{z}) on the sphere play the role of the canonical pair[28]. It was realized[26, 27] that to find instanton trajectories one has to consider z and \bar{z} as independent complex variables, thus expanding the dynamics into 4D phase space. The Riemann geometry methods seem to be well-suited to advance this subject as well.

This chapter is organized as follows: in section 2.2 we outline the relation between 1D multivalent Coulomb gases and non-Hermitian quantum mechanics and discuss general symmetries of the latter. In section 2.3 we summarize major numerical observations regarding complex spectra and band-structure for the family of Hamiltonians considered here. In section 2.4 we illustrate the machinery of algebraic geometry on Riemann surfaces for the familiar Hermitian cosine potential quantum mechanics, which corresponds to the monovalent $(1, 1)$ gas. Here we introduce complexified phase space and Riemann torii of constant energy; we then derive, solve and analyze solutions of the Picard-Fuchs equations. In section 2.5 we apply the developed methods for the divalent $(2, 1)$ Coulomb gas, which is also described by a genus-1 torus. In section 2.6 we extend the method for genus-2 example of trivalent $(3, 1)$ gas, which exhibits some qualitatively new features. The $(3, 2)$ and $(4, 1)$ gases are briefly tackled in section 2.7.

2.2 Mapping of Coulomb gases onto quantum mechanics

Consider a 1D gas of cations with charge $n_1 e$ and anions with charge $-n_2 e$, where (n_1, n_2) are positive integers. By Gauss's theorem, the electric field at a distance x larger than the radius of the channel a from a unit charge is $E_0 = 2e/a^2\epsilon_{\text{water}}$. At the

location of a charge $n_{1,2}$ the electric field exhibits a discontinuity $\pm 2E_0 n_{1,2}$. Since all charges are integers the field is conserved modulo $2E_0$ along the channel. This allows us to define the order parameter[6, 8] $q = E(x) \pmod{2E_0}$, which acts like an effective boundary charge $\pm q$ at the two ends of the channel. The Poisson equation in 1D reads $\nabla^2\phi = -2E_0\delta(x)$, leading to 1D Coulomb potential $\phi(x) = -E_0|x|$. The potential energy of the gas is thus

$$U = -\frac{eE_0}{2} \sum_{i,j} \sigma_i \sigma_j |x_i - x_j|, \quad (2.1)$$

where σ_j is the charge n_1 or $-n_2$ of an ion at the position x_j and we omit the $\pm q$ boundary charges for brevity. Our goal is to evaluate the grand canonical partition function of the gas in the channel of length L

$$\mathcal{Z}_L = \sum_{N_1, N_2=0}^{\infty} \frac{f_1^{N_1} f_2^{N_2}}{N_1! N_2!} \prod_{i=1}^{N_1} \int_0^L dx_i \prod_{j=1}^{N_2} \int_0^L dx_j e^{-U/k_B T}, \quad (2.2)$$

where $f_{1,2}$ are fugacities of the two charge species. One can now introduce the charge density employing a delta-function $\delta[\rho(x) - \sum_j \sigma_j \delta(x - x_j)]$. The delta-function is elevated in the exponent with the help of the auxiliary field $\theta(x)$. This procedure decouples all x_j integrals[6], bringing them to the form $\sum_N [f \int dx e^{i\sigma\theta(x)}]^N / N! = \exp\{f \int dx e^{i\sigma\theta(x)}\}$. The interaction potential (2.1), being inverse of the 1D Laplace operator, leads to $\exp\{(T/eE_0) \int dx \theta \partial_x^2 \theta\}$. As a result the partition function (2.2) is identically written as the Feynman path integral, in an “imaginary time” x , for the quantum mechanics with the Hamiltonian

$$\hat{H} = (i\partial_\theta - q)^2 - (\alpha_1 e^{in_1 \theta} + \alpha_2 e^{-in_2 \theta}), \quad (2.3)$$

where $\alpha_{1,2} = f_{1,2} k_B T / eE_0$ are dimensionless ion concentrations. Such Feynman integral is the expectation value of the evolution operator during “time” L , leading to

$$\mathcal{Z}_L = \left\langle q \left| \mathcal{X} e^{-\frac{eE_0}{k_B T} \int_0^L dx \hat{H}} \right| q \right\rangle = \sum_m |\langle q | m \rangle|^2 e^{-\frac{eE_0 L}{k_B T} \epsilon_m(q)}, \quad (2.4)$$

where \mathcal{X} stands for x -ordered exponent. Here $\epsilon_m(q)$ are eigenvalues of the effective Hamiltonian \hat{H} and $|m\rangle = \psi_m(\theta)$ are its eigenvectors in the Hilbert space of periodic functions $\psi_m(\theta) = \psi_m(\theta + 2\pi)$, and finally the matrix elements are $\langle q|m\rangle = \int_0^{2\pi} d\theta e^{-iq\theta} \psi_m(\theta)$. The boundary charge q plays the role of the Bloch quasi-momentum and the spectrum is obviously periodic in q with the unit period (reflecting the fact that the integer part of the boundary charge may be screened by mobile ions and thus inconsequential).

The pressure of the Coulomb gas is its free energy per unit length

$$P = k_B T \frac{\partial \ln \mathcal{Z}_L}{\partial L} \xrightarrow{L \rightarrow \infty} -eE_0 \epsilon_0(q), \quad (2.5)$$

where $\epsilon_0(q)$ is the eigenvalue with the smallest real part. In equilibrium the system minimizes its free energy by choosing an appropriate boundary charge q . In all cases considered below the minimum appears to be a non-polarized state of the channel, i.e. $q = 0$ (see however Refs. [[7]] for exceptions to this rule). Adiabatic charge transfer through the channel is associated with the boundary charge q sweeping through its full period. As a result, the (free) energy barrier for ion transport is

$$U_0 = eE_0 L \Delta_0, \quad (2.6)$$

where Δ_0 is the width of the lowest Bloch band. Therefore the ground state energy and the width of the lowest Bloch band of the Hamiltonian (2.3) determine thermodynamic and transport properties of the (n_1, n_2) Coulomb gas. The rest of this chapter is devoted to a semiclassical theory of the spectral properties of such Hamiltonians. We start by discussing some general symmetries of the non-Hermitian Hamiltonian (2.3).

2.2.1 \mathcal{PT} Symmetry

Although the Hamiltonian (2.3) is non-Hermitian for $n_1 \neq n_2$, it obeys \mathcal{PT} -symmetry [29, 30]. Here the parity operator \mathcal{P} acts as $\theta \rightarrow -\theta$, while the time-reversal operator \mathcal{T} works as complex conjugation $i \rightarrow -i$. Clearly the two operations combined leave the Hamiltonian (2.3) unchanged. One may prove [30, 31] that all eigenvalues of \mathcal{PT} -symmetric Hamiltonians are either real, or appear in complex conjugated pairs. As

shown below for positive values of concentrations $\alpha_{1,2} > 0$ the lowest energy band $\epsilon_0(q)$ is entirely real, ensuring the positivity of the partition function. The higher bands $\epsilon_m(q)$ are in general complex. It is interesting to note that, for unphysical negative concentrations $\alpha_{1,2} < 0$, already the lowest band $\epsilon_0(q)$ is complex, making the free energy ill-defined.

2.2.2 Isospectrality

The spectrum of the Hamiltonian (2.3) is invariant under shift of the coordinate $\theta \rightarrow \theta + \theta_0$, where θ_0 is an arbitrary complex number. Upon such transformation (preserving the periodic boundary conditions) the dimensionless concentrations $\alpha_{1,2}$ renormalize as $\alpha_1 \rightarrow \alpha_1 e^{in_1 \theta_0}$ and $\alpha_2 \rightarrow \alpha_2 e^{-in_2 \theta_0}$. Notice that the combination $\alpha_1^{n_2} \alpha_2^{n_1}$ remains invariant. From here one concludes that the family of Hamiltonians (2.3) with

$$\alpha_1^{n_2} \alpha_2^{n_1} = \text{const} \quad (2.7)$$

are *isospectral*[15]. Thus without loss of generality, one may pick one representative from each isospectral family. It is convenient to choose such a representative to manifestly enforce charge neutrality in the bulk reservoirs. To this end one takes $\alpha_1 n_1 = \alpha_2 n_2 = \alpha$, which brings the Hamiltonian (2.3) to the form

$$\hat{H} = \alpha \left[\hat{p}^2 - \left(\frac{1}{n_1} e^{in_1 \theta} + \frac{1}{n_2} e^{-in_2 \theta} \right) \right], \quad (2.8)$$

where we have defined the momentum operator as

$$\hat{p} = \alpha^{-1/2} (-i\partial_\theta + q); \quad [\theta, \hat{p}] = i\alpha^{-1/2}. \quad (2.9)$$

The commutation relation shows that $\alpha^{-1/2}$ plays the role of the effective Planck constant. With the help of the isospectrality condition (2.7), one may always choose a proper α such that the spectrum of Hamiltonian (2.8) is identical with that of a Hamiltonian with arbitrary $\alpha_{1,2}$. The physical reason for this symmetry is that the interior region of the long channel always preserves charge neutrality, allowing the edge regions to screen charge imbalance of the reservoirs. Therefore, irrespective of the relative fugacities of cations and anions in the reservoirs, the thermodynamics of the long channel

are equivalent to the one in contact with neutral reservoirs with an appropriate salt concentration α . Hereafter we restrict ourselves to the neutral Hamiltonian (2.8) with the single parameter α .

2.3 Numerical Analysis

In this section we discuss numerical simulation of the spectrum of the Hamiltonian (2.8). We focus on unequal charges $n_1 \neq n_2$, since the case of $n_1 = n_2$ reduces to the well-known Hermitian cosine potential[32, 33]. For unequal charges the Hamiltonian is non-Hermitian but \mathcal{PT} -symmetric, allowing for complex eigenvalues which appear in conjugated pairs[30, 31].

Since the Hamiltonian \hat{H} acts in the Hilbert space of periodic functions, one may choose the complete basis in the form $\{e^{im\theta}\}_{m \in \mathbb{Z}}$. In this basis the Hamiltonian is represented by an infinite size *real* matrix[7]

$$\hat{H}_{m,m'} = (m - q)^2 \delta_{m,m'} - \alpha \left(\frac{1}{n_1} \delta_{m+n_1, m'} + \frac{1}{n_2} \delta_{m-n_2, m'} \right). \quad (2.10)$$

The boundary charge q plays the role of quasi-momentum residing in the Brillouin zone $q \in [-\frac{1}{2}, \frac{1}{2}]$. To numerically calculate the energy spectrum $\epsilon_m(q)$ we truncate the matrix at a large cutoff, after checking that a further increase in the matrix size does not change the low-energy spectrum. We left the boundary conditions “open”, i.e. did not change the matrix elements near the cutoff, after verifying that different boundary conditions don’t affect the result. It is easy to see that the matrix size should be $\gg \sqrt{\alpha}$ to accurately represent the low-energy spectrum. As an illustration we show the Hamiltonian cut to a 5×5 matrix for divalent (2, 1) gas:

$$\begin{pmatrix} (-2 - q)^2 & 0 & -\frac{\alpha}{2} & 0 & 0 \\ -\alpha & (-1 - q)^2 & 0 & -\frac{\alpha}{2} & 0 \\ 0 & -\alpha & (0 - q)^2 & 0 & -\frac{\alpha}{2} \\ 0 & 0 & -\alpha & (1 - q)^2 & 0 \\ 0 & 0 & 0 & -\alpha & (2 - q)^2 \end{pmatrix}$$

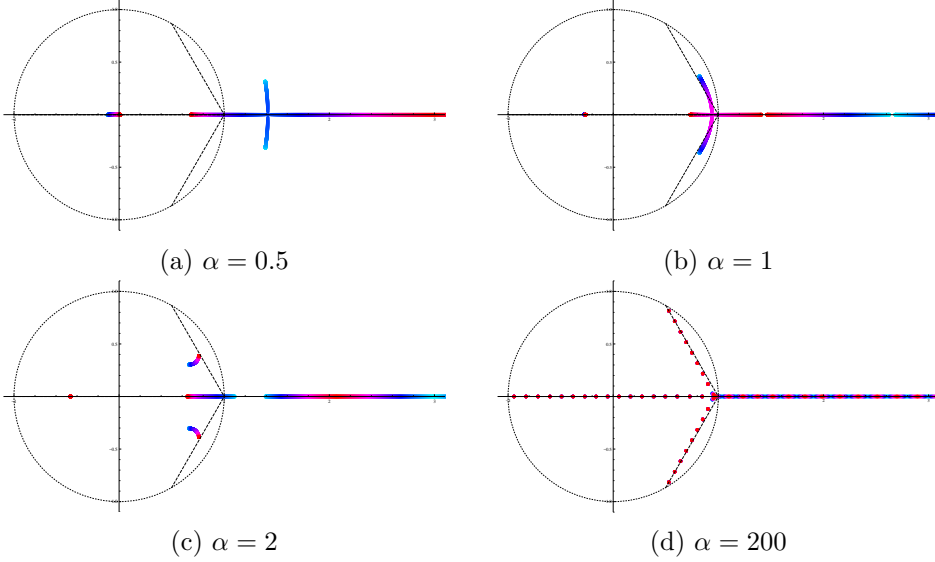


Figure 2.1: Complex plane of normalized energy $u = 2\epsilon_m(q)/3\alpha$ for $(2, 1)$ gas. The color corresponds to different values of quasimomentum q ; blue stands for $q = 0$ and red for $q = \pm 1/2$. The dotted circle is $|u| = 1$, the dashed lines connect between $u = 1$ and $u = e^{\pm i\pi/3}$, indicating positions of the narrow complex bands in the limit of large α .

For reasons which will become apparent below, it is convenient to present the spectrum ϵ on the complex plane of the normalized energy u defined as

$$u = \frac{n_1 n_2}{n_1 + n_2} \frac{\epsilon}{\alpha}. \quad (2.11)$$

For the divalent $(2, 1)$ gas $u = 2\epsilon/3\alpha$ and the corresponding spectra are shown in Fig. 2.1. The spectrum consists of a sequence of complex Bloch bands. The number of narrow bands within the unit circle $|u| = 1$ scales as $\sqrt{\alpha}$. They form three branches which terminate at $u = -1$ and $u = e^{\pm i\pi/3}$ and approximately line up along the lines connecting the termination points with the point $u = 1$. We shall discuss the corresponding bandwidths below. Outside the unit circle the bands are wide and centered near the positive real axis of energy.

Figure 2.2 shows the band structure in the first Brillouin zone $|q| < 1/2$ for $\alpha = 1$. Notice that the lowest Bloch band is purely real (this is always the case for $\alpha > 0$), ensuring positive partition function (2.4) and real pressure (2.5). The next two bands are complex. For $|q| < q_c \approx 0.36$ they exhibit opposite imaginary parts (not shown),

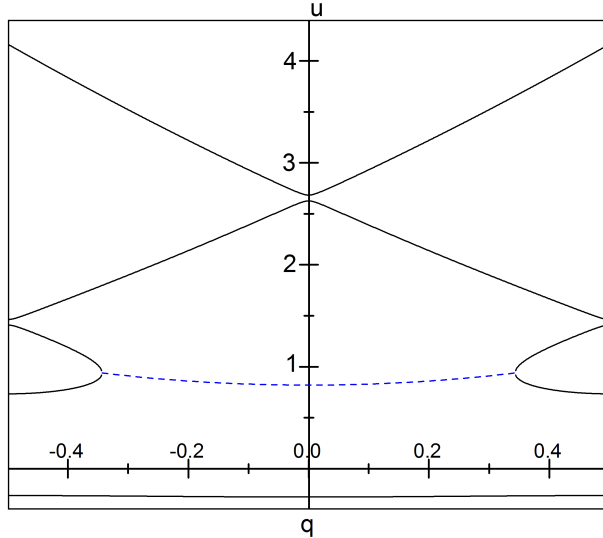


Figure 2.2: Band structure for $(2, 1)$ gas with $\alpha = 1$, cf. Fig. 2.1b, vs. boundary charge (quasi-momentum) q . For the complex bands the real part of $\epsilon_m(q)$ is shown in dashed blue.

but turn real at $|q| > q_c$. The next two bands are real, cf. Fig. 2.1b. The higher bands form an alternating sequence of two real and two complex bands. For larger values of α there is a sequence of entirely complex narrow bands, cf. Fig. 2.1d.

Figure 2.3 shows normalized spectra for several different combinations of charges on the complex energy plane of u , Eq. (2.11), at large concentration $\alpha = 200$. One may notice odd number $n_1 + n_2$ or $n_1 + n_2 - 1$ of spectral sequences, consisting of order $\sqrt{\alpha}$ exponentially narrow bands, seen as points. The central sequence goes along the real axis terminating at the bottom of the spectrum near $u = -1$. The other appear in conjugated pairs terminating near the roots of unity $u = -(1)^{1/(n_1+n_2)}$. Close to the termination points the band sequences align along the lines pointing towards $u = 1$. Further away from the termination points they deviate from these lines and may coalesce.

Although thermodynamics and transport properties of the Coulomb gases are merely determined by the lowest band $\epsilon_0(q)$, below we address the wider spectral properties of Hamiltonians (2.8), presented in Figs. 2.1 – 2.3. To this end we develop a semiclassical theory which is best suited for the description of exponentially narrow bands present at large concentration $\alpha \gtrsim 1$.

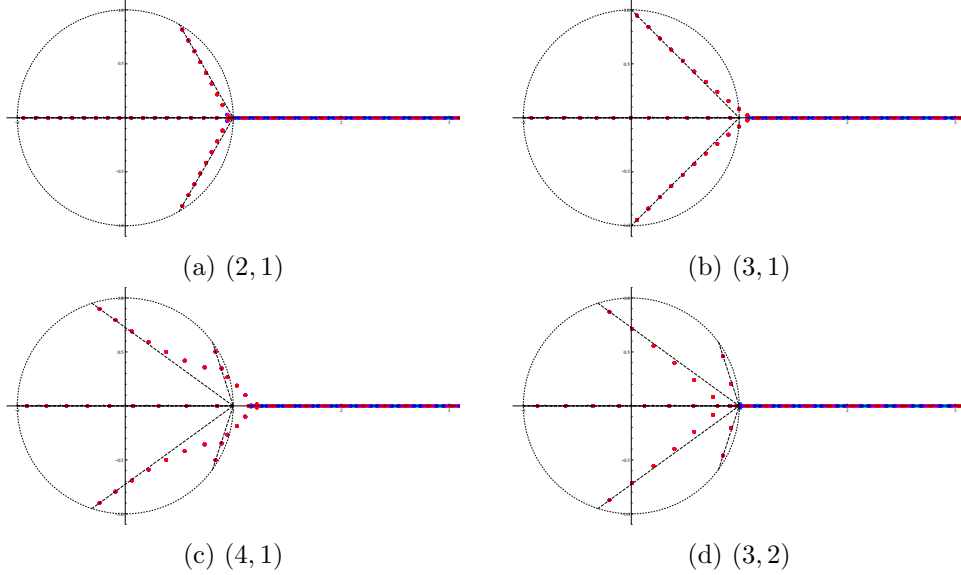


Figure 2.3: Complex plane of normalized energy u , Eq. (2.11), for $\alpha = 200$ and various valences (n_1, n_2) . The dotted circle is $|u| = 1$, the dashed lines connect spectrum termination points $u = -(1)^{1/(n_1+n_2)}$ and $u = 1$, indicating positions of narrow complex bands.

2.4 Monovalent (1,1) gas

To introduce the methods, we first develop a semiclassical spectral theory for the Hermitian Hamiltonian (2.8), (3.7) with $n_1 = n_2 = 1$. To this end we look for wavefunctions in the form $\psi = e^{i\alpha^{1/2}S}$, where S is an action for the classical problem with the normalized Hamiltonian

$$2u = p^2 - 2 \cos \theta, \quad (2.12)$$

where $u = \epsilon/(2\alpha)$, so $u = \mp 1$ correspond to the bottom (top) of the cosine potential. The semiclassical calculations require knowledge of the action integrals. Our approach to such integrals is based on complex algebraic geometry. First, let $z = e^{i\theta}$ and consider (z, p) as complex variables. Since $p(z)$ resides on the constant energy hypersurface

$$2u = p^2 - \left(z + \frac{1}{z} \right), \quad (2.13)$$

we have a family of complex algebraic curves

$$\mathcal{E}_u : \quad \mathcal{F}(p, z) = p^2 z - (z^2 + 2uz + 1) = 0 \quad (2.14)$$

parameterized by u . For $u \neq \mp 1$ it can be checked that $(\partial \mathcal{F}/\partial z, \partial \mathcal{F}/\partial p)$ does not vanish on \mathcal{E}_u , so each \mathcal{E}_u is nonsingular. Then $\mathcal{F}(p, z)$ implicitly defines a locally holomorphic map $p = p(z)$. The exceptions to this occur at $z = 0, \infty, z_{\pm}$, where

$$z_{\pm} = -u \pm i\sqrt{1-u^2} \quad (2.15)$$

are the roots of $p^2 = 0$ (i.e. classical turning points). In a vicinity of these *four* branching points $p(z)$ behaves as

$$p \sim z^{-1/2}, \quad (z \sim 0) \quad (2.16)$$

$$p \sim z^{1/2}, \quad (z \sim \infty) \quad (2.17)$$

$$p \sim (z - z_{\pm})^{1/2}, \quad (z \sim z_{\pm}) \quad (2.18)$$

respectively, i.e. $p(z)$ is locally double-valued. (Note that we have added a point at $z = \infty$ to the complex plane, thereby rendering it compact and topologically equivalent to a Riemann sphere, Fig. 2.4). To make sense of this double-valuedness, we first introduce *two* cuts between the four branching points. For convenience we have chosen to do so between $0, \infty$ and the turning points z_{\pm} . Upon this cut domain, $p(z)$ is locally holomorphic.

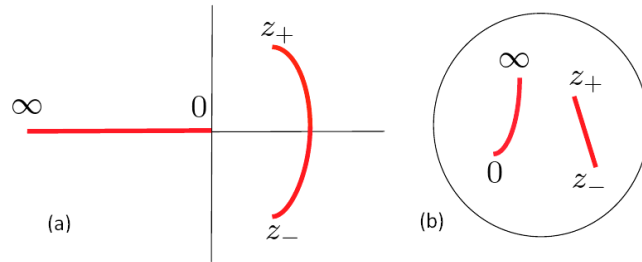


Figure 2.4: (a) Complex z -plane with two cuts. (b) It compactifies to Riemann sphere with two cuts.

We then introduce a second sheet of the z -plane and the corresponding Riemann sphere, cut in the same way as the first. We then analytically continue $p(z)$ on the first sheet across the cuts onto the second sheet. If $p(z)$ is analytically continued across the branch cut again, we arrive back on the first sphere where we started. In this way, we obtain $p(z)$ as a locally holomorphic function, whose domain is a doubly-branched cover of the Riemann sphere. Furthermore, suppose we open up the branch cuts, keeping track where on the other branch $p(z)$ will be, if we cross one side of a cut. Identifying these edges one obtains a torus as in Fig. 2.5 (where the arrows are used to signify the glued together edges). Thus the complex algebraic curve \mathcal{E}_u can be understood as a compact Riemann surface of genus $g = 1$ (generically, every compact Riemann surface is topologically a sphere with some number of handles g , called the genus of the surface).

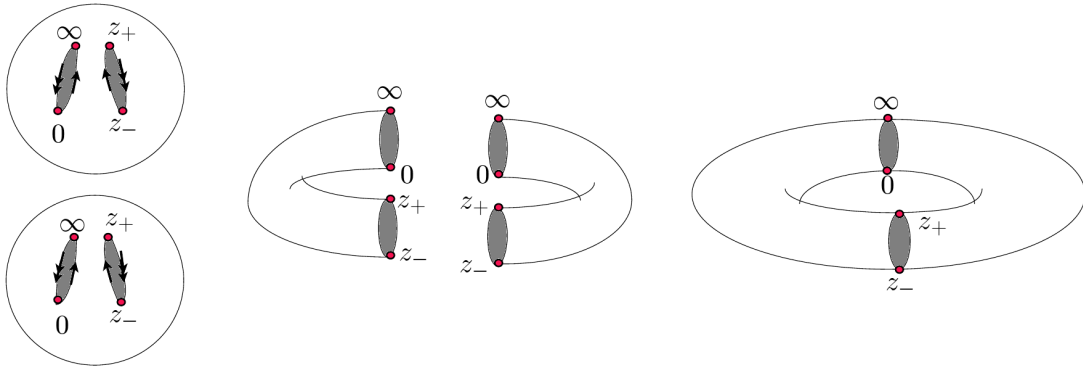


Figure 2.5: Construction of Riemann surface of genus 1. Two Riemann spheres with two cuts each are deformed into tubes to make the gluing in the final step more clear.

In the exceptional points $u = \mp 1$ the two turning points collide ($z_+ = z_- = \pm 1$) and the branch cut between them collapses. The Riemann surface degenerates into a sphere with two points identified, a singular surface of genus 0. This coincides with one of the loops of the torus becoming contractible to a point, Fig. 2.6.

2.4.1 Integration and topology on torus

The action integrals can be understood as $S = \oint_{\gamma} \lambda$ over classical trajectories, where

$$\lambda(u) = p(\theta) d\theta = p(z) \frac{dz}{iz} = \frac{(z^2 + 2uz + 1)^{1/2}}{iz^{3/2}} dz \quad (2.19)$$

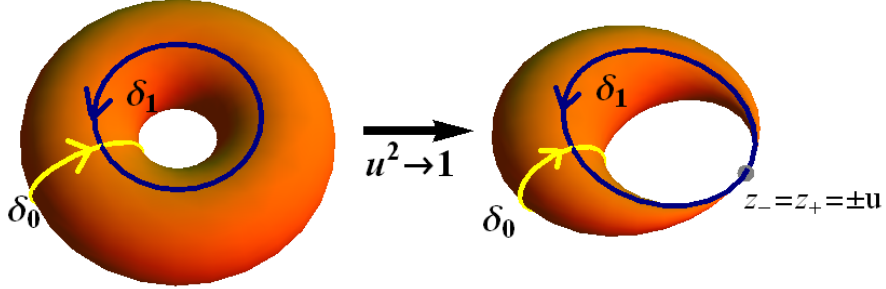


Figure 2.6: Riemann surface of genus-1 with two basic cycles δ_0 and δ_1 on it. In the limit $u \rightarrow \mp 1$ the torus degenerates into a singular surface. This coincides with the loop δ_0 (but not δ_1) becoming contractible to a point.

is the action 1-form which meromorphic on the torus. To visualize the relevant trajectories we momentarily return to θ and consider it as complex. In this representation one has square-root branch cuts along the real axis, connecting the classical turning points. The action integrals run just above or below the real axis in between the turning points. Combining them into closed cycles, one can push these cycles off the real axis and away from the turning points without altering the action integrals (by Cauchy theorem). The two deformed cycles, shown in Fig. 2.7, are hereafter called γ_0 and γ_1 .

Translating these two cycles to the complex z -plane yields the contours of Fig. 2.8. Notice that these are indeed cycles (i.e. closed contours) owing to the crossing of branch cuts. On the Riemann surface both wind around the torus. For this reason, the integrals $S_j(u) = \oint_{\gamma_j} \lambda$ are known as *periods* of \mathcal{E}_u with respect to $\lambda(u)$. One can see that the residue of the action form (2.19) at infinity is zero. Indeed, at large z we have $\lambda \sim dp$. Therefore we can safely deform the contour around infinity in the z -plane. Let us consider cycles δ_0, δ_1 as defined in Fig. 2.6. Any closed cycle on the torus (after appropriate deformation) can be decomposed into a superposition of an integer number of these two basic cycles. For example, the cycles γ_0 and γ_1 are

$$\gamma_0 = \delta_0, \quad \gamma_1 = 2\delta_1 - \delta_0. \quad (2.20)$$

This is evident if one examines the manner in which these cycles encircle around the torus. Formally, the basic cycles generate the first homology group of the torus (since cycles which are alike in this manner are homologous).

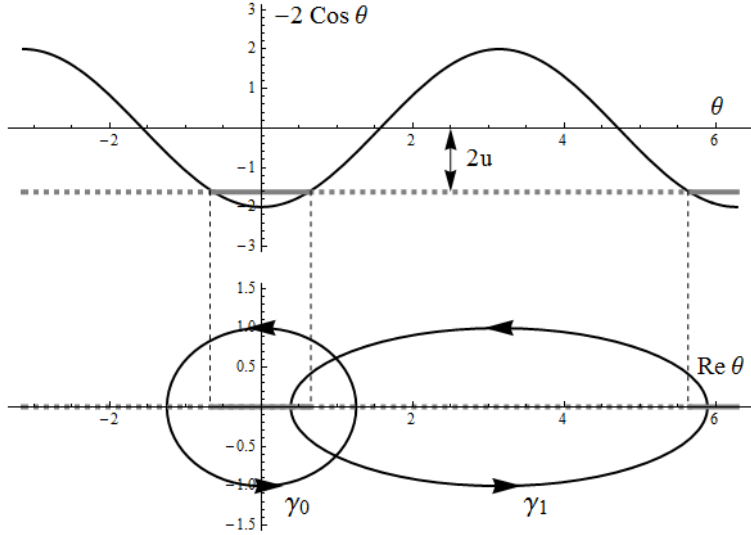


Figure 2.7: The classically allowed (forbidden) region at energy $2u$ are shown by the solid (dashed) gray line. A classical (instanton) periodic orbit, in the complex θ -plane, leads to $\gamma_0(\gamma_1)$ cycles.

One can also consider the first *cohomology* group of the torus, generated by two independent 1-forms on the Riemann surface modulo exact 1-forms (the latter integrate to zero for all cycles on the torus by Stokes' theorem). In this work we consider meromorphic 1-forms with zero residues. Modulo exact forms they are dual to 1-cycles on the torus by the de Rham theorem[34]. The duality implies that there are exactly as many independent 1-forms to integrate *upon* the surface as independent 1-cycles to integrate *along* the surface. For the torus the cohomology, like the homology, is two-dimensional, i.e. any three 1-forms on the torus are linearly dependent up to an exact form.

2.4.2 Picard-Fuchs equation

As a result, there must exist a linear combination of 1-forms $\{\lambda''(u), \lambda'(u), \lambda(u)\}$ which is an exact form, here primes denote derivatives w.r.t. u . This combination may be found by allowing for (u -dependent) coefficients in front of the three 1-forms and looking for an exact form $d_z[P_2(z)z^{-1/2}(z^2 + 2uz + 1)^{-1/2}]$, where $P_2(z)$ is a second degree polynomial with u -dependent coefficients. Matching coefficients for powers of z leads to 5 equations for 6 unknown parameters, determining the sought combination up to an

overall multiplicative factor. This way one finds that the operator $\mathcal{L} = (u^2 - 1)\partial_u^2 + 1/4$ acts on $\lambda(u)$ as

$$\mathcal{L}\lambda(u) = \frac{d}{dz} \left[\frac{i}{2} \frac{1 - z^2}{z^{1/2}(z^2 + 2uz + 1)^{1/2}} \right]. \quad (2.21)$$

It follows from Stokes' theorem and the exactness of $\mathcal{L}\lambda(u)$ that $\mathcal{L}S_j(u) = 0$ since γ_j is a cycle on the torus. Thus $S_j(u)$ satisfies the linear second order ODE[21]

$$(u^2 - 1)S_j''(u) + \frac{1}{4}S_j(u) = 0. \quad (2.22)$$

This is an example of the Picard-Fuchs equation[35, 36] (see Ref. [[37]] for a review). Exactly this equation appears extensively in the context of Seiberg-Witten theory.

Inspecting the coefficient in front of the highest derivative, one notices that equation (2.22) has regular singular points at $u = \infty$ and $u = \mp 1$, where the torus degenerates into a sphere, Fig. 2.6. Changing variable to u^2 , this equation may be brought to the standard hypergeometric form[38]. In the domain $|\arg(1 - u^2)| < \pi$ it admits two

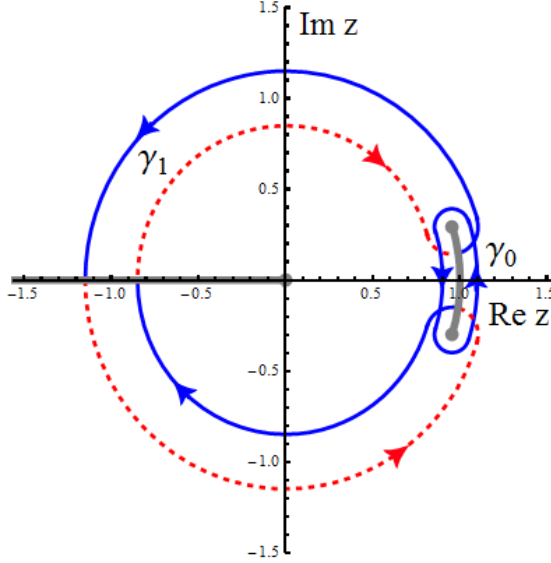


Figure 2.8: Cycles γ_0 and γ_1 on the complex z -plane for $u = -0.9$. Notice that cycle γ_1 crosses twice the two cuts from first branch (solid blue line) to second branch (dashed red line) and back.

linearly independent solutions of the form $F_0(u^2)$ and $uF_1(u^2)$, where

$$F_0(u^2) = {}_2F_1\left(-\frac{1}{4}, -\frac{1}{4}; \frac{1}{2}; u^2\right), \quad (2.23)$$

$$F_1(u^2) = {}_2F_1\left(+\frac{1}{4}, +\frac{1}{4}; \frac{3}{2}; u^2\right). \quad (2.24)$$

These solutions form a basis out of which $S_j(u)$ (and indeed any period of (2.14)) must be composed

$$S_0(u) = C_{00}F_0(u^2) + C_{01}uF_1(u^2), \quad (2.25)$$

$$S_1(u) = C_{10}F_0(u^2) + C_{11}uF_1(u^2). \quad (2.26)$$

To find coefficients C_{jk} , $j, k = 0, 1$ appropriate for the action cycles γ_j one needs to evaluate the periods at one specific value of u . Employing the fact that the hypergeometric functions (2.23–2.24) are normalized and analytic at $u = 0$, i.e. $F_k = 1 + \mathcal{O}(u^2)$, one notices that $S_j(u) = C_{j0} + uC_{j1} + \mathcal{O}(u^2)$. Thus to identify C_{jk} we expand $S_j(u)$ to first order in u and evaluate the integrals at $u = 0$. The corresponding cycles in the z -plane are shown in Fig. 2.9 and explicit calculation yields

$$C_{00} = e^{-i\pi/2}C_{10} = 8\pi^{-1/2}\Gamma(3/4)^2, \quad (2.27)$$

$$C_{01} = e^{+i\pi/2}C_{11} = \pi^{-1/2}\Gamma(1/4)^2. \quad (2.28)$$

The relations between C_{0k} and C_{1k} are not accidental. They originate from the fact that for $u = 0$ the turning points are $\pm i$ and so the cycle γ_1 transforms into γ_0 by substitution $z' = e^{-i\pi}z$, Fig. 2.9. Together with Eqs. (2.25), (2.26) these relations imply global symmetry between the two periods

$$S_0(u) = e^{-i\pi/2}S_1(e^{i\pi}u). \quad (2.29)$$

Equations (2.23)–(2.28) fully determine the two actions $S_{0,1}(u)$ through the hypergeometric functions ¹. One should now relate them to physical observables.

¹Since the integrals considered here are in fact elliptic integrals over a closed cycle, the hypergeometric functions presented here could have been given directly in terms of the complete elliptic integrals of the first and second kind[38].

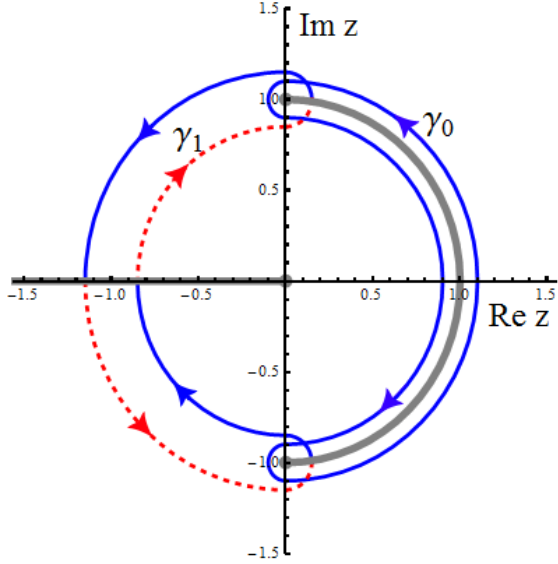


Figure 2.9: The two cycles $\gamma_{0,1}$ for $u = 0$. Here γ_1 may be mapped to γ_0 by rotating 180° .

2.4.3 Structure of $S_j(u)$ near $u = -1$

To this end we consider the structure of $S_j(u)$ in the neighborhood of $u = -1$. As noted earlier, the cycle $\gamma_0 = \delta_0$ contracts to a point as $u \rightarrow -1$ and therefore $S_0(-1) = 0$ by Cauchy's theorem. By contrast, $S_1(-1)$ remains finite. Moreover, while S_0 is analytic near $u = -1$, it turns out that S_1 is not. To see this, choose some $u \gtrsim -1$ and allow u to wind around -1 (i.e. $(u+1) \rightarrow (u+1)e^{2\pi i}$). Since $u \approx -1$ the roots z_\pm in (2.15) are of the form $z_\pm = -1 \pm i\sqrt{2(u+1)}$ we see that this transformation exchanges these branch points via a counter-clockwise half-turn; the branch cut in effect rotates by 180° . For the cycle δ_0 , which encloses the turning cut, this has no effect: the cut turns within it. Not so for δ_1 : as the cut rotates, one must allow δ_1 to continuously deform if δ_1 is never to intersect the branch points. The overall effect is shown in Fig. 2.10. The effect of this *monodromy* transformation is to produce a new cycle δ'_1 . Thus, while we have returned to the initial value of u , the period $S_1(u)$ (unlike $S_0(u)$) does not return to its original value and so $S_1(u)$ cannot be analytic near $u = -1$.

These facts are consistent, of course, with the origin of the integrals as the classical and instanton actions. At $u \rightarrow -1$, the classically allowed region collapses and $p(\theta) \rightarrow 0$,

so the classical action at the bottom of the cosine potential approaches that of the harmonic oscillator $S_0(u) \propto (1+u)$ (indeed the classical period $T \propto \partial_u S_0$ is a constant). For the instanton trajectory γ_1 the action S_1 does not vanish. Moreover as $u \rightarrow -1$ the period on the instanton trajectory is logarithmically divergent since the trajectory goes to the extrema of the cosine potential, Fig. 2.7. This implies that $S_1(u) \propto \text{const} + (1+u) \ln(1+u)$.

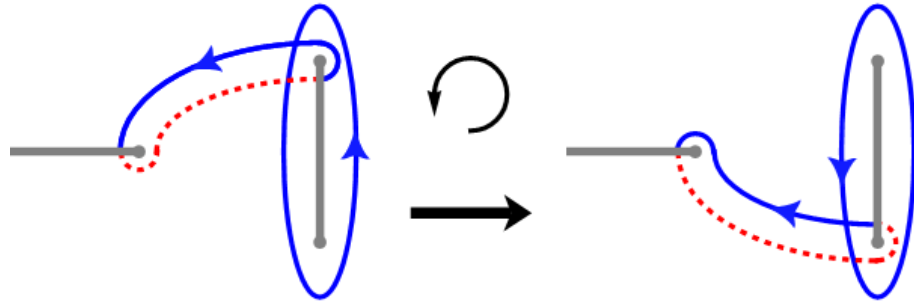


Figure 2.10: Monodromy transformation $(u+1) \rightarrow (u+1)e^{2\pi i}$ rotates the branch cut between $[z_-, z_+]$ by 180° counter-clockwise. This changes the cycle $\delta_1 \rightarrow \delta'_1 = \delta_1 - \delta_0$ along with it.

In fact, more can be said. Under monodromy transformation basis cycle δ'_1 relates to the original basis as $\delta'_1 = \delta_1 - \delta_0$ (as may be seen by counting intersections of cycles or by moving onto the torus). Thus $(\delta_0, \delta_1) \rightarrow (\delta_0, \delta_1 - \delta_0)$. From the decomposition of γ_0, γ_1 noted in (2.20) it follows that the $S_j(u)$ must transform as

$$\begin{pmatrix} S_0(u) \\ S_1(u) \end{pmatrix} \rightarrow \begin{pmatrix} 1 & 0 \\ -2 & 1 \end{pmatrix} \begin{pmatrix} S_0(u) \\ S_1(u) \end{pmatrix} = M_{-1} \begin{pmatrix} S_0(u) \\ S_1(u) \end{pmatrix}, \quad (2.30)$$

where we have introduced the *monodromy matrix* M_{-1} of the actions near $u = -1$. Since this variation of S_1 occurs for every such *monodromy* near $u = -1$, S_1 must have a component which depends logarithmically on $1+u$. Indeed, $\ln(1+u)$ increases by $2\pi i$ under the monodromy and since S_1 changes by $-2S_0$ it must have the following

functional form

$$S_1(u) = Q_1(u) + \frac{i}{\pi} S_0(u) \ln(1+u), \quad (2.31)$$

where $Q_1(u)$ and $S_0(u)$ are analytic functions of $(1+u)$.

As an immediate corollary, one can use the relation (2.29) between S_0 and S_1 to find the structure of the solution near $u = +1$. Then the functional form of $S_0(u)$ near $u = +1$ is $S_0(u) = Q_0(u) - iS_1(u) \ln(1-u)/\pi$, where $Q_0(u) = -iQ_1(-u)$ and $S_1(u) = iS_0(-u)$ are analytic functions of $(1-u)$. The corresponding monodromy matrix is

$$M_1 = \begin{pmatrix} 1 & 2 \\ 0 & 1 \end{pmatrix}. \quad (2.32)$$

While the structure of the periods near $u = \pm 1$ has been shown through geometric reasoning, it may be also found directly by looking for solutions of the Picard-Fuchs equation (2.22) as power series in $(1 \pm u)$. Such a procedure along with the demand of a constant Wronskian leads to a realization that one of the two solutions must include $(1 \pm u) \ln(1 \pm u)$ terms along with the iterative sequence for finding the coefficients of the polynomials. This allows for direct verification of Eq. (2.31).

2.4.4 Semiclassical results

We now seek semiclassical results for the sequence of low-energy bands terminated at $u = -1$. We shall interpret the period $S_0(u)$ which is analytic around $u = -1$ as a classical action. The latter should be quantized according to the Bohr-Sommerfeld rule to determine the normalized energies u_m of the bands

$$S_0(u_m) = 2\pi\alpha^{-1/2}(m + 1/2), \quad m = 0, 1, \dots \quad (2.33)$$

(we shall not discuss the origin of the Maslov index $1/2$ here). The second non-analytic period $S_1(u)$ is identified as the instanton action, which determines the bandwidth $(\Delta u)_m$ according to Gamow's formula

$$(\Delta u)_m = \frac{\omega}{\pi\sqrt{\alpha}} e^{i\alpha^{1/2}S_1(u_m)/2}, \quad (2.34)$$

where $\omega = 2$ is the classical frequency for the Hamiltonian (2.12). The monodromy of u around -1 , Eq. (2.30), carries over to the bandwidth as a factor of $e^{(i/2)\alpha^{1/2}(-2S_0(u_m))}$. Then the Bohr-Sommerfeld quantization (2.33) is also a condition for the bandwidth to be invariant with respect to monodromies.

To illustrate these results we expand the periods Eqs. (2.25)–(2.28) near $u = -1$ to find the physical energy levels $\epsilon_m = 2\alpha u_m$. To first order one finds for $S_0(u)$ and $Q_1(u)$

$$S_0(u) = 2\pi(u + 1), \quad (2.35)$$

$$Q_1(u) = 16i - 2i(u + 1) \ln(32e), \quad (2.36)$$

implying $\epsilon_m = -2\alpha + 2\alpha^{1/2}(m + 1/2)$. As a result the pressure (2.5) of a monovalent gas is

$$P = -eE_0\epsilon_0 = 2k_B T f - \sqrt{k_B T e E_0 f}. \quad (2.37)$$

The two terms here are the pressure of the ideal gas with the fugacity f and the mean-field Debye-Hueckel interaction correction respectively[7].

The instanton action, Eq. (2.31), at quantized u_m is

$$S_1(u_m) = 16i + \frac{2i}{\alpha^{1/2}} \left(m + \frac{1}{2}\right) \ln \left(\frac{m + 1/2}{32e\alpha^{1/2}}\right), \quad (2.38)$$

where the linear term in $Q_1(u)$ has been absorbed into the logarithm. The Gamow formula (3.13) leads to

$$\begin{aligned} (\Delta\epsilon)_m &= 2\alpha(\Delta u)_m = 2\alpha \frac{\omega}{\pi\sqrt{\alpha}} e^{i\alpha^{1/2}S_1(u_m)/2} \\ &= \frac{4}{\pi} \left(\frac{32e}{m + 1/2}\right)^{m+1/2} e^{-8\alpha^{1/2} + (m/2 + 3/4)\ln\alpha}, \end{aligned} \quad (2.39)$$

This coincides with the known asymptotic results for the Mathieu equation[32, 33, 39].

2.4.5 Neighborhood of $u = \infty$

For completeness we also consider the behavior of the actions at high energy. In the limit $u \rightarrow \infty$ the Picard-Fuchs equation (2.22) is of the form $u^2 S''(u) + S(u)/4 = 0$. Seeking a solution in the form $S = u^r$, one finds $r(r-1) + 1/4 = (r-1/2)^2 = 0$ and thus

there must be two independent solutions with the leading behavior $u^{1/2}$ and $u^{1/2} \ln(u)$. So the two periods should be of the form

$$S_i(u) = u^{1/2} [V_i(u) + W_i(u) \ln u] , \quad (2.40)$$

where W_i, V_i are analytic functions of $1/u$. To find these functions one needs to notice that while the continuation to infinity for S_1 is unambiguous, the result obtained for S_0 depends on whether the path to infinity passes above or below $u = 1$. This is due to the fact that S_0 exhibits nontrivial monodromy around $u = 1$, Eq. (2.32). In other words, whether u goes to infinity below or above the real axis determines which of the two turning points z_{\pm} goes to zero or infinity. Since these are also branching points for the torus, the path of analytic continuation determines how the cycles on the torus are carried along in the process.

Thus looking for the asymptotic behavior of the periods (2.25)–(2.28) at $u \rightarrow \infty \pm i0$, one finds[39]

$$V_0(u) = i\pi W_1(u) \mp V_1(u), \quad (2.41)$$

$$W_0(u) = \mp W_1(u), \quad (2.42)$$

$$V_1(u) = 4i\sqrt{2} [\ln(e^2/8) + 2/u], \quad (2.43)$$

$$W_1(u) = -4i\sqrt{2} [1 - (4u)^{-2}], \quad (2.44)$$

to leading corrections in $1/u$. Since $S_0(u) \pm S_1(u) = i\pi W_1(u)u^{1/2}$, from here one may readily show that under the monodromy $u \rightarrow ue^{2\pi i}$ the two actions transform with the following monodromy matrices

$$M_{\infty-i0} = \begin{pmatrix} -3 & 2 \\ -2 & 1 \end{pmatrix}, \quad M_{\infty+i0} = \begin{pmatrix} 1 & 2 \\ -2 & -3 \end{pmatrix}. \quad (2.45)$$

One may check that the three monodromy matrices satisfy

$$M_{\infty-i0} = M_1 \cdot M_{-1}, \quad M_{\infty+i0} = M_{-1} \cdot M_1, \quad (2.46)$$

as expected[38]: winding around 0 in large counter-clockwise circle is the same as winding -1 and 1 sequentially counterclockwise.

From Eqs. (2.40)–(2.44) one finds the unique non-singular period at $u \rightarrow \infty \pm i0$ to be given by $S_0(u) \pm S_1(u) = -i\pi W_1(u)u^{1/2}$. As discussed above, it must be identified with the classical action and subject to Bohr-Sommerfeld quantization $(S_0(u_m) \pm S_1(u_m))/2 = 2\pi\alpha^{-1/2}m$. This leads to $u_m \approx m^2/2\alpha$ and thus $\epsilon_m = 2\alpha u_m = m^2$, as expected for the high energy spectrum.

2.5 Divalent (2,1) gas

The divalent (2,1) gas is the simplest case where the Hamiltonian (2.8) is non-Hermitian. Employing complex variable $z = e^{i\theta}$ and normalized energy $u = 2\epsilon/3\alpha$, it takes the form

$$\frac{3}{2}u = p^2 - \left(\frac{z^2}{2} + \frac{1}{z}\right). \quad (2.47)$$

Similarly to Eq. (2.13) this defines a family of complex algebraic curves

$$\mathcal{E}_u : \quad \mathcal{F}(p, z) = 2p^2z - (z^3 + 3uz + 2) = 0. \quad (2.48)$$

The map $p = p(z)$ is locally holomorphic away from the zeros z_0, z_{\pm} (see Fig. 2.11). At these three branching points as well as at the singularity at $z = 0$ the function $p(z)$ is locally double-valued and behaves as $p \sim (z - z_j)^{1/2}$, $j = 0, \pm$ and $p \sim z^{-1/2}$, respectively. In contrast to the monovalent (1,1) case, Sec. 2.4, the function $p(z)$ is single-valued at $z \sim \infty$ where it goes as $p \sim z$, so no branch cut extends to $z = \infty$. Nevertheless there are again four branching points. To construct the Riemann sphere we draw two branch cuts: one between $[0, z_0]$ and the other between $[z_+, z_-]$. The resulting Riemann surface is again $g = 1$ torus, analogous to Fig. 2.5.

Its moduli space u contains *four* singular points $u = -1, e^{\pm i\pi/3}$ and $u = \infty$, where the torus degenerates into the sphere. (There were only three such points in the (1,1) case.) For $u = -1$ the branching points z_{\pm} coalesce, while for $u = e^{\pm i\pi/3}$ the branching point z_0 collides with z_{\pm} , correspondingly. As $u \rightarrow +\infty$, the branching point z_0 approaches $z = 0$, while $z_{\pm} \rightarrow \pm i\infty$.

The action integrals are again defined as $S_j = \oint_{\gamma_j} \lambda$, where the 1-form $\lambda(u) =$

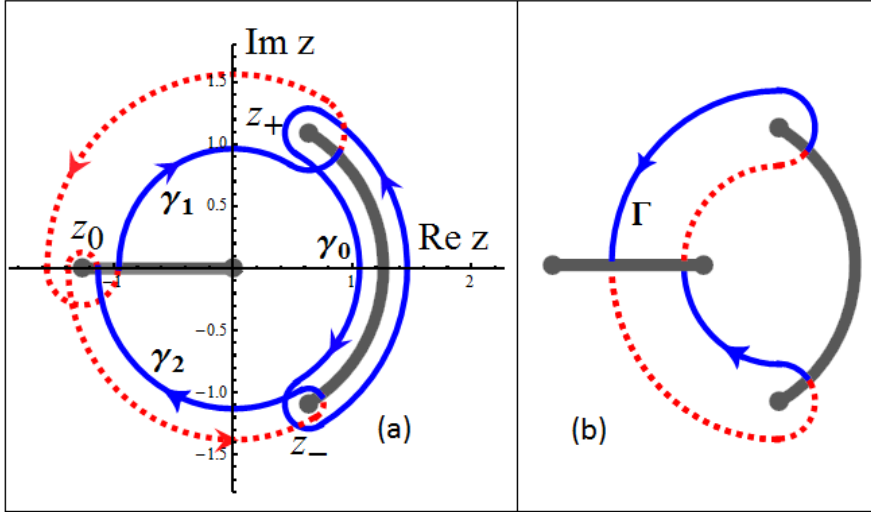


Figure 2.11: (Color online) Complex z -plane with two branch cuts, shown in gray. (a) Three integration cycles $\gamma_0, \gamma_1, \gamma_2$ are displayed for $u = 0$. (b) The instanton cycle $\Gamma = -\gamma_1 + \gamma_2$. The solid blue (dashed red) lines denote parts of the cycles going over the first (second) branch.

$p(z)dz/iz$ is meromorphic on the torus. In general the counterparts of the turning points in the complex θ -plane are not real. This makes it more convenient to discuss the action cycles γ_j in the z -plane. With three turning points z_0, z_\pm , it is convenient to take three paths of integration $\gamma_0, \gamma_1, \gamma_2$, depicted in Fig. 2.11. In terms of the two basic cycles on the torus δ_0, δ_1 , Fig. 2.6, the three paths are given by

$$\gamma_0 = \delta_0, \quad \gamma_1 = -\delta_1 + \delta_0, \quad \gamma_2 = \delta_1. \quad (2.49)$$

One may notice that $\gamma_0 - \gamma_1 - \gamma_2 = 0$, and thus $S_0 = S_1 + S_2$. This equality holds because on a Riemann surface of genus 1 there are only two independent closed cycles. From de Rham's theorem[34] one infers that there are exactly two independent 1-forms. Therefore the three forms $\{\lambda''(u), \lambda'(u), \lambda(u)\}$ are linearly dependent up to an exact form. Following the root outlined in Sec. 2.4.2 (where $P_2(z)$ is replaced with $P_3(z)$) –

polynomial of degree 3), one obtains the Picard-Fuchs equation

$$(u^3 + 1)S_j''(u) + \frac{u}{4} S_j(u) = 0. \quad (2.50)$$

In agreement with the above discussion, there are regular singular points at the third roots of negative unity, i.e. $u = -1, e^{\pm i\pi/3}$ where the coefficient in front of the highest derivative goes to zero, and at $u = \infty$. Two linearly independent solutions $F_0(u^3)$ and $uF_1(u^3)$ of this second-order ODE are given in terms of the hypergeometric functions

$$F_0(u^3) = {}_2F_1\left(-\frac{1}{6}, -\frac{1}{6}; \frac{2}{3}; -u^3\right), \quad (2.51)$$

$$F_1(u^3) = {}_2F_1\left(+\frac{1}{6}, +\frac{1}{6}; \frac{4}{3}; -u^3\right). \quad (2.52)$$

In this basis the three periods $S_j(u)$, where $j = 0, 1, 2$, are given by

$$S_j(u) = C_{j0}F_0(u^3) + C_{j1}uF_1(u^3). \quad (2.53)$$

Since the hypergeometric functions $F_j(u^3 \rightarrow 0) = 1 + \mathcal{O}(u^3)$, one notices that $S_j(u) = C_{j0} + uC_{j1} + \mathcal{O}(u^3)$, as $u \rightarrow 0$. One can thus find constants C_{jk} by explicit evaluation of the actions at $u = 0$, i.e. $C_{j0} = S_j(0)$ and $C_{j1} = S'_j(0)$. The corresponding integration paths are shown in Fig. 2.11 and straightforward integration yields:

$$C_{00} = C_{10}e^{\pi i/3} = C_{20}e^{-\pi i/3} = \frac{2^{11/6}3\pi^{3/2}}{\Gamma(\frac{1}{6})\Gamma(\frac{1}{3})}, \quad (2.54)$$

$$C_{01} = C_{11}e^{-\pi i/3} = C_{21}e^{\pi i/3} = \frac{3^{1/2}\Gamma(\frac{1}{6})\Gamma(\frac{1}{3})}{2^{11/6}\pi^{1/2}}. \quad (2.55)$$

These relations along with Eq. (2.53) imply the three-fold symmetry between the actions, cf. Eq. (2.29),

$$S_0(u) = e^{i\pi/3}S_1\left(e^{-2i\pi/3}u\right) = e^{-i\pi/3}S_2\left(e^{2i\pi/3}u\right). \quad (2.56)$$

Now one needs to connect the periods (2.53) with the quantum spectrum. We start by discussing the real branch of the spectrum terminating at the singular point $u = -1$, Fig. 2.1. As $u \rightarrow -1$, the two branching points z_{\pm} coalesce. As a result γ_0

cycle degenerates to a point, leading to $S_0(u \rightarrow -1) \rightarrow 0$, while $S_{1,2}$ remain finite and actually turn out to be non-analytic. This can be seen by considering the monodromy for a winding of u around -1 , i.e. $(u+1) \rightarrow (u+1)e^{2\pi i}$ (cf. Sec. 3.1). Such a transformation exchanges branching points z_{\pm} by a counter-clockwise 180° -rotation. This leaves the cycle $\delta_0 = \gamma_0$, which encloses these two points, unchanged. On the other hand, the cycle δ_1 picks up a contribution of $-\delta_0$: $\delta'_1 = \delta_1 - \delta_0$. Thus $\gamma_{1,2}$, Eq. (2.49), pick up a contribution of $\pm\delta_0$. As a result, for every monodromy cycle, $S_{1,2}$ pick up a contribution of $\pm S_0$, so locally they are of the form

$$S_{1,2}(u) = Q_{1,2}(u) \mp \frac{i}{2\pi} S_0(u) \ln(1+u), \quad (2.57)$$

where $Q_{1,2}(u)$ and $S_0(u)$ are analytic functions of $(1+u)$ (moreover $Q_1 + Q_2 = S_0$, cf. Eq. (2.49)). This allows us to identify the period $S_0(u) = (\sqrt{6}\pi/2)(1+u) + \mathcal{O}((1+u)^2)$ as the classical action, while the instanton action is a combination of the two non-analytic periods $S_{1,2}(u)$.

The corresponding monodromy matrix M_{-1} in e.g. basis (S_0, S_1) (since $S_2 = S_0 - S_1$ is linearly dependent) is

$$\begin{pmatrix} S_0(u) \\ S_1(u) \end{pmatrix} \rightarrow \begin{pmatrix} 1 & 0 \\ 1 & 1 \end{pmatrix} \begin{pmatrix} S_0(u) \\ S_1(u) \end{pmatrix} = M_{-1} \begin{pmatrix} S_0(u) \\ S_1(u) \end{pmatrix}. \quad (2.58)$$

Employing Eqs. (2.49), (2.56), one finds that at the singular point $e^{i\pi/3}$ ($e^{-i\pi/3}$) the period $S_1(u)$ ($S_2(u)$) is non-singular and goes to zero. It should be thus identified with the classical actions for the branch of the spectrum terminating at the respective singular point, Fig. 2.1. A combination of the remaining two actions S_0 and S_2 (S_1) form the corresponding instanton. The respective monodromy matrices (again in the basis (S_0, S_1)) are found as

$$M_{e^{i\pi/3}} = \begin{pmatrix} 1 & -1 \\ 0 & 1 \end{pmatrix}, \quad M_{e^{-i\pi/3}} = \begin{pmatrix} 2 & -1 \\ 1 & 0 \end{pmatrix}. \quad (2.59)$$

To find positions of the bands along the three branches of the spectrum, terminating at the three singular points $u = -1, e^{\pm i\pi/3}$, one employs Bohr-Sommerfeld quantization

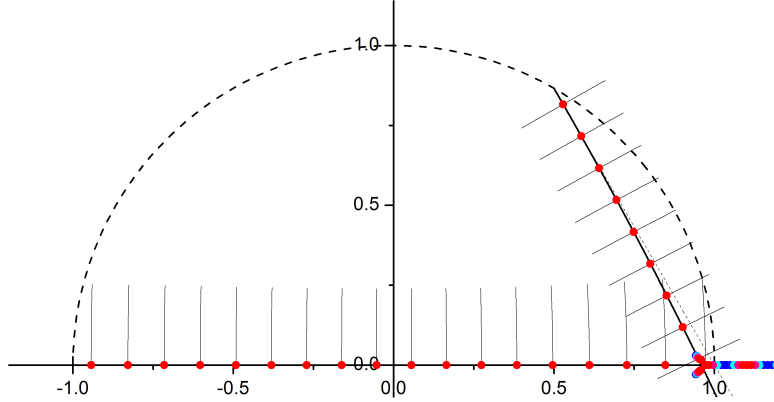


Figure 2.12: (Color online) Narrow energy bands (red dots) in the upper half-plane of complex energy u for $\alpha = 200$, cf. Fig. 2.3a. $\text{Im } S_0(u) = 0$ along the real axis, where the small lines mark $\text{Re } S_0(u) = 2\pi\alpha^{-1/2}(m + 1/2)$. The line $\text{Im } S_1(u) = 0$ emerges from $u = e^{i\pi/3}$ and intersects the real axis at $u \approx 0.96$. To the right of this point we observe bands with narrow gaps and use the same coloring convention as in FIGs. 2.1, 2.3. The small perpendicular lines mark $\text{Re } S_1(u) = 2\pi\alpha^{-1/2}(m + 1/2)$.

for the proper classical action $S_j(u)$ with $j = 0, 1, 2$, correspondingly:

$$S_j(u_m^{(j)}) = 2\pi\alpha^{-1/2}(m + 1/2), \quad m = 0, 1, \dots. \quad (2.60)$$

Figure 2.12 shows the lines $\text{Im } S_0(u) = 0$ and $\text{Im } S_1(u) = 0$ intersected with the set of lines $\text{Re } S_j(u) = 2\pi\alpha^{-1/2}(m + 1/2)$. The numerically computed spectrum sits right at the semiclassical *complex* energies $u_m^{(j)}$. The excellent agreement holds all the way up to the point $u \approx 0.96$, where all three periods S_j happen to be purely real. Beyond this point the semiclassical approximation seems to break down, which manifests in e.g. appearance of wide Bloch bands. Expanding $S_0(u)$ near $u = -1$, one finds for the energy levels $\epsilon_m = 3u_m^{(0)}\alpha/2$ in the semiclassical approximation $\epsilon_m \approx -3\alpha/2 + \sqrt{6\alpha}(m + 1/2)$. The corresponding pressure (2.5) $P = -eE_0\epsilon_0$ consists of the two contributions: the ideal (2, 1) gas and the mean-field Debye-Hueckel interaction correction.

Taking into account that there is no physical difference between S_1 and S_2 and that the monodromy around $u = -1$ in Eq. (2.57) should leave the bandwidth in Gamow's formula (3.13) invariant (i.e. it adds a factor of $\exp\{(i/2)\alpha^{1/2}(-2S_0(u_m^{(0)}))\}$), one identifies the instanton cycle with $\Gamma = -\gamma_1 + \gamma_2$, Fig. 2.11, i.e. $S_{\text{inst}}(u) = -S_1(u) +$

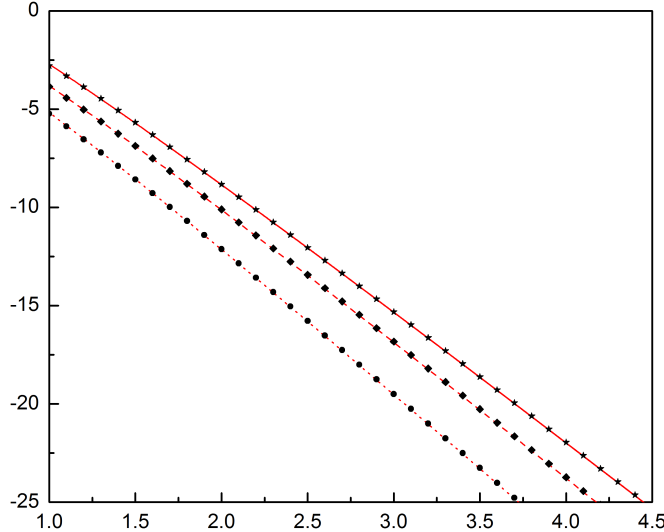


Figure 2.13: (Color online) Analytic (numerical) results for the logarithm of the bandwidth of the lowest band, $\ln(\Delta\epsilon)_0$, versus square-root of the charge concentration, $\sqrt{\alpha}$, with (1, 1) as dotted (circles), (2, 1) dashed (diamonds) and (3, 1) as solid line (stars).

$S_2(u)$. This can be also found by inspecting the cycles in figure 2.11: one sees that the combined $\Gamma = -\gamma_1 + \gamma_2$ cycle connects z_{\pm} turning points through the ‘‘classically forbidden region’’, similarly to γ_1 instanton cycle in (1, 1) case, cf. Fig. 2.8. Note, however, that we do not have a rigorous proof of this fact. Rather our choice of the integration cycle should be considered as an educated guess, which is verified by the numerics.

Expanding $S_{1,2}(u)$ actions near $u = -1$ and substituting $u_m^{(0)}$ from the Bohr-Sommerfeld quantization (2.60) with $j = 0$, one finds for the Bloch bandwidths of the central spectral branch, cf. Eq. (3.13) with $\omega = \sqrt{6}$,²

$$\begin{aligned} (\Delta\epsilon)_m &= \frac{3}{2}\alpha(\Delta u)_m \\ &= \frac{2\sqrt{6}}{\pi} \left(\frac{36\sqrt{6}e}{m + 1/2} \right)^{m+1/2} e^{-3\sqrt{6}\alpha + (m/2 + 3/4)\ln\alpha}. \end{aligned} \quad (2.61)$$

²In writing the Gamow formula above, we conjectured an overall preexponential factor of 4/3 in (2,1) case and 3/2 in (3,1) case compared to the (1,1) case, possibly due to the different structure of the fluctuation determinant. A detailed evaluation of the preexponential factor is beyond the scope of the present work.

Of special interest is the bandwidth of the lowest energy band, due to its direct relation to the transport barrier of the ion channel, Sec. 2.2. Setting $m = 0$ yields

$$(\Delta\epsilon)_0 \approx 34.14 \alpha^{3/4} e^{-7.35\sqrt{\alpha}}. \quad (2.62)$$

This is in very good agreement with the numerical simulations, Fig. 2.13.

Finally we focus on the behavior at $u = \infty$. The Picard-Fuchs equation is of the form $u^3 S'' + uS/4 = 0$. Searching for a solution of the form $S(u) = u^r$ leads to $(r - 1/2)^2 = 0$, signifying two independent solutions with the leading asymptotic $u^{1/2}$ and $u^{1/2} \ln(u)$. Upon the monodromy transformation $u \rightarrow ue^{2\pi i}$ the first of these solutions changes sign, while the second along with the sign change picks up a contribution from the first one. Considering asymptotics of $S_{1,2}(u)$, Eq. (2.53), at $u \rightarrow +\infty$, one finds the following $SL(2, \mathbb{Z})$ monodromy matrix

$$M_\infty = \begin{pmatrix} -1 & 0 \\ 3 & -1 \end{pmatrix}. \quad (2.63)$$

One can check that

$$M_\infty = M_{e^{i\pi/3}} \cdot M_{-1} \cdot M_{e^{-i\pi/3}}, \quad (2.64)$$

as it should be: winding once around 0 in a large counterclockwise rotation is identical to winding counterclockwise in sequence around the other three singular points.

2.6 Trivalent (3,1) gas

The trivalent (3,1) Hamiltonian with the normalized energy u is

$$\frac{4}{3}u = p^2 - \left(\frac{z^3}{3} + \frac{1}{z}\right). \quad (2.65)$$

It gives a family of algebraic curves

$$\mathcal{E}_u : \quad \mathcal{F}(p, z) = 3p^2z - (z^4 + 4uz + 3) = 0 \quad (2.66)$$

over complex (z, p) . They are nonsingular if $u^4 \neq 1$, and so $\mathcal{F}(p, z)$ implicitly defines a locally holomorphic map $p = p(z)$ almost everywhere on (p, z) . In this case there are

six square-root branching points at $z = 0, \infty$ and at the *four* turning points, i.e. four roots of $p^2(z) = 0$.

Hence, while \mathcal{E}_u is a doubly-branched cover of the Riemann sphere, three cuts (instead of two as in the genus-1 case) are required per branch. After opening up cuts and identifying edges under analytic continuation, this leads to a *double torus*, i.e. a sphere with two handles, Fig. 2.14a. Unlike the mono- or di-valent cases, the trivalent channel gives a family of genus-2 Riemann surfaces. The exceptional $u^4 = 1$ cases make \mathcal{E}_u singular at $(p, z) = (0, -u)$, due to collision of two turning points, Fig. 2.14b. So the double torus degenerates into a simple torus with two points identified (a singular surface of genus 1).

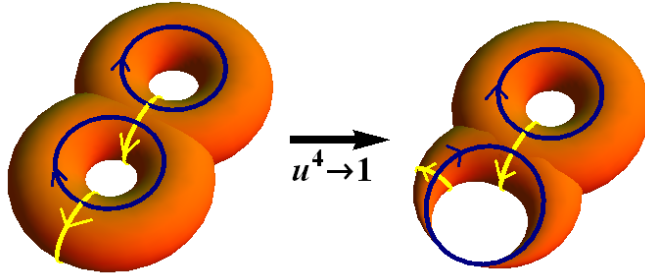


Figure 2.14: (Color online) (a) Double torus curve \mathcal{E}_u for $u^4 \neq 1$, having four basic cycles. (b) When $u^4 = 1$ the $g = 2$ torus degenerates into a singular $g = 1$ surface. This makes one of the basic cycles to pass through the singularity, and renders another cycle contractible to a point.

As in the genus-1 cases, the actions can be understood as integrals $S_j = \oint_{\gamma_j} \lambda$ of the meromorphic action 1-form $\lambda(u) = p(z)(dz/iz)$ upon these Riemann surfaces. Owing to the four turning points, there will be four such cycles γ_j with $j = 0, 1, 2, 3$. These are chosen as in the divalent case, with the inner arcs of each being taken to start on the principal branch. They are shown for $u = 0$ in Fig. 2.15a. The u -dependence of these periods is governed by the Picard-Fuchs equation.

As the double torus is genus-2, there are four independent cycles (as opposed to two for genus-1). So the homology—and so too, as argued before, the cohomology—is not two- but *four*-dimensional: any *five* meromorphic 1-forms on the double torus are linearly dependent up to an exact form. Thus $\lambda(u)$ and its first *four* derivatives can be used to produce an exact form; this is done by finding coefficients in a polynomial

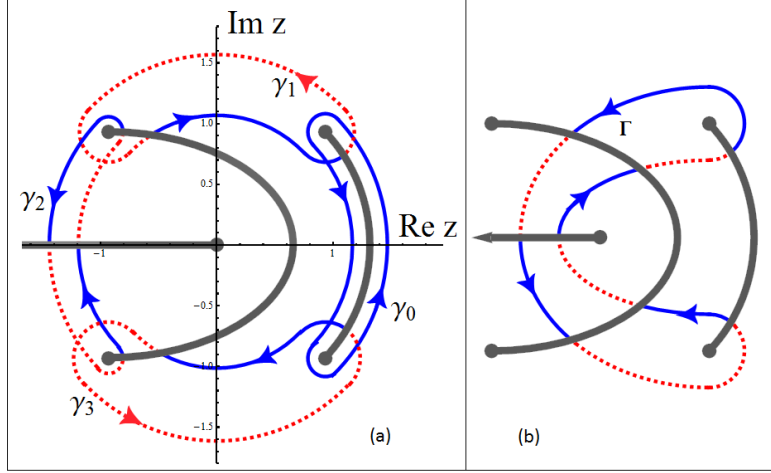


Figure 2.15: (Color online) The Riemann surface is doubly branched with a total of three cuts, shown in gray. The four cycles γ_j with $j = 0, 1, 2, 3$, along with the instanton cycle Γ (defined for later reference) are displayed for $u = 0$. The solid blue (dashed red) lines denote parts of the cycles going over the first (second) branch.

entering the exact form, as discussed in Sec. 2.4.2. Stokes' theorem implies that $S(u) = \oint_\gamma \lambda(u)$ must satisfy a 4th-order linear ODE in u , i.e. Picard-Fuchs equation which in the present case takes the form

$$(u^4 - 1)S^{(4)} + 8u^3 S^{(3)} + \frac{217}{18} u^2 S'' + u S' + \frac{65}{144} S = 0. \quad (2.67)$$

It has regular singular points at fourth roots of 1, i.e. $u \in \{\pm 1, \pm i\}$ and at $u = \infty$. By changing variable to u^4 , one can cast the Picard-Fuchs equation as a *generalized hypergeometric equation*. In the cut domain $|\arg(1 - u^4)| < \pi$ it has four linearly

independent solutions of the form $u^k F_k(u^4)$, where $k = 0, 1, 2, 3$ and

$$F_0(u^4) = {}_4F_3\left(-\frac{1}{8}, -\frac{1}{8}, \frac{5}{24}, \frac{13}{24}; \frac{1}{4}, \frac{1}{2}, \frac{3}{4}; u^4\right), \quad (2.68)$$

$$F_1(u^4) = {}_4F_3\left(+\frac{1}{8}, +\frac{1}{8}, \frac{11}{24}, \frac{19}{24}; \frac{1}{2}, \frac{3}{4}, \frac{5}{4}; u^4\right), \quad (2.69)$$

$$F_2(u^4) = {}_4F_3\left(+\frac{3}{8}, +\frac{3}{8}, \frac{17}{24}, \frac{25}{24}; \frac{3}{4}, \frac{5}{4}, \frac{3}{2}; u^4\right), \quad (2.70)$$

$$F_3(u^4) = {}_4F_3\left(+\frac{5}{8}, +\frac{5}{8}, \frac{23}{24}, \frac{31}{24}; \frac{5}{4}, \frac{3}{2}, \frac{7}{4}; u^4\right), \quad (2.71)$$

are generalized hypergeometric series. Note that the parameters of each ${}_4F_3(\{a_i\}; \{b_j\}; u^4)$ satisfy $\sum b_i - \sum a_i = 1$; such hypergeometric series are known as one-balanced.

Writing the actions in this basis as

$$S_j(u) = \sum_{k=0}^3 C_{jk} u^k F_k(u^4), \quad (2.72)$$

we note that $S_j(u) = \sum_{k=0}^3 C_{jk} u^k + \mathcal{O}(u^4)$ (as generalized hypergeometric functions are unity at zero and analytic nearby). We expand each $S_j(u)$ up to u^3 around $u = 0$ and evaluate the resulting integrals, Fig. 2.15a, to obtain the $\{C_{jk}\}$ ³. For e.g. S_0 this brings

$$C_{00} = +2^{7/2} \cdot 3^{-9/8} \pi^{-1/2} \Gamma(5/8) \Gamma(7/8) \quad (2.73)$$

$$C_{01} = +2^{-1/2} \cdot 3^{-7/8} \pi^{-1/2} \Gamma(1/8) \Gamma(3/8) \quad (2.74)$$

$$C_{02} = -2^{-5/2} \cdot 3^{-13/8} \pi^{-1/2} \Gamma(1/8) \Gamma(3/8) \quad (2.75)$$

$$C_{03} = -7 \cdot 2^{-1/2} \cdot 3^{-27/8} \pi^{-1/2} \Gamma(5/8) \Gamma(7/8) \quad (2.76)$$

When $u = 0$ the turning points satisfy $z^4 + 3 = 0$ and so they lie on a certain circle in the complex plane. Hence γ_j and γ_{j+1} are only different by $\pi/2$ rotation, Fig. 2.15a.

³Note that the integrals that arise at u^2 -order and higher are divergent near the turning points; however, they are convergent near 0 and ∞ and can be calculated by deforming the contours to run between these points.

As a result, we find the four-fold symmetry relations

$$S_0(u) = e^{\frac{\pi i}{4}} S_1(e^{-\frac{\pi i}{2}} u) = e^{\frac{\pi i}{2}} S_2(e^{-\pi i} u) = e^{-\frac{\pi i}{4}} S_3(e^{\frac{\pi i}{2}} u) \quad (2.77)$$

for u in the cut domain $|\arg(1 - u^4)| < \pi$.

We now consider the periods in the neighborhood of $u = -1$. As before, the cycle γ_0 becomes contractible to a point as $u \rightarrow -1$ and therefore $S_0(-1) = 0$ by Cauchy's theorem. The other three actions remain finite, but S_1 and S_3 are non-analytic. This can be seen by considering the monodromy around $u = -1$. As in the genus-1 cases, the shrinking branch cut near $z = 1$ makes a half-turn. Examining the action cycles, it is only γ_1 and γ_3 that intersect the cut rotating under the monodromy within the γ_0 cycle. Hence it is these two cycles that change under monodromy and thus have logarithmic non-analyticity near $u = -1$. More precisely, $(S_1, S_3) \rightarrow (S_1 + S_0, S_3 - S_0)$ under the monodromy and so these actions are of the form

$$S_{1,3}(u) = Q_{1,3}(u) \mp \frac{i}{2\pi} S_0(u) \ln(1 + u), \quad (2.78)$$

where $Q_{1,3}(u)$ as well as $S_0(u)$ and $S_2(u)$ are analytic near $u = -1$. Since $S_1(u) + S_3(u)$ is seen to be invariant under the monodromy, there are a total of three independent periods which have trivial monodromy around $u = -1$. This is again supported by considering series solutions of the Picard-Fuchs equation (2.67) near $u = -1$. This way one finds three regular solutions with leading behavior $(1 + u)^0, (1 + u)^1, (1 + u)^2$ along with an irregular solution with the leading behavior $(1 + u) \ln(1 + u)$. For reasons of space we omit the corresponding 4×4 monodromy matrix.

Although analytical facts about ${}_4F_3$ series are sparse (see [38, 40] for relevant discussion), there are simple consistency checks which our solutions (2.72) must pass. First the vanishing of the classical action $S_0(u)$ at $u = -1$ implies the identity

$$\sum_{k=0}^3 C_{0k} (-1)^k F_k(1) = 0 \quad (2.79)$$

for the hypergeometric functions given above. In addition, from inspection of the Hamiltonian (2.65), one notices that the classical frequency near $u = -1$ is $\omega = \sqrt{8}$. This

implies $S'_0(-1) = \frac{4}{3}(2\pi/\omega)$ and thus

$$\sum_{k=0}^3 C_{0k} \frac{d}{du} \left(u^k F_k(u^4) \right)_{u=-1} = \frac{\sqrt{8}\pi}{3}. \quad (2.80)$$

Being checked numerically, both hold up to 10^{-16} .

Now we turn to the analysis of the spectrum of the Hamiltonian (2.65) at large α . There are three spectral branches terminating at the singular points $u = -1, \pm i$, Fig. 2.3b (notice that the fourth point $u = 1$ lies in the middle of the spectrum and does not have an obvious semiclassical interpretation). To determine positions of the bands we quantize the corresponding actions $j = 0, 1, 3$ (but not $j = 2$, the latter is responsible for the period vanishing at $u = 1$) according to the Bohr-Sommerfeld rule:

$$S_j(u_m^{(j)}) = 2\pi\alpha^{-1/2}(m + 1/2), \quad m = 0, 1, \dots; j = 0, 1, 3. \quad (2.81)$$

Figure 2.16 shows the semiclassical energies $u_m^{(j)}$ along with numerically found energy bands. One notices the perfect agreement between these two for $Re u \lesssim 1.09$. At the point $u \approx 1.09$ all three actions $S_{0,1,3}$ are purely real and the corresponding instanton action (see below) goes through zero. Beyond this point energy bands are not exponentially narrow and semiclassical approximation may not be applicable. Notice that this point is unmistakably different from the singular point $u = 1$. Focusing on the real energies at the bottom of the spectrum and expanding near $u = -1$, one finds with the help of identities (2.79), (2.80) $S_0(u) = (\sqrt{8}\pi/3)(1+u) + \mathcal{O}(1+u)$. The Bohr-Sommerfeld rule (2.81) leads to $\epsilon_m = 4u_m^{(0)}\alpha/3 = -4\alpha/3 + 2\sqrt{2}\alpha^{1/2}(m + 1/2)$. Employing Eq. (2.5), this yields the pressure of the trivalent Coulomb gas as $P = \frac{4}{3}\alpha - \sqrt{2\alpha}$. The two terms here are the ideal gas pressure and the mean-field Debye-Hueckel correction respectively.

Let us now focus on the width of the Bloch bands near $u = -1$. This requires to identify a cycle corresponding to the instanton action. Guided by the cosine potential example, cf. Fig. 2.7, we take the corresponding cycle as connecting the turning points of the classical action S_0 through the “classically forbidden region”. This suggests cycle Γ shown in Fig. 2.15b, which is essentially of the same form as γ_1 instanton cycle in $(1, 1)$ case. One can see that $\Gamma = \gamma_3 - \gamma_2 - \gamma_1$ by considering intersections of these cycles. Upon the monodromy transformation around $u = -1$ the instanton action

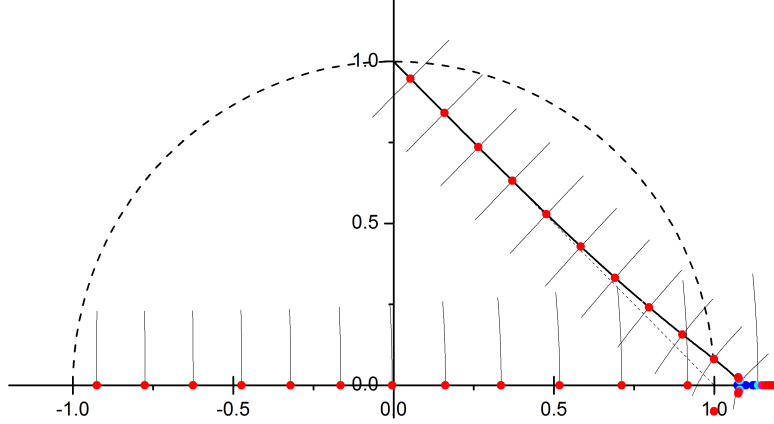


Figure 2.16: (Color online) Narrow energy bands in the upper half-plane of complex energy u for $\alpha = 200$, cf. Fig. 2.3b. $\text{Im } S_0(u) = 0$ along the real axis, where the small lines mark $\text{Re } S_0(u) = 2\pi\alpha^{-1/2}(m + 1/2)$. The line $\text{Im } S_1(u) = 0$ emerges from $u = i$ and intersects the real axis at $u \approx 1.09$. To the right of this point we observe bands with narrow gaps and use the same coloring convention as in FIGs. 2.1, 2.3. The small perpendicular lines mark $\text{Re } S_1(u) = 2\pi\alpha^{-1/2}(m + 1/2)$; red dots, numerically computed narrow bands.

thus acquires a contribution $-2S_0(u)$, Eq. (2.78), which leaves the bandwidth invariant thanks to Bohr-Sommerfeld quantization (2.81). The resulting instanton action is

$$S_{inst}(u) = Q_{inst}(u) + \frac{i}{\pi} S_0(u) \ln(1 + u), \quad (2.82)$$

where $Q_{inst} = Q_3 - S_2 - Q_1$ is the regular part of $S_{inst}(u)$, cf. Eq. (2.78). To first order in $(1 + u)$ this is $Q_{inst}(u_m) \approx 14.12i - 6.71i \cdot (1 + u)$, where e.g. the leading term originates from

$$\begin{aligned} Q_{inst}(-1) &= S_{inst}(-1) \\ &= \sum_{k=0}^3 (C_{3k} - C_{2k} - C_{1k}) (-1)^k F_k(1) \approx 14.12i. \end{aligned}$$

Then, for $u_m^{(0)}$ along the real u -axis satisfying Bohr-Sommerfeld quantization, Gamow's

formula yields for the bandwidth

$$\begin{aligned} (\Delta\epsilon)_m &= \frac{4\alpha}{3}(\Delta u)_m = \frac{4\alpha}{3} \cdot \frac{3\omega}{2\pi\sqrt{\alpha}} e^{i\alpha^{1/2}S_{inst}(u_m)/2} \\ &\approx \frac{4\sqrt{2}}{\pi} \left(\frac{582.88}{m+1/2} \right)^{m+1/2} e^{-7.06\sqrt{\alpha}+(m/2+3/4)\ln\alpha}. \end{aligned} \quad (2.83)$$

The width of the lowest band $(\Delta\epsilon)_0$ is compared with the numerical results in Fig.2.13. As in the earlier cases the two results are in strong accord

For completeness we address the $u = \infty$ behavior. For large u the Picard-Fuchs equation is of the form $u^4 S^{(4)} + 8u^3 S^{(3)} + 217u^2 S''/18 + uS' + 65S/144 = 0$. The trial $S(u) = u^r$ brings four independent solutions with leading asymptotic $\{u^{1/2}, u^{1/2}\ln(u), u^{-5/6}, u^{-13/6}\}$. The former two are familiar from the genus-1 cases, but the latter two are novel to the genus-2 case. The fractional powers $\propto 1/6$ may seem unexpected, given the four-fold symmetries of the periods. However, this symmetry is manifest at the level of cycles at $u = 0$, where four turning points are equally spaced on a circle in the complex z -plane. By contrast, as $u \rightarrow \infty$, the turning points must satisfy either $z^3 \sim -u$ or $1/z \sim -u$, thus only *three* of the four turning points tend towards infinity and one towards zero. This leads to the three-fold exchange of actions upon monodromy around $u = \infty$. Thus the u^r behavior of the periods with $r = -\text{integer}/(2 * 3)$ is exactly what is needed to construct a proper $Sp(4, \mathbb{Z})$ monodromy matrix.

2.7 Higher valence gases

Here we briefly summarize our current state of understanding of the higher valence (4, 1) and (3, 2) gases. The corresponding Hamiltonians are

$$(4,1) : \quad \frac{5}{4}u = p^2 - \left(\frac{z^4}{4} + \frac{1}{z} \right), \quad (2.84)$$

$$(3,2) : \quad \frac{5}{6}u = p^2 - \left(\frac{z^3}{3} + \frac{1}{2z^2} \right). \quad (2.85)$$

In both cases there are *five* turning points in the z -plane given by the equation $p^2(z) = 0$. The behavior at $z = 0$ and $z = \infty$ is somewhat different: for (4, 1) there is a branching point at $z = 0$, but not at $z = \infty$ (cf. (2,1) problem); while for (3, 2) the opposite is true:

there is no branching point at $z = 0$, but there is one at $z = \infty$. In either case there are *six* branching points, which dictate *three* branch cuts. The resulting Riemann surface is the double torus, as in (3, 1) case, Fig. 2.14. In these cases it is not degenerate as long as $u^5 \neq -1$; otherwise two of the five turning points collide, leading to a contraction of one of the cycles. Therefore one expects five branches of the spectrum terminating at $u = (-1)^{1/5}$, in agreement with Figs. 2.3c,d.

Since the Riemann surfaces are genus-2, there is a linear combination of the 1-form $\lambda(u) = p(z)dz/iz$ and its *four* u -derivatives which sum up to an exact form. Therefore any period $S = \oint \lambda$ must satisfy a 4th-order ODE in u . This is found by matching coefficients in a polynomial entering the exact form (see Sec. 2.4.2), yielding the Picard-Fuchs equations

$$(4,1): \quad (u^5 + 1)S^{(4)}(u) + \frac{9u^5 - 1}{u} S^{(3)}(u) + \frac{235}{16} u^3 S''(u) + \frac{5}{4} u^2 S'(u) + \frac{39}{64} u S(u) = 0, \quad (2.86)$$

$$(3,2): \quad (u^5 + 1)S^{(4)}(u) + \frac{9u^5 - 1}{u} S^{(3)}(u) + \frac{140}{9} u^3 S''(u) + \frac{5}{4} u^2 S'(u) + \frac{119}{144} u S(u) = 0. \quad (2.87)$$

While the coefficients seem arbitrary, some features are notable. First, changing variable to u^5 , the equations can be brought to the generalized hypergeometric form; one finds four independent solutions of the form $u^k F_k(u^5)$, where $k = 0, 1, 2, 4$ and F_k being a certain ${}_4F_3$ hypergeometric series⁴. Notice the absence of a $k = 3$ solution. This can be verified directly from the Picard-Fuchs equations, whose leading behavior near $u = 0$ is given by $S^{(4)}(u) - u^{-1} S^{(3)}(u) = 0$. Substituting $S \propto u^k$, one finds $k(k-1)(k-2)(k-4) = 0$.

Second, let us focus on the vicinities of fifth roots of -1 , e.g. on $u = -1$. Notably both Eqs. (2.86),(2.87) have the same leading behavior $5(u+1)S^{(4)}(u) + 10S^{(3)}(u) = 0$, with all other terms are subleading. Looking for a solution in the form $S(u) \sim (1+u)^s$, one finds for the s -exponent $5s(s-1)^2(s-2) = 0$. Therefore in both cases there are

⁴While we omit the parameters of these series for reasons of space, we note that they satisfy the one-balanced condition[40] stated in the (3,1) case.

three analytic solutions with the leading behavior $(1+u)^0, (1+u)^1, (1+u)^2$, while the double root at $s = 1$ signifies that the fourth independent solution is of the form $(1+u)\ln(1+u)$ ⁵.

This observation indicates non-trivial monodromy matrix M_{-1} , allowing one to identify the polynomial in front of the $\ln(1+u)$ with the classical action $S_0(u)$. Being quantized according to Bohr-Sommerfeld, the latter determines the spectrum along the branch terminating at $u = -1$, Figs. 2.3c,d.

Finally, we consider the behavior at $u \rightarrow \infty$. By taking trial solutions in the form $S(u) \sim u^r$, one obtains 4-th order algebraic equations for the exponent r . The four roots of these equations are $\{\frac{1}{2}, \frac{1}{2}, -\frac{3}{4}, -\frac{13}{4}\}$ for $(4, 1)$ case and $\{\frac{1}{2}, \frac{1}{2}, -\frac{7}{6}, -\frac{17}{6}\}$ for $(3, 2)$ case. Remarkably, there is a double degenerate root at $r = 1/2$ in both cases, leading to the two solutions with the leading asymptotic behavior $u^{1/2}$ and $u^{1/2}\ln(u)$. This was also the case in *all* the examples, considered above. The first of these solutions, being quantized, leads to $\epsilon_m = m^2$, expected at large energies. The two other roots bring two additional solutions with the leading behavior $u^{-3/4}, u^{-13/4}$ or $u^{-7/6}, u^{-17/6}$ for $(4, 1)$ and $(3, 2)$ cases, correspondingly. The denominators of these fractional powers may be related with the fact that *four* and *three* turning points go to infinity as $u \rightarrow \infty$ in the two respective cases. The monodromy transformation M_∞ interchanges the corresponding periods (possibly with a sign change). This is achieved by having $-\text{integer}/4$ and $-\text{integer}/(2 \times 3)$ powers in the corresponding solutions.

⁵Existence of $3 = 4 - 1$ analytic solutions near $u = -1$ follows from a theorem of generalized hypergeometric equations going back to Pochammer[38]; the analogous behavior of the mono-, di-, and trivalent gases near $u = -1$ are also instances of this theorem.

Chapter 3

Spin tunneling oscillations of single molecule magnets

3.1 Introduction

In this chapter we move to a new system, that of single molecule magnets (SMM) in an applied magnetic field. The underlying problem, study of systems with large spin J goes back to the works by Harter and Patterson [46, 47]. They realized that the total spin J takes the role of an inverse Planck constant, so for $J \gg 1$ semiclassical treatment is applicable. They studied in great detail a system that corresponds to a SMM without applied magnetic field. Later work by Stone, Garg and others suggests a description in terms of spin-coherent states [42, 44, 45]. There the action for this system is $S = \int \frac{\bar{z}dz - zd\bar{z}}{1 + \bar{z}z}$, where z is the stereographic projection of the spin direction in (θ, ϕ) and \bar{z} its formal complex conjugate [45]. In the case of two classically degenerate minima the quantum mechanical degeneracy is lifted by the presence of instantons. To find an instanton trajectory both θ and ϕ have to be treated as complex variables, which is equivalent to treating the formally complex conjugated (z, \bar{z}) as two *independent* complex variables. This leads to a phase space of complex dimension two. Examples of such calculations in the context of SMM have been given in e.g. [42, 45, 27, 48]. However the procedure is extensive and explicit solutions are only known in a limited class of models.

Our goal is to develop a method to obtain the required action integrals without

explicitly solving the classical equations of motion. Therefore one writes the action as a closed contour integral over complex coordinates in the space of conserved energy. Earlier work [49] exploited the invariance of the integral under canonical transformations to obtain a stable numerical method to calculate the action. Here we demonstrate an analytical solution in a more complex geometry. As was the case in chapter 3.3.2, complex energy conservation restricts the phase space to one complex dimension which can be identified with a Riemann surface. Its genus and specific form is determined by the Hamiltonian. By Cauchy's integral theorem integration in one complex dimension does not depend on the actual path of integration, only its relative position with respect to the singularities and branch points is relevant. The contribution of the singularities can be calculated from their residue values. To calculate the branch point contribution we apply the monodromy concept elaborated in section ; unlike in that case, we will find it necessary to address how poles of the action influence the monodromy transformation. The significant point is that this again strongly constrains the action integrals as analytic functions of the moduli (parameters of the Hamiltonian and energy itself). Here we show that in some examples there are sufficient constraints to fully determine the action integrals. In the following we will review this concept in more detail.

The chapter is organized as follows: section 3.2 presents basic facts about single molecule magnets and spin coherent states, and introduces the specific system that will be discussed below. In section 3.3 we show in detail how geometric reasoning on the Riemann surface allows to solve for the actions only by calculating residues and performing monodromy transformations. The results for energy states, level splitting and its characteristic oscillation with the applied magnetic field in SMM are compared with numerical calculations.

3.2 Single molecule magnets and spin-coherent states

Single-molecule magnets are large molecules with several metallic atoms. Their spins are fixed with respect to each other and thus at low temperatures act like one large spin [52, 53, 54, 55]. One of the most widely studied examples is $[Fe_8O_2(OH)_{12}(tacn)_6]^{8+}$, short name Fe_8 , with a total spin $J = 10$ [56, 57, 58, 48]. The anisotropy of the effective spin Hamiltonian can be derived directly from the molecule's symmetry properties [52],

in an external magnetic field up to leading order it is

$$\hat{\mathcal{H}} = k_1 J_x^2 + k_2 J_y^2 - g\mu_B \vec{J} \cdot \vec{H}. \quad (3.1)$$

In the usual notation $k_1 > k_2 > 0$, therefore x is hard, y medium and z the easy axis. Experimentally, $g \simeq 2$, $k_1 \simeq 0.338K$ and $k_2 \simeq 0.246K$ [56]. It was shown [48] that for full quantitative understanding additional fourth-order anisotropy terms in (3.1) need to be taken into account, but qualitative effects are similar.

Classically there are two degenerate ground states with the spin pointing along the z axis in positive or negative direction. Quantum mechanically this degeneracy is lifted by magnetic quantum tunneling [58, 56]. However the splitting of the two levels oscillates with the strength of the external magnetic field $\vec{H} \parallel \hat{x}$, [56] cf. figure 3.1. This is caused by the presence of two interfering instantons with complex actions. A magnetic field applied along the hard x axis adds a Berry phase to the imaginary part, causing oscillations between constructive and destructive interference and thus of the level splitting [59]. At zero field interference is purely constructive in a system with integer spin and purely destructive with half-integer spin. The latter implies that the two lowest states are perfectly degenerate, which is a manifestation of Kramer's theorem.

The $2J + 1$ spin states are best described by SU(2) spin-coherent states $|z\rangle = e^{zJ_+}|J, -J\rangle$. Here z is a stereographic coordinate of the spin direction, \bar{z} its formal complex conjugate. However these have to be treated as two independent complex variables [42]. The instanton action in spin-coherent states is [48]

$$S = - \int_{\gamma} \left(\frac{\dot{\bar{z}}z - \bar{z}\dot{z}}{1 + \bar{z}z} - \mathcal{H}(z, \bar{z}) \right) dt, \quad (3.2)$$

where

$$\begin{aligned} \mathcal{H}(z, \bar{z}) = \frac{\langle z | \hat{\mathcal{H}} | z \rangle}{J \langle z | z \rangle} = & k_1 \left(J - \frac{1}{2} \right) \left(\frac{1 - \bar{z}z}{1 + \bar{z}z} \right)^2 + k_2 \left(J - \frac{1}{2} \right) \frac{-(\bar{z} - z)^2}{(1 + \bar{z}z)^2} \\ & + \frac{k_1 + k_2}{2} - g\mu_B H \frac{-1 + \bar{z}z}{1 + \bar{z}z} \end{aligned} \quad (3.3)$$

is the expectation value of the Hamiltonian (3.1). The stereographic coordinates (z, \bar{z}) are taken along the x axis, i.e. as projection onto a plane parallel to the yz -plane. The

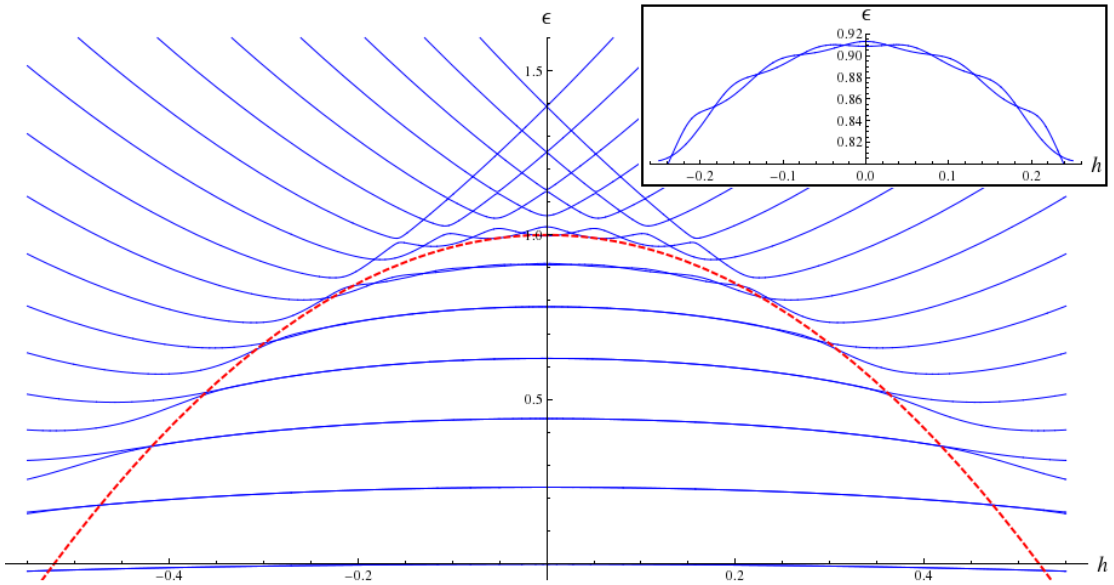


Figure 3.1: Energy levels for $\lambda = 0.728$ and $J = 10$ versus applied magnetic field. The red-dashed line marks the critical value for the field, underneath it pairs of levels are nearly degenerate. The splitting is caused by instantons and oscillates with applied field, the inset shows the example for the sixth pair of levels.

classical equations of motions are obtained by independent variations of this action with respect to z and \bar{z} . The integration path γ runs along a solution of these equations, satisfying a proper boundary conditions. Any such solution conserves the complex energy \mathcal{H} . As a result, the last term in the action (3.2) is always trivial and, in all cases considered below, is a pure phase. The first term is the dynamic contribution. We treat it in the rest of the chapter by developing a method to evaluate it without explicitly knowing the trajectory γ .

3.3 Riemann surface calculations

In this section we evaluate the action integrals on the Riemann surface and use the results to obtain energy levels and their tunneling splitting. To this end we define the new complex coordinates

$$p = \frac{1 - z\bar{z}}{1 + z\bar{z}}; \quad q = \frac{z - \bar{z}}{i(z + \bar{z})}.$$

The 1-form in equation (3.2) is transformed into

$$\sigma = -\frac{zd\bar{z} - \bar{z}dz}{1 + \bar{z}z} = i(1-p)\frac{dq}{1+q^2}, \quad (3.4)$$

and complex energy conservation from equation (3.3) becomes

$$\epsilon = \frac{1}{\lambda}(p-h)^2 + \frac{(1-p^2)q^2}{1+q^2}, \quad (3.5)$$

where we defined $\lambda = k_2/k_1$, $h = \frac{-Hg\mu_B}{2k_1(J-1/2)}$ and $\epsilon = \frac{\mathcal{H}-(k_1+k_2)J/2}{k_2J(J-1/2)} + \frac{k_1h^2}{k_2}$. The shift in \mathcal{H} fixes the classical minimum to $\epsilon = 0$. Kinematics are restricted by energy conservation (3.5), therefore all trajectories are confined to a Riemann surface \mathcal{F} of complex dimension one inside the space of two complex dimensions p, q :

$$\mathcal{F}(p, q) = ((p-h)^2 - \epsilon\lambda)(1+q^2) + \lambda q^2(1-p^2) = 0. \quad (3.6)$$

3.3.1 Analysis of the Riemann surface

To obtain the 1-form (3.4) equation (3.6) is solved for $p = p(q)$:

$$p(q) = \frac{h(1+q^2) \pm \sqrt{\lambda}\sqrt{\epsilon + [\epsilon(2-\lambda) - 1 + h^2]q^2 + [\epsilon - \epsilon\lambda + (h^2 + \lambda - 1)]q^4}}{(1+q^2 - \lambda q^2)}. \quad (3.7)$$

Substituting this into σ in equation (3.4) reduces the problem to integration in one complex variable q . The square root and \pm sign in equation (3.7) imply $p(q)$ is double valued, i.e. the Riemann surface (3.6) has two different sheets. Locally $p(q)$ is single valued and analytic except near the four zeroes of the square root, these are the branch points. To obtain a globally analytic function one connects the branch points pairwise via (arbitrarily chosen) branch cuts and performs analytic continuation of $p(q)$ by jumping to the other sheet of the Riemann surface whenever a cut is crossed. Figure 3.2 shows the complex plane in q with two branch cuts (blue). The cut around the origin along the real axis is labeled the inner branch cut, the cut along the imaginary axis which is closed through ∞ is labeled the outer branch cut. A Riemann surface with two branch cuts has genus $g = 1$ and is topologically a torus.

Besides the branch points there are more special points on the Riemann surface, the

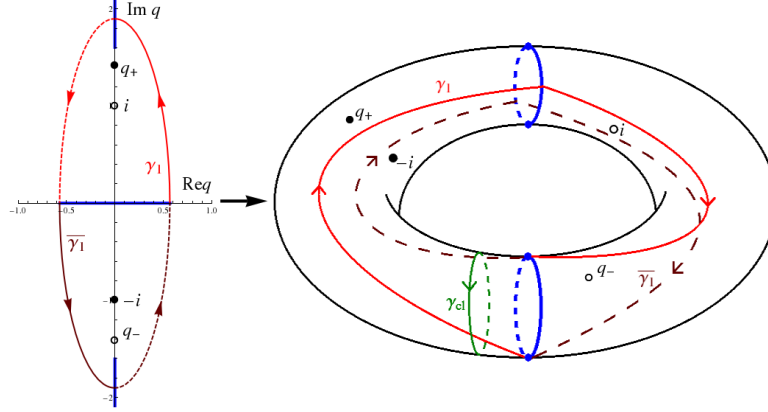


Figure 3.2: (Color online) Left: Plane of complex q for $\lambda = 0.5$, $h = 0.4$ and $\epsilon = 0.1$. The black points are the singularities $\pm i$ and q_{\pm} , where a full (open) point means the non-zero residue is only on the first (second) sheet. The blue lines are the branch cuts, the outer branch cut, along the imaginary axis, is continued to $\pm i\infty$. The instanton trajectories γ_1 ($\bar{\gamma}_1$) in light (dark) red connect two classical turning points (endpoints of inner branch cut) on opposite sheets, where a solid (dashed) line is on the first (second) sheet. Right: The Riemann surface of genus 1 can be seen as a torus. The green trajectory is the classical cycle around the inner branch cut. Combining $\gamma_1 + \bar{\gamma}_1 = \Gamma$ gives a closed instanton trajectory.

singularities in σ . The measure $\frac{dq}{1+q^2}$ diverges at $q = \pm i$, $p(q)$ diverges at $q_{\pm} = \frac{\pm i}{\sqrt{1-\lambda}}$. The residues of σ at these points are easily calculated, but the values differ on the two sheets. Without loss of generality the first sheet is identified so that at $q = 0 + i\delta$ the positive sign in (3.7) is assumed and the square root is evaluated with positive real part, everywhere else the definition follows from analytic continuation. Under this definition the residues of σ are

$$\text{Res}_i^{(2)}(\sigma) = 1, \quad \text{Res}_{-i}^{(1)}(\sigma) = -1, \quad \text{Res}_{q_+}^{(1)}(\sigma) = \frac{h}{\sqrt{1-\lambda}}, \quad \text{Res}_{q_-}^{(2)}(\sigma) = \frac{-h}{\sqrt{1-\lambda}}. \quad (3.8)$$

Here the superscript denotes the sheet on which the poles are on. On the respective other sheet the residues are zero, i.e. these are removable singularities. Therefore there is a total of four poles on the Riemann surface, not four poles per sheet. These are marked in figure 3.2 in black.

3.3.2 Evaluating action integrals

The trajectories live on a Riemann surface with complex dimension one, so by Cauchy's theorem any continuous deformation of the path of integration does not change the value of the integral. Practically this implies one does not need to know the precise path of integration, only its relative position to the branch points and poles.

There are two classically degenerate energy minima of the Hamiltonian (3.1) which are mapped onto the same value $q = 0$, but they are on opposite sheets of the Riemann surface. For non-zero energy spin precession around a classical minimum appears as oscillation around the origin, the inner branch points are the turning points. The classical trajectory goes along the inner branch cut. An instanton trajectory needs to connect two classical turning points on different sheets, i.e. it has to cross the outer branch cut. The two possibilities are $\gamma_1, \bar{\gamma}_1$ in figure 3.2.

Energy levels

The classical action $S_{cl}(\epsilon) = \int_{\gamma_{cl}} \sigma$ is analytic in ϵ , thus it can be expanded in a Taylor series:

$$S_{cl}(\epsilon) = S_{cl}(0) + S'_{cl}(0)\epsilon + \mathcal{O}(\epsilon^2) = \epsilon \oint_{\gamma_{cl}} \partial_\epsilon \sigma|_{\epsilon=0} + \mathcal{O}(\epsilon^2). \quad (3.9)$$

and γ_{cl} may be deformed into a closed trajectory around the inner branch cut. In the limit $\epsilon \rightarrow 0$ both branch points coincide at $q = 0$ and σ is regular in the vicinity. Thus $S_{cl}(0) = 0$ and all derivatives of $S_{cl}(\epsilon)$ only depend on residue values at $q = 0$. For the first derivative

$$\partial_\epsilon \sigma|_{\epsilon=0} = \frac{-i\sqrt{\lambda}dq}{2q\sqrt{1-h^2+(1-h^2-\lambda)q^2}}, \quad (3.10)$$

and calculating the residue gives

$$S_{cl}(\epsilon) = \frac{\pi\epsilon\sqrt{\lambda}}{\sqrt{1-h^2}}. \quad (3.11)$$

The quantization condition $S_{cl} = \frac{2\pi n}{J}$ for spin Hamiltonians in SU(2) [43] determines the energy levels as

$$\epsilon_n = \frac{2n\sqrt{1-h^2}}{J\sqrt{\lambda}}. \quad (3.12)$$

Higher corrections can be easily calculated by evaluating residues of higher ϵ derivatives of σ at $\epsilon = 0$. Thus energy states can be evaluated by the use of a simple residue calculation.

Oscillation period

Two degenerate levels are split by tunneling which goes as

$$\Delta \propto e^{-JS_1} + e^{-J\bar{S}_1} = e^{-J\mathbf{Re}S_1} \cos(\mathbf{Im}S_1), \quad (3.13)$$

where S_1, \bar{S}_1 are the actions of the two instantons $\gamma_1, \bar{\gamma}_1$ in figure 3.2 which are complex conjugated. The imaginary part of S_1 yields an oscillatory term, the real part an overall magnitude. For $\epsilon = 0$ the only contribution to the imaginary part comes from the singularities on the Riemann surface. This can be seen when deforming γ_1 in figure 3.2 to go from the origin along the imaginary axis. It passes two first-order poles at $q = i$ and $q = q_+$, which enter as half-residues when passing in one direction. Contour γ_1 passes them in counter-clockwise direction on their respective sheet, thus

$$i\mathbf{Im}S_1 = \pi i \left(\text{Res}_i^{(2)} + \text{Res}_{q_+}^{(1)} \right) = \pi i \left(1 + \frac{h}{\sqrt{1-\lambda}} \right). \quad (3.14)$$

From equation (3.13) it follows that instantons interfere destructively for $J\mathbf{Im}S_1 = \frac{\pi}{2}, \frac{3\pi}{2}, \dots$, i.e. the condition for the tunneling splitting to be absent (so called "quenching", see Fig. 3.1) is

$$h = \sqrt{1-\lambda} \frac{J - m - \frac{1}{2}}{J}, \quad (3.15)$$

for an integer m . This is in perfect agreement with numerical simulations (see figure 3.5) and the behavior for integer J cited in literature [59]. Here it is derived only out of geometric reasoning, without solving the equations of motion.

For excited levels $\epsilon \neq 0$ there is an additional contribution to the imaginary part from integration along the real axis between the two turning points. The contribution to both γ_1 and $\bar{\gamma}_1$ is half the classical cycle γ_{cl} . Applying the quantization condition for the classical action shows that the additional contribution is $\mathbf{Im}S_1 = \frac{\pi n}{J}$ for the n th level, and the same for \bar{S}_1 . This causes a phase shift of $n\pi$ in the oscillatory part and leaves the level splitting (3.13) unchanged. The quenching condition (3.15) thus also holds for

higher levels. Furthermore every trajectory with the same boundary conditions has the same $\mathbf{Im}S_1$ and a conjugated partner. Therefore condition (3.15) holds to all orders in the semiclassical expansion and is the full quantum mechanical quenching condition. Numerically this holds up to 10^{-15} .

Amplitude of the oscillations

To obtain the real part of S_1 combine $\gamma_1 + \bar{\gamma}_1$ in figure 3.2 into a closed cycle Γ with action $S_{in} = 2\mathbf{Re}S_1$. Then the splitting (3.13) becomes $\Delta \propto e^{-JS_{in}/2} \cos(\mathbf{Im}S_1)$. Straightforward integration along Γ is rather tedious but in complex space an integral is uniquely defined by special points. On the Riemann surface $\mathcal{F}(p, q)$ in (3.6) two branch points collide to make \mathcal{F} degenerate if for a point (p, q) the two derivatives vanish $\partial_p \mathcal{F} = 0$, $\partial_q \mathcal{F} = 0$. This happens if the moduli of the Riemann surface $\mathcal{F} = 0$, i.e. parameters (λ, h, ϵ) , are

$$a) \epsilon = 0, \quad b) \lambda = 0, \quad c) (h \pm 1)^2 = \epsilon\lambda, \quad \text{or} \quad d) 1 - \lambda - h^2 = \epsilon(1 - \lambda). \quad (3.16)$$

For all other values S_{in} is analytic in the moduli. Note that condition *d*) is the case for two branch points colliding at $q = \infty$. The physically relevant range is $0 < \lambda < 1$, small energy $\epsilon > 0$ and fields h below a critical value given by (3.16d). Case (3.16c) is beyond that value and therefore not relevant.

As was the case in chapter , non-analytic contributions can be identified by monodromy transformations, i.e. analytic continuation of the moduli around the critical values (3.16). In the present case, however, we have movable singularities and therefore it seems pertinent to present the concept in full once more. A full monodromy cycle returns the Riemann surface to its initial state, but branch points and singularities move and may exchange position. During a transformation the integration contour should not cross a branch cut or singularity, it rather gets pulled along with the special points. The resulting cycle differs from the original trajectory by an addition of an integer number of basic cycles around the handles of the Riemann surface. These additional cycles are the net change due to the monodromy transformation. Two main examples of monodromies are schematically shown in figures 3.3 and 3.4.

First consider the transformation in only one of the moduli, λ . Therefore assume

$\epsilon = 0^+$ and $h = 0^+$. Note that for $h = 0$ the outer branch points coincide with the singularities q_{\pm} , for $\epsilon = 0$ the inner branch cut collapses into a point at $q = 0$ (cf. figure 3.2).

$\lambda = 0$, (3.16b) Rotating $\lambda \rightarrow \lambda e^{2\pi i}$ rotates the outer branch points around the neighbouring pair of singularities in counter-clockwise direction. The cycle Γ is not affected by this. However the outer branch cut winds around the singularities as schematically shown in figure 3.4. Restoring the original branch cut and singularities inverts the notion of first and second sheet, implying that now Γ is on the opposite sheet. Compared to Γ being on its initial sheet this introduces an overall minus sign:

$$S_{in} \rightarrow -S_{in} \quad \text{for } \lambda \rightarrow \lambda e^{2\pi i} \quad (3.17)$$

Therefore S_{in} is an odd function of $\sqrt{\lambda}$. This implies that $\sqrt{\lambda}$ is rather to be seen as the modulus of the Riemann surface than λ .

$\lambda = 1$, (3.16d) In terms of $\sqrt{\lambda}$ there are two possible monodromies, $(1 \pm \sqrt{\lambda}) \rightarrow (1 \pm \sqrt{\lambda})e^{2\pi i}$. In both cases the two outer branch points exchange position in clockwise direction and Γ obtains two additional cycles similar to figure 3.3. Both go around the inner branch points and all singularities, one clockwise on the first sheet, one counter-clockwise on the second sheet. Only the singularities $\pm i$ contribute with their residue

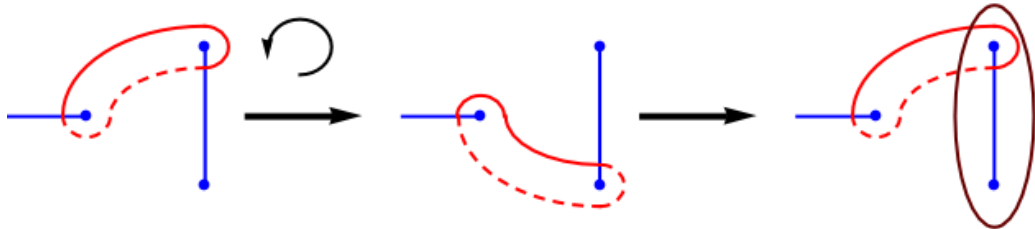


Figure 3.3: Schematics of a monodromy transformation where two branch points (blue) are exchanged. Left: original cycle (red), where the solid (dashed) part is on the first (second) sheet. Middle: The two branch points to the right exchanged counter-clockwise. Right: Constructing the original cycle from the transformed cycle introduces an additional cycle around the branch cut (claret-red).

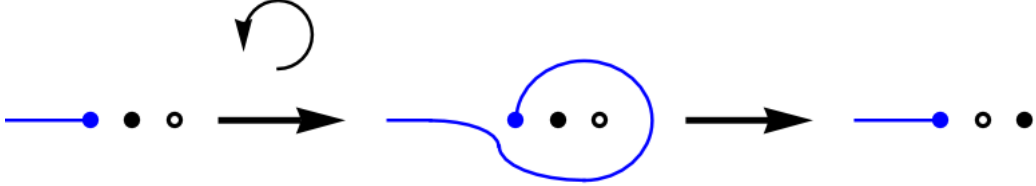


Figure 3.4: Schematics of a monodromy transformation where the branch cut (blue) entangles singularities (black). Left: original branch cut structure, where full (empty) circle is a singularity on first (second) sheet. Middle: The branch cut moved around the singularities counter-clockwise. Right: The branch cut is brought to its original position. During this process both singularities cross the branch cut to the respective other sheet. To restore the initial singularities the notion of first and second sheet is inverted.

values (3.8) to yield

$$\begin{aligned} S_{in} \rightarrow S_{in} + 2 \cdot 2\pi i & \quad \text{for} \quad (1 - \sqrt{\lambda}) \rightarrow (1 - \sqrt{\lambda})e^{2\pi i}, \\ S_{in} \rightarrow S_{in} - 2 \cdot 2\pi i & \quad \text{for} \quad (1 + \sqrt{\lambda}) \rightarrow (1 + \sqrt{\lambda})e^{2\pi i}. \end{aligned} \quad (3.18)$$

Every repeated monodromy cycle causes the same change. The only function that constantly adds the same amount when the phase of the argument is changed is the complex logarithm. Therefore $S_{in}(\sqrt{\lambda})$ needs to contain logarithmic terms as

$$\begin{aligned} S_{in} &= Q_+ + 2 \ln(1 - \sqrt{\lambda}), \\ S_{in} &= Q_- - 2 \ln(1 + \sqrt{\lambda}), \end{aligned} \quad (3.19)$$

where Q_+ (Q_-) is analytic near $\sqrt{\lambda} = 1$ ($\sqrt{\lambda} = -1$).

From these conditions one can obtain S_{in} by identifying Q_\pm . To this end define $g_\pm(\sqrt{\lambda})$ via

$$Q_+(\sqrt{\lambda}) = -2 \ln(1 + \sqrt{\lambda}) + g_+(\sqrt{\lambda}), \quad Q_-(\sqrt{\lambda}) = +2 \ln(1 - \sqrt{\lambda}) + g_-(\sqrt{\lambda}). \quad (3.20)$$

g_\pm are entire functions in $\sqrt{\lambda}$. Equating the two expressions for S_{in} in (3.19) shows $g_+(\sqrt{\lambda}) = g_-(\sqrt{\lambda}) = g(\sqrt{\lambda})$. Similarly equation (3.17) can be used to show $g(\sqrt{\lambda}) = -g(-\sqrt{\lambda})$. Thus $g(0) = 0$ with a well-defined limit. Furthermore in equation (3.5) a

change of $\lambda \rightarrow 1/\lambda$ only is an exchange of coordinate axis $x \leftrightarrow y$. Therefore $g(\sqrt{\lambda})$ is analytic and finite at ∞ , i.e. g is entire and bounded everywhere so by Liouville's theorem $g(\sqrt{\lambda}) = \text{const} = g(0) = 0$. This yields for the instanton action

$$S_{in} = 2 \ln \left(\frac{1 - \sqrt{\lambda}}{1 + \sqrt{\lambda}} \right) = 2\mathbf{Re} S_1. \quad (3.21)$$

This gives the ground state splitting in the zero field limit [59].

Next consider the case with an applied magnetic field $h \neq 0$. This separates the outer branch points from the singularities q_{\pm} which obtain non-zero residue (3.8).

$h \rightarrow -h$, Inverting the sign of h is equivalent to changing the direction of the magnetic field, however the symmetry in (3.1) requires that this leaves the physics unchanged. Therefore

$$S_{in}(-h) = S_{in}(h). \quad (3.22)$$

$\lambda = 0$, **(3.16b)** The monodromy effect is the same as for $h = 0$, therefore equation (3.17) still holds and S_{in} is an odd function in $\sqrt{\lambda}$.

$1 - \lambda - h^2 = 0$, **(3.16d)** There are two possibilities to perform this monodromy in $\sqrt{\lambda}$, namely to rotate around $\pm\sqrt{1-h^2}$. The effect is the same as for $h = 0$, Γ picks up cycles around the inner branch cut and all singularities. The net difference to (3.19) comes from the singularities q_{\pm} which obtain non-zero residues:

$$\begin{aligned} S_{in} &= Q_+ + 2 \left(1 - \frac{h}{\sqrt{1-\lambda}} \right) \ln(\sqrt{1-h^2} - \sqrt{\lambda}), \\ S_{in} &= Q_- - 2 \left(1 - \frac{h}{\sqrt{1-\lambda}} \right) \ln(\sqrt{1-h^2} + \sqrt{\lambda}). \end{aligned} \quad (3.23)$$

Alternatively (3.16d) can be written as $1 - \lambda - h^2 = (1 - h^2)(1 - \lambda) - h^2\lambda = 0$, and the monodromy is performed around $\sqrt{(1-h^2)(1-\lambda)} \pm h\sqrt{\lambda} = 0$. This notion gives the same transformation for the branch points and cycles, the equivalent condition for the

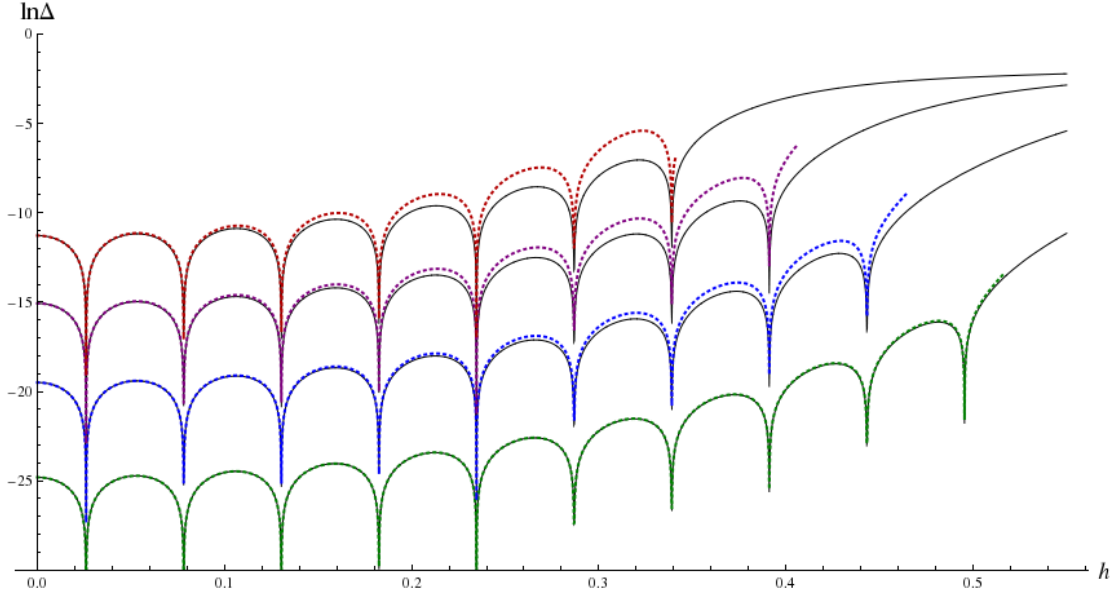


Figure 3.5: Analytic results (dashed, different colors) for the logarithm of the level splitting, compared to numeric calculations (solid-black). Here $\lambda = 0.728$ for the Fe_8 molecule [56].

action becomes

$$\begin{aligned} S_{in} &= \tilde{Q}_+ + 2 \left(1 - \frac{h}{\sqrt{1-\lambda}} \right) \ln(\sqrt{1-h^2}\sqrt{1-\lambda} - h\sqrt{\lambda}), \\ S_{in} &= \tilde{Q}_- - 2 \left(1 - \frac{h}{\sqrt{1-\lambda}} \right) \ln(\sqrt{1-h^2}\sqrt{1-\lambda} + h\sqrt{\lambda}). \end{aligned} \quad (3.24)$$

Again S_{in} is identified by a similar procedure as in equations (3.20) and (3.21). It is easy to see that the term with the constant residue 1 obeys the symmetry properties (3.17) and (3.22) as written in (3.23), the term with residue $h/\sqrt{1-\lambda}$ obeys these as written in equation (3.24). Putting these observations together one finds

$$S_{in} = 2 \ln \left(\frac{\sqrt{1-h^2} - \sqrt{\lambda}}{\sqrt{1-h^2} + \sqrt{\lambda}} \right) - \frac{2h}{\sqrt{1-\lambda}} \ln \left(\frac{\sqrt{1-h^2}\sqrt{1-\lambda} - h\sqrt{\lambda}}{\sqrt{1-h^2}\sqrt{1-\lambda} + h\sqrt{\lambda}} \right). \quad (3.25)$$

In the limit $h \rightarrow 0$ (3.25) reduces to (3.21), as required, and the resulting level splitting is in a perfect agreement with literature [59] and numerical results for the lowest level in figure 3.5 (green).

With the same procedure S_{in} can be found for excited states $\epsilon \neq 0$. The relevant critical moduli are (3.16a), (b) and (d), while (3.16c) is outside the range of parameters.

$\epsilon = 0$, **(3.16a)** Rotating ϵ around zero exchanges the two inner branch points in counter-clockwise direction (see example in 3.3). As net effect, two cycles around the inner branch cut are added to Γ , clockwise on the first sheet and counter-clockwise on the second sheet, i.e. $\Gamma \rightarrow \Gamma - 2\gamma_{cl}$. To obtain an additional term of twice the quantized classical action for every monodromy, S_{in} contains a logarithmic term as

$$S_{in} = Q_\epsilon - \frac{\epsilon\sqrt{\lambda}}{\sqrt{1-h^2}} \ln \epsilon, \quad (3.26)$$

where expression (3.11) for the classical action was used.

$\lambda = 0$, **(3.16b)** Additionally to the previously mentioned change of the sign Γ gets twisted around the inner branch cut and obtains additional contributions of classical cycles $\Gamma \rightarrow -\Gamma - 2\gamma_{cl}$, thus

$$S_{in} \rightarrow -S_{in} - 2S_{cl} \quad \text{for } \lambda \rightarrow \lambda e^{2\pi i}. \quad (3.27)$$

Therefore

$$S_{in} = Q_\lambda - \frac{\epsilon\sqrt{\lambda}}{\sqrt{1-h^2}} \ln \lambda, \quad (3.28)$$

and Q_λ is antisymmetric in $\sqrt{\lambda}$.

$1 - \lambda - h^2 - \epsilon + \epsilon\lambda = 0$, **(3.16d)** The net effect of this monodromy is the same as mentioned above equation (3.18). For this monodromy $\sqrt{\lambda}$ rotates around $\pm\sqrt{1-h^2-\epsilon+\epsilon\lambda}$, the net change to equation (3.23) is the contribution from the classical cycle:

$$\begin{aligned} S_{in} &= Q_+ + 2 \left(1 - \frac{h}{\sqrt{1-\lambda}} - \frac{\epsilon\sqrt{\lambda}}{\sqrt{1-h^2}} \right) \ln(\sqrt{1-h^2-\epsilon+\epsilon\lambda} - \sqrt{\lambda}), \\ S_{in} &= Q_- - 2 \left(1 - \frac{h}{\sqrt{1-\lambda}} - \frac{\epsilon\sqrt{\lambda}}{\sqrt{1-h^2}} \right) \ln(\sqrt{1-h^2-\epsilon+\epsilon\lambda} + \sqrt{\lambda}). \end{aligned} \quad (3.29)$$

Or alternatively

$$\begin{aligned} S_{in} &= \tilde{Q}_+ + 2 \left(1 - \frac{h}{\sqrt{1-\lambda}} - \frac{\epsilon\sqrt{\lambda}}{\sqrt{1-h^2}} \right) \ln(\sqrt{1-h^2-\epsilon}\sqrt{1-\lambda} - h\sqrt{\lambda}), \\ S_{in} &= \tilde{Q}_- - 2 \left(1 - \frac{h}{\sqrt{1-\lambda}} - \frac{\epsilon\sqrt{\lambda}}{\sqrt{1-h^2}} \right) \ln(\sqrt{1-h^2-\epsilon}\sqrt{1-\lambda} + h\sqrt{\lambda}). \end{aligned} \quad (3.30)$$

Now we use the same arguments as below Eq. (3.24) to identify the instanton action of the n th level as

$$\begin{aligned} S_{in} = & - \frac{\epsilon_n\sqrt{\lambda}}{\sqrt{1-h^2}} \ln(\epsilon_n\lambda(1-h^2-\epsilon_n+\epsilon_n\lambda-\lambda)) + 2 \ln \left(\frac{\sqrt{1-h^2-\epsilon_n+\epsilon_n\lambda}-\sqrt{\lambda}}{\sqrt{1-h^2-\epsilon_n+\epsilon_n\lambda}+\sqrt{\lambda}} \right) \\ & - \frac{2h}{\sqrt{1-\lambda}} \ln \left(\frac{\sqrt{1-h^2-\epsilon_n}\sqrt{1-\lambda}-h\sqrt{\lambda}}{\sqrt{1-h^2-\epsilon_n}\sqrt{1-\lambda}+h\sqrt{\lambda}} \right). \end{aligned} \quad (3.31)$$

Here ϵ_n is the energy of the n th level, cf. equation (3.12). This is the full result for the instanton action of excited levels, which agrees with the previous result (3.25) for the ground state $\epsilon_0 = 0$. Figure 3.5 compares the resulting splitting of the first three excited levels (blue, purple, red) to numerical results. For each curve the preexponential factor in (3.13) was chosen constant such that for $h = 0$ the analytic and numerical results agree. The prefactor of the first logarithm comes from first-order approximation to S_{cl} in equation (3.11). Applying the quantization condition in SU(2) allows to replace $\frac{\epsilon_n\sqrt{\lambda}}{\sqrt{1-h^2}} = \frac{2n}{J}$ and make the result precise to higher orders. The analytic result follows the simulated values well: The oscillation period of the quenchings is equal for all levels and agrees perfectly with numerical results. The amplitude agrees well, with discrepancies mostly coming from the approximated value for the energy (the second-order expansion of S_{cl} in ϵ was used), and the effect that for larger h the effective barrier size decreases and semiclassical approximation is expected to become less accurate.

Chapter 4

Universal finite-size scaling in 1D lattice models

4.1 Introduction

Since the introduction of topological order in condensed matter physics, the field of topological insulators received constantly growing attention[63, 64, 65, 66]. Although non-interacting topological phases were fully classified[67, 68, 69] and a plethora of topological edge states characterized[64, 66, 70, 71, 72, 73], little attention was given so far to finite-size effects around the topological transition. An important question is whether finite-size scaling is capable to distinguish between topological indexes and may be used as an indicator of the topological nature of the transition. One may also ask whether such scaling is universal or specific to a particular symmetry class, *e.g.* sensitive to \mathbb{Z} vs. \mathbb{Z}_2 topological index.

In this chapter we depart from the WKB-type analysis of the previous chapters: instead of considering a small effective Planck constant, we consider the asymptotic behavior of large but finite system. Specifically, we discuss the finite-size scaling of the ground state energy across topological phase transitions in 1 + 1 dimensional models. The critical point in such models is described by a conformal field theory[74] (CFT). The finite-size, N , scaling of the ground state energy $E(N, 0)$ for an *open* system at

criticality is known[75, 76] to be

$$E(N, 0) = N \bar{\epsilon}(0) + b(0) - \frac{c}{N} \frac{\pi}{24} + \mathcal{O}(N^{-2}), \quad (4.1)$$

where $\bar{\epsilon}(0)$ is the average bulk energy per particle, $b(0)$ the size-independent boundary term and argument (0) specifies the exact critical point. Here length is measured in units of lattice spacing and energy in units of the Fermi velocity over the lattice spacing. The $1/N$ term appears to be universal and depends only on c – the central charge of the Virasoro algebra[74].

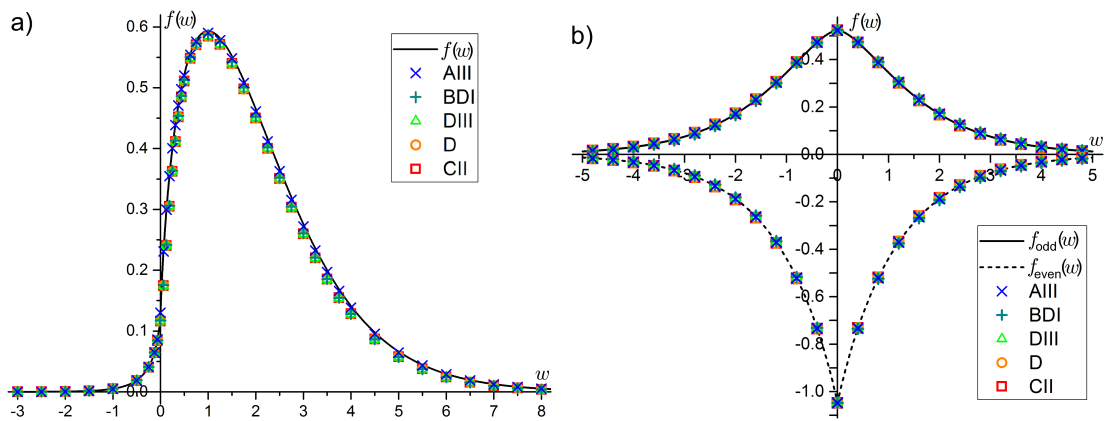


Figure 4.1: (Color online) Numerical results for $f(w)$, where $w = Nm$ and $N = 100$ for 5 topologically non-trivial symmetry classes in one spatial dimension. (a) The case for open boundary conditions which is sensitive to topology, the solid line is the scaling function given by Eq. (4.15). (b) In periodic boundary conditions the results are independent of the topological index and the scaling function Eq. (4.16) is symmetric. There is a difference between even ($f(w)$ negative) and odd ($f(w)$ positive) number of sites $N = 100, 101$.

A relevant perturbation drives the system away from criticality, creating a spectral gap $2m$ and a corresponding correlation length $\xi = 1/m$. Our main observation is that the CFT expansion (4.1) may be generalized as

$$E(N, m) = N \bar{\epsilon}(m) + b(m) - \frac{c}{N} f(Nm) + \mathcal{O}(N^{-2}), \quad (4.2)$$

where in the double scaling limit[77]: $N \rightarrow \infty$ and $m \rightarrow 0$, while $w = Nm = N/\xi = const$, the function $f(w)$, Fig. 4.1, is *universal* for all 5 Altland-Zirnbauer symmetry

classes with non-trivial topology in 1 spatial dimension (AIII, BDI, DIII, D, CII)[67, 68]. Hereafter we identify $m > 0$ with the topological and $m < 0$ with non-topological, or lesser topological index, side of the transition. Most notably, the scaling function for open boundary conditions exhibits markedly distinct behavior on the two sides of the topological transition, while for periodic boundary conditions it is symmetric¹. Curiously, a similar scaling function for the entanglement entropy [78] appears to be symmetric across the topological transition[79], and it is only the N -independent boundary term which is sensitive to the topological index.

One may worry that in the double scaling limit dependence on m of the bulk and boundary terms should not be kept. This is not quite so, because of their singular dependence on the gap. As we explain below

$$\bar{\epsilon}(m) = \bar{\epsilon}(0) - \frac{c}{2\pi} [m^2 + \mathcal{O}(m^4)] \ln \alpha|m|; \quad (4.3)$$

$$b(m) = b(0) + \frac{c}{\pi} [m + \mathcal{O}(m^2)] \ln \alpha_b|m|, \quad (4.4)$$

where α and α_b are non-universal constants. As a result the double scaling limit (4.2) for the energy may be equivalently written as

$$E(N, w) = N \bar{\epsilon}(0) + b(0) + \frac{c \log N}{2\pi N} (2w - w^2) - \frac{c}{N} f_2(w), \quad (4.5)$$

where $f_2(w) = f(w) + \frac{1}{2\pi} (2w \log \alpha_b|w| - w^2 \log \alpha|w|)$ incorporates non-universal terms $\sim w$ and $\sim w^2$. Since these latter may be easily subtracted both numerically and analytically, it is preferable to use the expansion (4.2) with the fully universal function $f(w)$.

4.2 Universality of the scaling function

Before discussing analytic properties of the scaling function $f(w)$ let us focus on our numerical setup and demonstrate the universal behavior for different symmetry classes.

¹Notice that the average energy $\bar{\epsilon}(m)$ is a symmetric function across the transition, while the boundary term $b(m)$ is sensitive to the presence of the edge states and is therefore asymmetric. In periodic boundary conditions the two sides of the transition are physically equivalent.

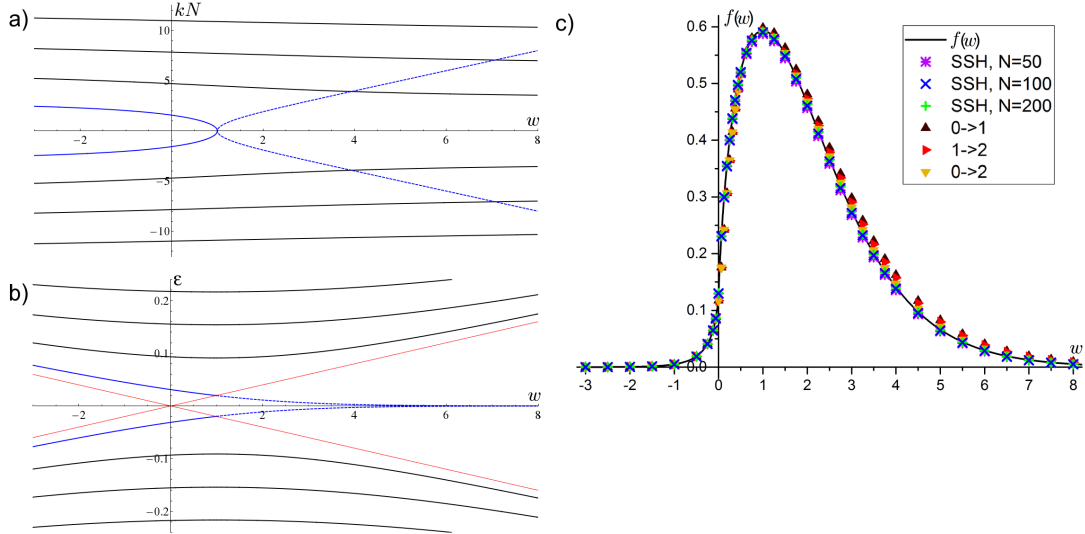


Figure 4.2: (Color online) SSH model (AIII symmetry class): (a) Visualization of the phase shift across the transition. For a fixed $w = Nm$, a state exists with energy $\epsilon^\pm(k)$ if $w = kN \cot(kN)$, Eq. (4.11). In both limits $w \rightarrow \pm\infty$ there are states at $kN = n\pi$, however one pair of states collides at $w = 1$ (blue) and obtains imaginary k , shown as dashed line. (b) Energy spectrum near the gap for a $N = 50$ SSH Hamiltonian (black), with a pair of evolving edge states (blue). The edge state crosses the bulk Dirac cone (thin red) at $w = 1$, where the momentum becomes imaginary. (c) Comparison of numerical results for SSH Hamiltonians with the scaling function (4.15) for system sizes $N = 50, 100, 200$ and three transitions in a 2-chain SSH model with topological indexes $Z = 0 \rightarrow 1, 1 \rightarrow 2, 0 \rightarrow 2$.

We consider models for all five Altland-Zirnbauer symmetry classes which are topologically non-trivial in one dimension[68]. To extract the scaling function we use Eq. (4.2). $E(N, m)$ is the sum of all eigenvalues which are obtained by numerical diagonalization. The average energy $\bar{\epsilon}$ is the integral over the entire Brillouin zone of the dispersion relation for all filled bands, which are calculated from the k-space representation of the Hamiltonian. The boundary term may be also calculated analytically (see below) or alternatively approximated by $b(m) \approx E(N, m) - N\bar{\epsilon}(m)$ for some large N , say $N = 1000$. We have checked that the two ways are in excellent agreement.

In AIII symmetry class we use the standard Su-Schrieffer-Heeger (SSH) tight-binding

Hamiltonian [80, 81]:

$$\mathcal{H}_{AIII} = \sum_{j=1}^N t_1 c_{A,j}^\dagger c_{B,j} + \sum_{j=1}^{N-1} t_2 c_{B,j}^\dagger c_{A,j+1} + h.c. \quad (4.6)$$

Here we choose the gauge for the momentum to have the gap closing at $k = 0$, where the dispersion relation reads $\varepsilon(k) = \pm\sqrt{t_1^2 + t_2^2 - 2t_1 t_2 \cos k}$. For $t_1 \neq t_2$ neighboring sites form dimers, where for $t_1 > t_2$ all sites are part of a dimer, but for $t_1 < t_2$ the two sites at the ends of the chain are unpaired (from now on $m = t_2 - t_1$). Thus there are two distinct phases with topological index $Z = 0$ or $Z = 1$ respectively. The central charge is $c = 1$. In the case of n similar parallel chains the topological index takes values $Z = \{0, 1, \dots, n\}$. Fig. 4.2c shows results for the scaling function at different system sizes, as well as three different transitions ($Z = 0 \rightarrow 1, 0 \rightarrow 2, 1 \rightarrow 2$) in a system with two parallel chains. The results scale with w as the only parameter, and all transitions agree with the analytic result, Eqs. (4.2), (4.15). The numerical results for the class AIII, as well as the four others defined in the next section, are shown in Fig. 4.1 and confirm universality across all five topological classes.

4.3 Different symmetry classes

The other four symmetry classes are defined as follows. The spinless Kitaev chain[82, 83] falls into symmetry class **BDI**. The Hamiltonian is

$$\mathcal{H}_{BDI} = -2\mu \sum_{j=1}^N c_j^\dagger c_j - \sum_{j=1}^{N-1} (tc_j^\dagger c_{j+1} + \Delta c_j c_{j+1}) + h.c., \quad (4.7)$$

where μ is the chemical potential, t a hopping parameter and Δ the pair creation amplitude. For $|\mu| < t$ the system is topological and Majorana edge modes appear, the gap size gives $m = t - |\mu|$. The central charge is $c = 1/2$.

A generalization to spin- $\frac{1}{2}$ fermions with p-wave pairing falls into symmetry class

DIII[84]:

$$\begin{aligned} \mathcal{H}_{DIII} = & -2\mu \sum_{\sigma,j=1}^N c_{j,\sigma}^\dagger c_{j,\sigma} + t \sum_{\sigma,j=1}^{N-1} c_{j,\sigma}^\dagger c_{j+1,\sigma} \\ & + \sum_{j=1}^{N-1} (\Delta_1 c_{j,\uparrow}^\dagger c_{j+1,\uparrow}^\dagger + \bar{\Delta}_1 c_{j,\downarrow}^\dagger c_{j+1,\downarrow}^\dagger) \\ & + \Delta_2 \sum_{\sigma \neq \sigma', j=1}^{N-1} -ic_{j,\sigma}^\dagger c_{j+1,\sigma'}^\dagger + h.c. \end{aligned} \quad (4.8)$$

Here μ is the on-site potential, t hopping parameter and Δ_1, Δ_2 p-wave pairing fields. For $|\mu| < t$ the system is in a topological state, where the gap size gives $m = t - |\mu|$. Due to Kramer's degeneracy all Majorana modes appear in pairs, thus $c = 1$.

Introducing an additional Zeeman splitting of the on-site potential breaks time reversal symmetry and gives a system in **D** symmetry class. Compared to the DIII Hamiltonian we replace the on-site term as follows:

$$\mathcal{H}_D : -2\mu \sum_{\sigma,j=1}^N c_{j,\sigma}^\dagger c_{j,\sigma} \rightarrow -2 \sum_{j=1}^N \mu_1 c_{j,\uparrow}^\dagger c_{j,\uparrow} + \mu_2 c_{j,\downarrow}^\dagger c_{j,\downarrow}. \quad (4.9)$$

The system is topological if $t \in (\mu_1, \mu_2)$, so there are two topological critical points with $c = 1/2$. Focussing on the latter the size of the gap yields $m = t - \mu_2$.

The **CII** symmetry class may be represented by a bipartite tight-binding model for

spin- $\frac{1}{2}$ fermions.

$$\begin{aligned} \mathcal{H}_{CII} = & \mu \sum_{\sigma,j=1}^N (a_{j,\sigma}^\dagger a_{j,\sigma} - b_{j,\sigma}^\dagger b_{j,\sigma}) \\ & + \frac{t_1}{2} \sum_{\sigma,j=1}^{N-1} (a_{j,\sigma}^\dagger a_{j+1,\sigma} - b_{j,\sigma}^\dagger b_{j+1,\sigma}) \\ & + \frac{t_2}{2i} \sum_{j=1}^{N-1} (-a_{j,\uparrow}^\dagger b_{j+1,\downarrow} + a_{j+1,\uparrow}^\dagger b_{j,\downarrow} \\ & \quad + a_{j,\downarrow}^\dagger b_{j+1,\uparrow} - a_{j+1,\downarrow}^\dagger b_{j,\uparrow}) + h.c., \end{aligned} \quad (4.10)$$

where μ is the on-site potential and t_1, t_2 are hopping parameters. The critical point is at $|\mu| = t_1$, with $m = t_1 - \mu$, and the transition is described by a conformal field theory with $c = 1$.

4.4 Analytic properties of the scaling function

Universality of $f(w)$ function is related to the fact that, similarly to the CFT result (4.1), it is fully determined by the vicinity of the critical point. One may thus approximate a near-critical system by the Dirac Hamiltonian e.g. in AIII symmetry class, $\mathcal{H} = m\sigma_1 + i\partial_x\sigma_2$, where the Pauli matrices act in the space of A/B sublattices, cf. Eq. (4.6). Assuming that outside of the interval $0 < x < N$ the mass is very big and, *e.g.*, negative one derives the boundary conditions $\Psi_A(0) = \Psi_B(N) = 0$. The quantized values of $k > 0$ are given by

$$\cos(kN + \delta(k)) = 0; \quad \tan \delta(k) = \frac{m}{k} = \frac{w}{kN}. \quad (4.11)$$

As a result the spectrum is determined by the condition $w \equiv Nm = kN \cot(kN)$, plotted in Fig. 4.2a, and is given by $\epsilon^\pm(k) = \pm\sqrt{m^2 + k^2}$. At $w = 1$ two of its real solutions collide and switch to purely imaginary ones, corresponding to the decaying edge states. Notice that the non-propagating states do not form at $m = 0$, as could be naively expected, but rather at $m = 1/N$.

We now consider the total energy of the filled lower band, still assuming AIII symmetry. This is the sum of all states satisfying Eq. (4.11), with energy obtained substituted in the lower band dispersion relation $\epsilon^-(k) = -\sqrt{t_1^2 + t_2^2 - 2t_1 t_2 \cos k}$. This sum may be converted into an integral with the argument principle:

$$E(N, m) = \frac{1}{2} \oint \frac{dk}{2\pi i} \epsilon^-(k) \partial_k \ln [\cos(Nk + \delta(k))], \quad (4.12)$$

where the contour runs in the complex k -plane encircling all solutions of the quantization condition, see Fig. 4.3. The prefactor $1/2$ is introduced to avoid double counting. The

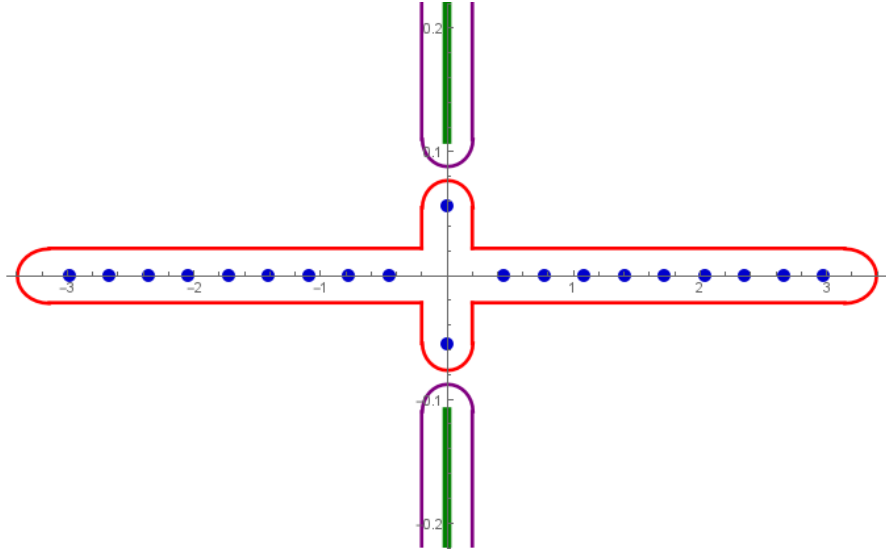


Figure 4.3: Integration contour in the complex k plane for $N = 10$ and $w = 1.1$. The contour (red) encloses all zeroes of the argument of the logarithm (blue) and is to be taken counter-clockwise. After a change of variable $z = Nk$ and taking the scaling limit $N \rightarrow \infty$ the contour runs along the entire real line, above and below. These two parts of the contour are now deformed (purple) to run along the branch cuts of $\sqrt{m^2 + k^2}$ (green).

two pieces of the integration contour above and below the real axis yield the same contribution, in the following we treat these two pieces independently. The contributions proportional to N^1 and N^0 are the bulk and boundary terms, respectively. Writing the

cosine as sum of two exponentials one can factor out these leading contributions to get

$$\begin{aligned} N\bar{\epsilon} + b &= \int (dk/2\pi) \epsilon^-(k) [N + \partial_k \delta(k)] \\ &= \pm \int (dk/2\pi i) \epsilon^-(k) \partial_k \ln e^{\pm i(Nk+\delta(k))}, \end{aligned} \quad (4.13)$$

where the \pm sign is chosen differently above and below the real line so that the remaining exponential term vanishes as $k \rightarrow \pm i\infty$. Now one subtracts $N\bar{\epsilon} + b$ from Eq. (4.12) to find the scaling function $f(w)$,

$$-\frac{f(w)}{N} = \pm \int \frac{dk}{2\pi} \epsilon^-(k) \partial_k \ln \left[1 + e^{\mp 2i(Nk+\delta(k))} \right]. \quad (4.14)$$

In the scaling limit $N \rightarrow \infty$ integration runs along the entire real line and can be seen as closed at infinity. The approximation to the dispersion relation near the Dirac point, $\epsilon^-(k) = \sqrt{m^2 + k^2}$, has a branch cut along the imaginary axis starting at $k = \pm im$. Now one deforms the integration contour to run along this branch cut and redefines the integration variable as $z = \pm ikN$ and introduces $w = Nm$. As a result, in the scaling limit $N \rightarrow \infty$ one finds

$$f(w) = - \int_{|w|}^{\infty} \frac{dz}{\pi} \sqrt{z^2 - w^2} \partial_z \ln \left[1 + e^{-2z-2\delta_w(z)} \right], \quad (4.15)$$

where $\delta_w(z) = -\tanh^{-1}(w/z)$. This expression is plotted in Figs. 4.1a, 4.2c as a full line and is in good agreement with the numerical data.

Before discussing analytic properties of this scaling function let us add a couple of remarks: (i) though the derivation was given for the model in symmetry class AIII, the same logic works for the other symmetry classes. One needs to subtract proper model-dependent bulk and boundary parts, but the scaling term is only determined by the vicinity of the Dirac point and remains unchanged; (ii) a similar derivation may be applied to the case of periodic boundary conditions. In the gauge chosen after equation (4.6) periodic boundary conditions give $\Psi(N) = (-1)^N \Psi(0)$. In this case the quantization condition (4.11) changes to $\cos(kN) = (-1)^N$. After subtracting the bulk energy (there is no boundary term in this case) and following the same steps one arrives

at a similar scaling function:

$$\begin{aligned} f(w) &= -2 \int_{|w|}^{\infty} \frac{dz}{\pi} \sqrt{z^2 - w^2} \partial_z \ln [1 - (-1)^N e^{-z}] \\ &= -\frac{2w}{\pi} \sum_{j=1}^{\infty} \frac{K_1(jw)}{j} (-1)^{jN}, \end{aligned} \quad (4.16)$$

where $K_1(x)$ is the modified Bessel function. This function $f(w)$ is manifestly symmetric across the topological phase transition, as it must be for periodic boundary conditions. However even in the scaling limit $N \rightarrow \infty$ it is dependent on parity of N , see also Fig. 4.1b. The difference may be attributed to the level crossing at the gap closing point $k = 0$ and $w = 0$ for even N , explaining $\sim |w|$ non-analytic behavior of the scaling function. For odd N , all levels undergo avoided crossings and the scaling function is free from such non-analyticity. The CFT result[75, 76] predicts $f(0) = \pi/6$, which agrees with the case for odd N , while for even N we obtain $f(0) = -\pi/3$.

Returning to a system with open boundary conditions, at small $|w| \ll 1$ Eq. (4.15) leads to:

$$f(w) \approx \frac{\pi}{24} + \frac{1}{2\pi} (-2w + w^2) \ln |w| + \dots \quad (4.17)$$

The first term here is in agreement with the CFT limit (4.1). The subsequent terms ensure that $f_2(w)$ function, defined after Eq. (4.5), is analytic. Indeed, at any finite N the ground state energy $E(N, m)$ and all its derivatives must be non-singular at $m = 0$. To derive the second term in Eq. (4.17) one may employ monodromy transformation, which rotates complex w in a small circle around zero[85]. Upon such transformation the right hand side of Eq. (4.15) picks up a contribution given by a closed contour integral around a branch cut $-|w| < z < |w|$ times the number of revolutions. Calculation of such an integral leads to $i(-2w + w^2)$, implying that $f(w)$ must have logarithmic branch cut terminating at $w = 0$ with the discontinuity across it given by this value. Hence Eq. (4.17). We note in passing that in addition to such logarithmic branch cut, $f(w)$ function has an infinite sequence of square root branch cuts along the imaginary w -axis.

At large argument $|w| \gg 1$, i.e. $N \gg |\xi|$, the finite-size corrections decay exponentially. Remarkably the rate of the decay appears to be sensitive to the topology:

$$f(w) \approx \begin{cases} \frac{1}{16\sqrt{\pi}} |w|^{-\frac{1}{2}} e^{-2|w|} & \text{trivial} \quad w \ll -1; \\ 2we^{-w} & \text{topological } w \gg 1. \end{cases} \quad (4.18)$$

(In \mathbb{Z} symmetry classes, the two lines may be attributed to Z and $Z + 1$ topological index.) The fact that on the topological side the scaling function decays half as fast as on the trivial side may be associated with the appearance of the edge states in the middle of the gap and effectively cutting the gap in half. In fact, the purely imaginary solution of $w = kN \cot(kN)$ at $w \gg 1$ gives the energy of the edge states as $\epsilon = \pm 2we^{-w}/N$. This is identical to the asymptotic of $f(w)/N$ on the topological side of the transition, Eq. (4.18), indicating that the latter originates solely from the edge state. In the case of periodic boundary conditions the large w asymptotic is $f(w) = -(-1)^N \sqrt{2/\pi} |w|^{1/2} e^{-|w|}$, which is different from both sides of the transition, Eq. (4.18), in the open boundary condition case.

Furthermore note that there develops a peak at $w = N/\xi = 1$ on the topological side (cf. Fig. 4.1). At this point there is a crossover between the regime of the correlation length being larger than the system size to smaller than the system size. In other words, here the two edge states at opposite ends transform from being delocalized and correlated to localized modes, i.e. the topological transition happens when $m = 1/N$. This manifests itself in Fig. 4.2 as the point where two momenta become imaginary.

Chapter 5

Large deviation statistics of the KPZ equation with weak noise

5.1 Introduction

Large deviation functions of nonequilibrium stochastic systems can exhibit singularities, i.e. non-analytic dependencies on the system parameters. In dynamical systems with a few degrees of freedom the singularities can be associated with the Lagrangian singularities of the underlying optimal fluctuational paths leading to a specified large deviation [87, 88, 89]. In extended macroscopic systems the nature of such singularities, identified as nonequilibrium phase transitions [90, 91, 92], is not yet fully understood. So far several examples of such singularities [93, 94, 95] have been found in stochastic lattice gases: simple microscopic models of stochastic particle transport [96, 97, 98].

Here we uncover a non-analytic behavior in a large-deviation function of the iconic Kardar-Parisi-Zhang (KPZ) equation [99]. This equation represents an important universality class of non-conserved surface growth [100, 101, 102, 103, 104, 105, 106], which is directly accessible in experiment [107, 108]. In 1 + 1 dimension the KPZ equation,

$$\partial_t h = \nu \partial_x^2 h + (\lambda/2) (\partial_x h)^2 + \sqrt{D} \xi(x, t), \quad (5.1)$$

describes the evolution of the interface height $h(x, t)$ driven by a Gaussian white noise $\xi(x, t)$ with zero mean and covariance $\langle \xi(x_1, t_1) \xi(x_2, t_2) \rangle = \delta(x_1 - x_2) \delta(t_1 - t_2)$. Without

loss of generality we will assume that $\lambda < 0$ ¹.

An extensive body of work on the KPZ equation addressed the self-affine properties of the growing interface and the scaling behavior of the interface height at long times [100, 101, 102]. In $1 + 1$ dimension, the height fluctuations grow as $t^{1/3}$, whereas the correlation length scales as $t^{2/3}$. These exponents are hallmarks of the KPZ universality class.

Recently the focus of interest in the KPZ equation in $1 + 1$ dimension shifted toward the complete probability distribution $\mathcal{P}(H, T)$ of the interface height $h(0, T) - h(0, 0) = H$ (in a proper moving frame²) at a specified point $x = 0$ and at *any* specified time $t = T > 0$. This distribution depends on the initial condition [103, 104, 105, 106]. One natural choice of the initial condition is a *stationary* interface: an interface that has evolved for a long time prior to $t = 0$. Mathematically, it is described by a two-sided Brownian interface pinned at $x = 0$. In this case, in addition to averaging over realizations of the dynamic stochastic process, one has to average over all possible initial pinned Brownian interfaces with diffusivity ν . Imamura and Sasamoto [109] and Borodin et al [110] derived exact explicit representations for $\mathcal{P}(H, T)$ in terms of the Fredholm determinants. They also showed that, in the long-time limit and for typical fluctuations, \mathcal{P} converges to the Baik-Rains distribution [111] that is also encountered in the studies of the stationary totally asymmetric simple exclusion process, polynuclear growth and last passage percolation [103].

Here we will be mostly interested in short times. As we show, at short times the interface height exhibits very interesting large-deviation properties. Instead of extracting the short-time asymptotics from the (quite complicated) exact representations [109, 110], we will employ the weak noise theory (WNT) of the KPZ equation [112, 113, 114, 115, 116, 117] which directly probes the early-time regime [118, 119]. In the framework of the WNT, $-\ln \mathcal{P}$ is proportional to the “classical” action over the *optimal path*: the most probable history $h(x, t)$ (a non-random function of x and t) conditioned on the specified large deviation. A crucial signature of the stationary interface is the a priori unknown optimal *initial* height profile which is selected by the system out of a class of functions $h(x, 0)$ carrying certain probabilistic weights and constrained

¹ Changing the sign of λ is equivalent to changing the sign of h .

² The solution of Eq. (5.1) includes a systematic interface displacement $h_s(x, t)$ that comes from the noise rectification by the nonlinearity [136, 106]. Our H is defined as $H = h(0, t) - h_s(0, t)$.

by $h(0, 0) = 0$.

The central result of this chapter is that at short times the optimal path and the optimal initial profile exhibit breaking of a reflection symmetry $x \leftrightarrow -x$ at a certain critical value $H = H_c$. This leads to a non-analytic behavior of the large deviation function of H defined below. This non-analyticity exhibits all the characteristics of a mean-field-like second-order phase transition, where the role of the equilibrium free energy is played by the large deviation function of H . The non-analyticity occurs in the negative (for our choice of $\lambda < 0$) tail of \mathcal{P} . At $|H| \gg |H_c|$ this tail scales as $-\ln \mathcal{P} \sim |H|^{3/2}/T^{1/2}$ and agrees, at any $T > 0$, with the corresponding tail of the Baik-Rains distribution [111]. The latter was previously derived [109, 110] only at long times. Here we show that it is applicable at any time $T > 0$ for $H < 0$ and $|H| \gg |H_c|$.

The rest of the chapter is organized as follows. In Section 5.2 we present the WNT formulation of the problem. Section 5.4 deals with the limit of small H which describes a Gaussian distribution of typical height fluctuations at short times. Section 5.5 describes a numerical algorithm for solving the WNT equations and presents numerical evidence for the symmetry-breaking transition. In Sections 5.6 we present analytical results for large negative H .

5.2 Weak noise theory

Let us rescale $t/T \rightarrow t$, $x/\sqrt{\nu T} \rightarrow x$, and $|\lambda| h/\nu \rightarrow h$. Equation (5.1) becomes

$$\partial_t h = \partial_x^2 h - (1/2)(\partial_x h)^2 + \sqrt{\epsilon} \xi(x, t), \quad (5.2)$$

where $\epsilon = D\lambda^2\sqrt{T}/\nu^{5/2}$ is a dimensionless noise magnitude. We are interested in the probability density of observing $h(x = 0, t = 1) = H$, where H is rescaled by $\nu/|\lambda|$, under the condition that $h(x, 0)$ is a two-sided Brownian interface with $\nu = 1$ and $h(x = 0, t = 0) = 0$. In the physical variables $\mathcal{P}(H, T)$ depends on two parameters $|\lambda|H/\nu$ and ϵ .

The weak-noise theory assumes that ϵ is a small parameter. The stochastic problem for Eq. (5.2) can be formulated as a functional integral which, in the limit of $\epsilon \ll 1$, admits a “semi-classical” saddle-point evaluation. This leads, as will be shown in Section

5.3, to a minimization problem for the action functional $s = s_{\text{in}} + s_{\text{dyn}}$, where

$$s_{\text{dyn}} = \frac{1}{2} \int_0^1 dt \int_{-\infty}^{\infty} dx \left[\partial_t h - \partial_x^2 h + \frac{1}{2} (\partial_x h)^2 \right]^2 \quad (5.3)$$

is the dynamic contribution, and

$$s_{\text{in}} = \int_{-\infty}^{\infty} dx (\partial_x h)^2|_{t=0} \quad (5.4)$$

is the “cost” of the (a priori unknown) initial height profile ³. The ensuing Euler-Lagrange equation can be cast into two Hamilton equations for the optimal path $h(x, t)$ and the canonically conjugate “momentum” density $\rho(x, t)$:

$$\partial_t h = \delta \mathcal{H} / \delta \rho = \partial_x^2 h - (1/2) (\partial_x h)^2 + \rho, \quad (5.5)$$

$$\partial_t \rho = -\delta \mathcal{H} / \delta h = -\partial_x^2 \rho - \partial_x (\rho \partial_x h), \quad (5.6)$$

where

$$\mathcal{H} = \int dx \rho \left[\partial_x^2 h - (1/2) (\partial_x h)^2 + \rho/2 \right]$$

is the Hamiltonian. Equations (5.5) and (5.6) were first obtained by Fogedby [112].

Specifics of the one-point height statistics are reflected in the boundary conditions. The condition $h(x = 0, t = 1) = H$ leads to [115, 118]

$$\rho(x, t = 1) = \Lambda \delta(x), \quad (5.7)$$

where Λ should be ultimately expressed in terms of H . The initial condition for the stationary interface follows from the variation of the action functional s over $h(x, t = 0)$ [122] (see Section 5.3) and takes the form ⁴

$$\rho(x, t = 0) + 2\partial_x^2 h(x, t = 0) = \Lambda \delta(x). \quad (5.8)$$

To guarantee the boundedness of the action, $\rho(x, t)$ and $\partial_x h(x, 0)$ must go to zero

³ The KPZ equation is one of a very few lucky non-equilibrium models where the stationary height distribution, leading to Eq. (5.4), is known (but only in 1d).

⁴ That Λ in Eqs. (5.7) and (5.8) is the same follows from the conservation law $\int_{-\infty}^{\infty} dx \rho(x, t) = \text{const}$ [cf. Eq. (5.6)] and from the boundary condition $\partial_x h(\pm\infty, 0) = 0$ that is necessary for s_{in} to be bounded.

sufficiently rapidly at $|x| \rightarrow \infty$. Finally,

$$h(x = 0, t = 0) = 0. \quad (5.9)$$

Once the optimal path is found, we can evaluate $s = s_{\text{in}} + s_{\text{dyn}}$, where s_{dyn} can be recast as

$$s_{\text{dyn}} = \frac{1}{2} \int_0^1 dt \int_{-\infty}^{\infty} dx \rho^2(x, t). \quad (5.10)$$

This yields \mathcal{P} up to pre-exponential factors: $-\ln \mathcal{P} \simeq s/\epsilon$. In the physical variables

$$-\ln \mathcal{P}(H, T) \simeq \frac{\nu^{5/2}}{D\lambda^2\sqrt{T}} s \left(\frac{|\lambda|H}{\nu} \right). \quad (5.11)$$

As one can see, the action s plays the role of the large deviation function for the short-time one-point height distribution. In section 5.4 we determine the optimal path and s analytically in different limits, and also evaluate these quantities numerically.

5.3 Derivation of the minimization problem

In this section, we give the details by which the minimization problem in section 5.2 is obtained. Using Eq. 5.1, one can express the noise term as

$$\sqrt{D}\xi(x, t) = \partial_t h - \nu \partial_x^2 h - \frac{\lambda}{2} (\partial_x h)^2. \quad (5.12)$$

The probability to encounter such a realization of the Gaussian white noise is given by $\propto e^{-S_{\text{dyn}}/D}$, where

$$\begin{aligned} S_{\text{dyn}} &= \frac{D}{2} \int_0^T dt \int dx \xi^2(x, t) \\ &= \frac{1}{2} \int_0^T dt \int dx \left[\partial_t h - \nu \partial_x^2 h - \frac{\lambda}{2} (\partial_x h)^2 \right]^2. \end{aligned} \quad (5.13)$$

The cost of creating an (a priori unknown) initial interface profile is determined by the stationary height distribution of the KPZ equation:

$$S_{\text{in}} = \nu \int dx (\partial_x h)^2|_{t=0}.$$

For a weak noise and large deviations, the dominant contribution to the total action $S = S_{\text{dyn}} + S_{\text{in}}$ comes from the optimal path $h(x, t)$ that is found by minimizing S with respect to all possible paths $h(x, t)$ obeying the boundary conditions. The variation of the total action is

$$\begin{aligned} \delta S = & \int_0^T dt \int dx \left[\partial_t h - \nu \partial_x^2 h - \frac{\lambda}{2} (\partial_x h)^2 \right] \left(\partial_t \delta h - \nu \partial_x^2 \delta h \right. \\ & \left. - \lambda \partial_x h \partial_x \delta h \right) + 2\nu \int dx \partial_x h \partial_x \delta h|_{t=0}. \end{aligned} \quad (5.14)$$

Let us introduce the momentum density field $\rho(x, t) = \delta L / \delta v$, where $v \equiv \partial_t h$, and

$$L\{h\} = \frac{1}{2} \int dx \left[\partial_t h - \nu \partial_x^2 h - \frac{\lambda}{2} (\partial_x h)^2 \right]^2$$

is the Lagrangian. We obtain

$$\rho(x, t) = \partial_t h - \nu \partial_x^2 h - \frac{\lambda}{2} (\partial_x h)^2 \quad (5.15)$$

and arrive at

$$\partial_t h = \nu \partial_x^2 h + \frac{\lambda}{2} (\partial_x h)^2 + \rho, \quad (5.16)$$

the first of the two Hamilton equations of the weak-noise theory (WNT). Now we can rewrite the variation (5.14) as follows:

$$\begin{aligned} \delta S = & \int_0^T dt \int dx \rho (\partial_t \delta h - \nu \partial_x^2 \delta h - \lambda \partial_x h \partial_x \delta h) \\ & + 2\nu \int dx \partial_x h \partial_x \delta h|_{t=0}. \end{aligned}$$

Demanding $\delta S = 0$ and performing integrations by parts, one obtains the Euler-Lagrange equation, which yields the second Hamilton equation of the WNT:

$$\partial_t \rho = -\nu \partial_x^2 \rho + \lambda \partial_x (\rho \partial_x h). \quad (5.17)$$

The boundary terms in space, resulting from the integrations by parts, all vanish. The boundary terms in time must vanish independently at $t = 0$ and $t = T$. Both $h(x, t = 0)$,

and $h(x, t = T)$ are arbitrary everywhere except at $x = 0$ where they are fixed by the conditions

$$h(x = 0, t = 0) = 0 \quad \text{and} \quad h(x = 0, t = T) = H. \quad (5.18)$$

This leads to the following boundary conditions:

$$\rho(x, t = 0) + 2\nu\partial_x^2 h(x, t = 0) = \Lambda\delta(x), \quad (5.19)$$

$$\rho(x, t = T) = \Lambda\delta(x), \quad (5.20)$$

where Λ is an auxiliary parameter that should be finally set by the second relation in Eq. (5.20). An evident additional condition, $\partial_x h(|x| \rightarrow \infty, t) = 0$, is necessary for the boundedness of S_{in} . Once the WNT equations are solved, the desired probability density is given by

$$\begin{aligned} -\ln \mathcal{P}(H, T) &\simeq \frac{S}{D} \\ &= \frac{1}{2D} \int_0^T dt \int dx \rho^2(x, t) + \frac{\nu}{D} \int dx (\partial_x h)^2|_{t=0}. \end{aligned} \quad (5.21)$$

The rescaling transformation

$$t/T \rightarrow t, \quad x/\sqrt{\nu T} \rightarrow x, \quad |\lambda| h/\nu \rightarrow h, \quad |\lambda| T p/\nu \rightarrow p \quad (5.22)$$

brings Eqs. (5.16) and (5.17) to the rescaled form of Eq. 5.6. The boundary condition (5.19) becomes Eq. 5.8, with a rescaled Λ . The rest of boundary conditions remain the same.

5.4 Small- H expansion

For sufficiently small H the WNT problem can be solved via a regular perturbation expansion in the powers of H , or Λ [118, 119, 123]. One writes $h(x, t) = \Lambda h_1(x, t) + \Lambda^2 h_2(x, t) + \dots$ and similarly for $\rho(x, t)$, and obtains an iterative set of coupled linear partial differential equations for h_i and ρ_i . These equations can be solved order by order with the standard Green function technique [118]. The leading order corresponds to the

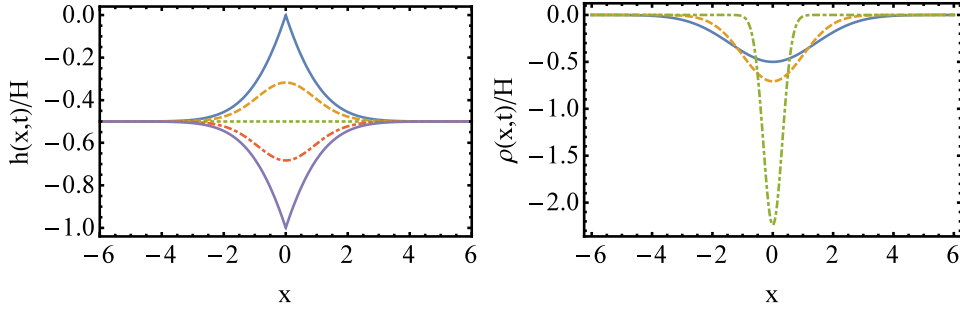


Figure 5.1: The optimal path in the linear approximation, as described by Eqs. (5.25) and (5.26) for $H < 0$, at $t = 0, 0.25, 0.5, 0.75$ and 1 (top panel, from top to bottom) and $t = 0, 0.5$ and 0.95 (bottom panel).

WNT of the Edwards-Wilkinson equation [124]:

$$\partial_t h_1 = \partial_x^2 h_1 + \rho_1, \quad (5.23)$$

$$\partial_t \rho_1 = -\partial_x^2 \rho_1, \quad (5.24)$$

with the boundary conditions $\rho_1(x, 0) + 2\partial_x^2 h_1(x, 0) = \rho(x, 1) = \delta(x)$ and $h_1(0, 0) = 0$. This is a simple problem, and one obtains in this order $\Lambda \simeq \sqrt{\pi}H$, and

$$h(x, t) \simeq \frac{H}{4} \left[2 + xf \left(\frac{x}{2\sqrt{t}} \right) - xf \left(\frac{x}{2\sqrt{1-t}} \right) \right], \quad (5.25)$$

$$\rho(x, t) \simeq \frac{H}{2\sqrt{1-t}} e^{-\frac{x^2}{4(1-t)}}, \quad (5.26)$$

where $f(z) = \sqrt{\pi} \operatorname{erf}(z) + z^{-1} e^{-z^2}$, see Fig. 5.1. Noticeable in Eq. (5.25) is a time-independent plateau $h(\pm\infty, t) = H/2$. Importantly for the following, $h(x, t)$ and $\rho(x, t)$ are, at all times, symmetric functions of x . Although the KPZ nonlinearity appears already in the second order of the perturbation theory, the reflection symmetry $x \leftrightarrow -x$ of the optimal path persists in *all* orders. Therefore, within its (a priori unknown) convergence radius, the perturbation series for $s(H)$ comes from a unique optimal path which respects the reflection symmetry. Note for comparison that the *time-reversal* symmetry $t \leftrightarrow 1 - t$ of $h(x, t)$, present in the first order in H , is violated already in the second order, reflecting the lack of detailed balance in the KPZ equation.

Using Eqs. (5.3) and (5.4), one obtains, in the first order, $s(H) \simeq \sqrt{\pi}H^2/2$. Therefore, as is well known, the body of the short-time distribution $\mathcal{P}(H, T)$ is a Gaussian with the variance $(D^2T/\pi\nu)^{1/4}$ that obeys the Edwards-Wilkinson scaling [124]. This variance is larger by a factor $\sqrt{2}$ than the variance for a flat initial interface, as observed long ago [125]. Indeed, a flat interface is *not* the optimal initial configuration for the stationary process, see Fig. 5.1.

5.5 Phase transition at $H < 0$: numerical evidence

To deal with finite H we used a numerical iteration algorithm [126, 127] which cyclically solves Eq. (5.6) backward in time, and Eq. (5.5) forward in time, with the initial conditions (5.7) and (5.8), respectively. At the very first iteration of Eq. (5.6) one chooses a reasonable “seed” function for $h(x, t)$ and keeps iterating until the algorithm converges. For small $|H|$ we used the linear theory, described above, to choose such a seed. We then used $h(x, t)$, obtained upon convergence of the algorithm for a given H , as a seed for a slightly larger value H , *etc.*

For sufficiently small $|H|$ the algorithm converges to a reflection-symmetric optimal path resembling (or, for still smaller $|H|$, almost coinciding with) the one shown in Fig. 5.1. The reflection symmetry is also intact for *any* positive H , although the optimal solution strongly deviates from the small- H solution of Sec. 5.4 once $H > 1$.

At sufficiently large *negative* H the symmetric solution loses stability, and the algorithm converges to one of two solutions with a *broken* reflection symmetry. Each of these two solutions has unequal plateaus at $|x| \rightarrow \pm\infty$, see Figs. 5.2 and 5.3, and is a mirror reflection of the other around $x = 0$.

To characterize the symmetry breaking we introduced an order parameter

$$\Delta = h(\infty, t) - h(-\infty, t) = \int_{-\infty}^{\infty} dx \partial_x h(x, t), \quad (5.27)$$

which is a conserved quantity, as one can check from Eq. (5.5). Our numerical results for $|\Delta|$ vs. $|H|$ at $H < 0$ are shown in the left panel of Fig. 5.4. They indicate a phase transition at a critical value $H = H_c$. At $|H| \leq |H_c|$ $\Delta = 0$, in agreement with the

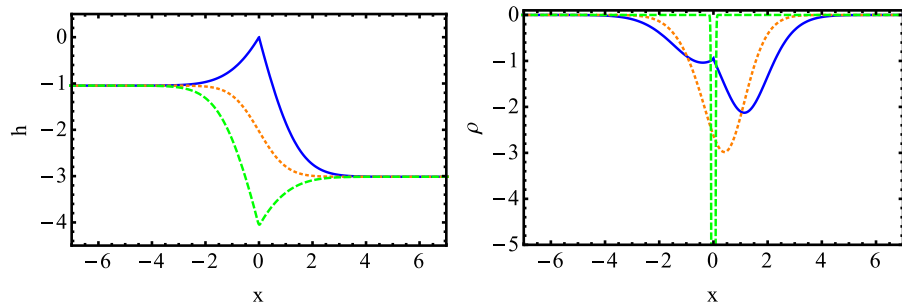


Figure 5.2: The optimal path for $\Lambda = -6.3$ computed numerically. Shown are h (top) and ρ (bottom) vs. x at $t = 0$ (solid line), 0.5 (short dash) and 1 (long dash).

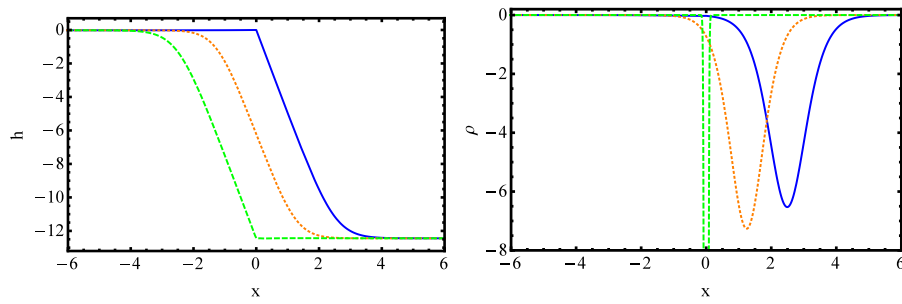


Figure 5.3: Same as in Fig. 5.2 but for $\Lambda = -10$.

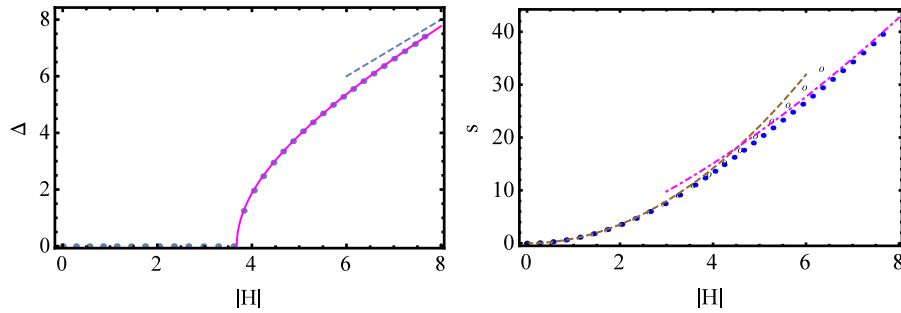


Figure 5.4: Top: Δ vs. $|H|$ at $H < 0$. Symbols: numerical results, solid line: Eq. (5.28), dashed line: the $|H| \gg 1$ asymptotic $|\Delta| = |H|$. Bottom: s vs. $|H|$ at $H < 0$: The asymmetric and symmetric branches are shown by the solid and empty symbols, respectively. Also shown are the small- and large- $|H|$ asymptotics of s .

results of the previous Section. For $|H| \geq |H_c|$ a good fit to the data is provided by

$$\Delta^2(H) = a(|H| - |H_c|) + b(|H| - |H_c|)^2, \quad (5.28)$$

with $H_c \simeq -3.7$, $a \simeq 10.6$ and $b \simeq 0.8$. This suggests a mean-field-like second-order transition, where the large deviation function s exhibits a discontinuity in its second derivative $\partial_H^2 s$ at $H = H_c$. One can recognize this discontinuity in the right panel of Fig. 5.4 which shows s vs. H for the asymmetric (solid symbols) and symmetric (empty symbols) solutions⁵. The corresponding values of s coincide at $|H| < |H_c|$ but start deviating from each other at $|H| > |H_c|$, the symmetric solution becoming non-optimal. The right panel also shows the small- H analytic result $s(H) = \sqrt{\pi}H^2/2$, and the large- $|H|$ analytic result (5.32) obtained below.

5.6 Negative- H tail

At very large negative H , or Λ , the asymmetric and symmetric solutions can be approximately found analytically. They involve narrow pulses of ρ , which we will call solitons, and ‘‘ramps’’ of h . The asymmetric solutions can be parameterized by the soliton/ramp

⁵ To obtain a converged symmetric solution, we artificially enforced symmetry at each iteration.

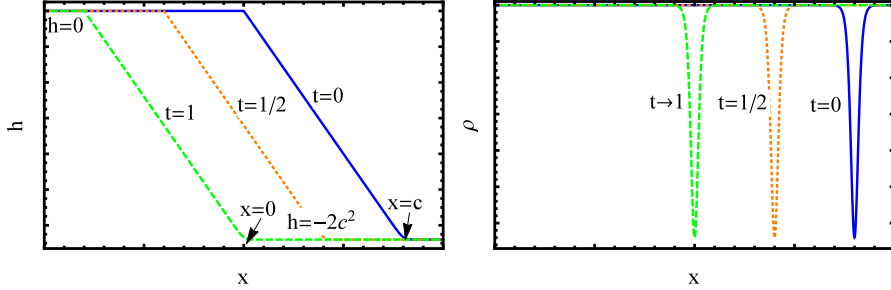


Figure 5.5: The optimal path, $h(x, t)$ and $\rho(x, t)$, for $H < 0$ and $|H| \gg 1$, see Eqs. (5.29)-(5.31), for $t = 0, 1/2$ and 1 .

speed $c \gg 1$. The left-moving solution can be written as

$$\rho(x, t) = -c^2 \operatorname{sech}^2 \left[\frac{c}{2} (ct + x - c) \right], \quad (5.29)$$

$$h(x, t) \simeq 2 \ln \left[1 + e^{c(ct+x-c)} \right] - 2c(ct + x) \quad (5.30)$$

for $x > -ct$, and

$$\rho(x, t) \simeq h(x, t) \simeq 0 \quad (5.31)$$

at $x < -ct$, see Fig. 5.5. The expressions for each of the two regions are exact solutions of Eqs. 5.5 and (5.6). The approximate combined solution obeys, up to exponentially small corrections, the boundary conditions (5.8) and (5.9). It is continuous (again, up to an exponentially small correction), but includes a shock in the interface slope $V(x, t) = \partial_x h(x, t)$ at $x = -ct$ ⁶. In our numerical solutions for large negative Λ , the ρ -soliton rapidly changes into the delta-function (5.7) at $t \rightarrow 1$ (as Fig. 5.3 indicates already for moderate negative Λ). This transient does not contribute to the action in the leading order in $|H| \gg 1$.

The conservation law $\int dx \rho(x, t) = \Lambda$ yields $c = -\Lambda/4$, and we obtain $s = s_{\text{dyn}} + s_{\text{in}} = 4c^3/3 + 4c^3 = (16/3)c^3$. Expressing c via H from the relation $|H| = 2c^2$ (see Fig. 5.5), we arrive at

$$s = \frac{4\sqrt{2}|H|^{3/2}}{3}. \quad (5.32)$$

⁶ The shock is a small price to pay for neglecting the diffusion. To get a smooth solution one can reintroduce the diffusion and match, in a joint applicability region, the solution (5.30) with an exact traveling wave solution of the *deterministic* KPZ equation that obeys $h(x = -\infty, t) = 0$, cf. Ref. [118].

In the physical units

$$-\ln \mathcal{P}(H, T) \simeq \frac{4\sqrt{2}\nu|H|^{3/2}}{3D|\lambda|^{1/2}T^{1/2}}, \quad (5.33)$$

in perfect agreement with the proper tail of the Baik-Rains distribution⁷ [111]. The latter has been known to describe the *late-time* one-point statistics of the KPZ interface for the stationary initial condition [109, 110]. As we see now, this tail holds at any $T > 0$.

The simplest among the *symmetric* solutions is a single stationary ρ -soliton and two outgoing h -ramps. These exact solutions were found earlier [115, 118, 119]. A family of more complicated exact two-soliton solutions involves two counter-propagating ρ -solitons that collide and merge into a single stationary soliton. Correspondingly, two counter-propagating h -ramps disappear upon collision and reemerge with the opposite signs, see Appendix A. Remarkably, the single-soliton and two-soliton solutions are particular members of a whole family of exact multi-soliton/multi-ramp solutions of Eqs. (5.5) and (5.6). We found them by performing the Cole-Hopf canonical transformation $Q = e^{-\frac{h}{2}}$, $P = -2\rho e^{\frac{h}{2}}$ and applying the Hirota method [128] to the transformed equations; see Appendix A for more details.

For all symmetric solutions the action s is twice as large as what Eq. (5.32) predicts, so they are not optimal. Notably, the corresponding non-optimal action s coincides with that describing the tail of the Tracy-Widom distribution [129]. This tail appears, at all times, for a class of *deterministic* initial conditions [118, 120, 119]. Therefore, fluctuations in the initial condition, intrinsic for the stationary interface, greatly enhance (by the factor of 2 in a large exponent) the negative tail of $\mathcal{P}(H)$.

⁷ To make the comparison, the Baik-Rains distribution $\mathcal{P}_{\text{BR}}(H, T)$ should be represented as $-\ln \mathcal{P}_{\text{BR}}(H, T) \simeq \Phi(H)/T^{1/2}$. The large deviation function $\Phi(H) = s(-2H)/8$, where s is our rescaled total action.

Chapter 6

Conclusion and Discussion

We shall close by surveying the methods and results of the previous chapters, with an eye towards possible future work.

In chapter 3.3.2 we developed semiclassical treatment for a family of non-Hermitian \mathcal{PT} -symmetric Hamiltonians which arose by mapping of 1D classical statistical mechanics of multi-valent Coulomb gases onto quantum mechanics. The low-energy spectra of the Hamiltonians directly translate into thermodynamic and adiabatic transport coefficients of the corresponding Coulomb gases.

To carry out the semiclassical method in a tractable manner, we made use methods of algebraic topology and Riemann surfaces. The main advantage of this strategy is that it allows us to avoid solving equations of motion and finding classical trajectories explicitly. The latter task is rather non-trivial (if at all attainable) in the 4D phase space. Instead, we argued that any surface of constant energy is a 2D Riemann surface with genus $g \geq 1$. The action along any closed trajectory (not necessarily satisfying equations of motion) may be written as an integer valued linear combination of $2g$ basic periods of the surface. The latter may be found as solutions of Picard-Fuchs ODE in the space of parameters. Finally, relations between basic periods and the quantum spectra are established by considering special points in the parameter space, where the surface degenerates into genus $g - 1$ singular surface. Consideration of monodromy transformations in a vicinity of these points allows us to identify classical actions, quantized according to Bohr-Sommerfeld, as well as the instanton action, which determines the bandwidth.

The results obtained this way were in excellent agreement with numerical simulations in a broad range of parameters. One of the reasons for this success is that the method provides with preexponential factors on the same footing with the exponent itself. Another appealing feature of the approach is that none of our semiclassical calculations required the concept of imaginary time. In fact "time" (i.e. 1D coordinate of the Coulomb gas) does not appear at all. In a sense it is substituted by evolution in the space of parameters of the Hamiltonian (moduli space).

Upon finishing this work, we wanted to apply our method to other problems involving instanton calculations in complex spaces. Our problem of interest became the topic of chapter 3, namely semiclassical calculations for large-spin systems in $SU(2)$. Here we made use of the same Riemann surface theory as in chapter 3.3.2 to again demonstrate that the necessary action integrals can be evaluated without explicitly knowing the trajectories that solve the equations of motion. The principal technical difference is that we needed to consider how simple poles, not just the periods, behaved under monodromy transformations near the critical values of the moduli where the Riemann surface is degenerate. This allowed us to obtain energy levels for the given Hamiltonian (3.1) and extend previous results for the level splitting to excited states with non-zero energy and an explicit proof that the oscillation period with the applied magnetic field does not change for higher levels and indeed extends to the full quantum mechanical result. The semiclassical results fit well with numerical simulations.

Having stated our successes in this regard, it is worth making note of some of the limitations. With the Coulomb gas system, we found that we could develop a Picard-Fuchs equation with energy as moduli parameter. This only succeeded, however, because the system could be characterized by a single fugacity. As such, our results were limited to systems consisting of exactly species each of cation and anion; considering more than this resulted in analytical obstacles that we could not progress beyond. Similarly, the multiplicity of parameters in SMM systems precluded a useful description via Picard-Fuchs equations, and made it difficult to carry out any analysis of the physically-relevant fourth-order anisotropy term. It is also worth noting that, in order to make what progress we did, we had to break the symmetry between z, \bar{z} in the action integral. A symmetric treatment seems more natural but ultimately eluded us.

After this work, the author left behind WKB-type analyses for a time in favor of

more generic asymptotic problems. This resulted in the work of chapter 4, where we considered the universal finite-size scaling of free energy in 1D lattice systems in the vicinity of a topological phase transition. In conformal field theories the N^{-1} term in energy is universal and only depends on the central charge of the Virasoro algebra[75, 76]. Here we find that in the case of topological phase transitions this term naturally extends into a scaling function, depending only on the ratio of the system size to the correlation length. Furthermore this scaling function is universal for all topologically non-trivial classes of non-interacting fermions in one spatial dimension. While the scaling function for energy appears to be sensitive to the topological nature of the transition, this is by no means the common situation. For example, the finite-size scaling function of the entanglement entropy away from the critical point[78], appears to be symmetric across the topological transition[79] (there is still an asymmetric size-independent boundary term).

It is natural to ask whether the scaling behavior changes with interactions, especially for models with central charge different from $c = 1$ and $c = 1/2$ considered here. Another direction to explore is relation of the scaling function to the theory of integrable systems[86]. In particular if it may be expressed in terms of solutions of Painleve equations, as it happens in e.g. the Ising model [77]. As mentioned above, the non-analytic contributions to the finite-size scaling near $w = 0$ are related to the monodromy, i.e. discontinuity across the branch cut terminating at $w = 0$, which happens to be simply a second order polynomial in w . An open question is if the full $f(w)$ -function may be recovered from the monodromy data, specified for all of its branch cuts, through the solution of a Riemann-Hilbert problem[85].

As the last project presented here, we return in chapter 5 to the realm of semiclassical analysis by considering the weak-noise theory of the KPZ equation. From that numerical analysis, we determined the tails of the short-time interface-height distribution in the KPZ equation when starting from a stationary interface. As shown, the $|H|^{3/2}/T^{1/2}$ tail of the Baik-Rains distribution, predicted by earlier authors to hold for long times, holds at all times. We argued (see also Refs. [118, 119]) that the other tail, $|H|^{5/2}/T^{1/2}$, also holds at long times once the condition $|H| \gg T$ is met.

A central result of this chapter is the discovery of a dynamical phase transition in the large deviation function of H at $T \rightarrow 0$. The transition occurs at $H = H_c \simeq 3.7 \nu/\lambda$ and

is caused by a spontaneous breaking of the reflection symmetry $x \leftrightarrow -x$ of the optimal path responsible for a given H . We provided numerical evidence that the transition is of the second order. Strictly speaking, the WNT only predicts a true phase transition at a single point $(H_c, 0)$ of the phase diagram (H, T) . At finite but short times the transition is smooth but sharp around H_c , and this sharp feature should be observable in stochastic simulations of the KPZ equation. One can characterize the transition by measuring the probability distribution of Δ (a random quantity)¹ at fixed H . This distribution is expected to change, in the vicinity of the critical value $H_c < 0$, from unimodal, centered at zero, to bimodal. At very large $|H|$ the bimodality peaks should approach $\Delta \simeq \pm H$.

As a postscript to this project, a subsequent publication of Krajenbrink and Le Doussal in 2017 [121] succeeded obtaining *exact* results for the short-time height distribution of the KPZ equation. In particular, they recovered the above phase transition that had been discovered by means of semiclassical approximation. This seems an appropriate note on which to end this thesis, as an instance of how semiclassical method provides a guide for both analytic theory and experimental discovery.

¹ In a stochastic system one can define $\Delta = h(X, 0) - h(-X, 0)$, where X can be chosen as $a\ell$, where ℓ is the characteristic lateral size of the optimal initial height profile, predicted by the WNT at given H , and a is a constant of order of unity. For large negative H , $\ell \simeq (\lambda HT)^{1/2}$ is the lateral size of the ramp, see the left panels of Figs. 5.3 and 5.5.

References

- [1] T. Gulden, M. Janas, P. Koroteev and A. Kamenev, Sov. Phys. JETP **117** 1 (2013), J. Exp. Theor. Fiz. **144** 9 (2013)
- [2] T. Gulden, M. Janas, and A. Kamenev, J. Phys. A: Math. Theor. **47** 085001 (2014).
- [3] T. Gulden, M. Janas, and A. Kamenev, J. Phys. A: Math. Theor. **48** 075304 (2015).
- [4] T. Gulden, M. Janas, Y. Wang, and A. Kamenev, Phys. Rev. Lett. **116** 026402 (2016).
- [5] M. Janas, A. Kamenev, and B. Meerson, Phys. Rev. E. **94** : 032133, (2016).
- [6] A. Kamenev, J. Zhang, A. I. Larkin, and B. Shklovskii, Physica A **359**, p. 129-161 (2006).
- [7] J. Zhang, A. Kamenev, and B. Shklovskii, Phys. Rev. E **73**, 051205 (2006).
- [8] J. Zhang, A. Kamenev, and B. Shklovskii, Phys. Rev. Lett. **95**, 148101 (2005).
- [9] R. MacKinnon, Angew. Chem., Int. Ed. **43**, 4265 (2004).
- [10] D.A. Doyle *et al.*, Science **280**, 69 (1998).
- [11] B. Roux, T. Allen, S. Berneche and W. Im, Q. Rev. Biophys. **37**, 15 (2004).
- [12] T.W. Allen, P.S. Andersen, and B. Roux, Proc. Natl. Acad. Sci. USA **101**, 117 (2004).
- [13] S.-H. Chung, and B. Corry, Eur. Phys. J. E **1**, 417 (2005).

- [14] A. M. Berezhkovskii, M. A. Pustovoit, and S. M. Bezrukov, J. Chem. Phys. **116**, 6216 (2002); **116**, 9952 (2002); **119**, 3943 (2003).
- [15] S.F. Edwards, and A. Lenard, J. Math. Phys. **3**, 778 (1962).
- [16] V. G. Vaks, A. I. Larkin, and S. A. Pikin, Sov. Phys. JETP **24**, 240 (1967).
- [17] N. Seiberg, and E. Witten, Nucl. Phys. B **426**, 19 (1994); [Erratum-ibid. B **430**, 485 (1994)].
- [18] N. Seiberg, and E. Witten, Nucl. Phys. B **431**, 484 (1994).
- [19] R. Donagi, and E. Witten, Nucl. Phys. B **460**, 299 (1996).
- [20] A. Gorsky, I. Krichever, A. Marshakov, A. Mironov, and A. Morozov, Phys. Lett. B **355**, 466 (1995).
- [21] A. Gorsky, *On the Properties of Complex Dynamical Systems*, unpublished.
- [22] C.E. Rüter, K.G. Makris, R. El-Ganainy, D.N. Christodoulides, M. Segev, and D. Kip, Nat. Phys. **6**, 192 (2010).
- [23] I. Rotter, J. Phys. A: Math. Theor. **42**, 153001 (2009).
- [24] D. L. Huber, and W. Y. Ching, Phys. Rev. B **47**, 3220 (1993).
- [25] J. C. Tully, and C. M. Truesdale, J. Chem. Phys. **65**, 1002 (1976).
- [26] A. Garg, E. Kochetov, K.-S. Park, and M. Stone, J. Math. Phys **44**, p. 48 (2003).
- [27] E. Kececioglu, and A. Garg, Phys. Rev. B **67**, 054406 (2003).
- [28] A. Altland, and B. Simons, *Condensed Matter Field Theory*, (Cambridge University Press, Cambridge UK 2007).
- [29] C. M. Bender, D. C. Brody, and H. F. Jones, Phys. Rev. Lett. **89**, 270401 (2002).
- [30] C. M. Bender, D. C. Brody, and H. F. Jones, Am. J. Phys. **71**, p. 1095-1102 (2003).
- [31] Y. N. Joglekar, and J. L. Barnett, Phys. Rev. A **84**, 024103 (2011).

- [32] J. N. L. Connor, T. Uzer, R. A. Marcus, and A. D. Smith, *J. Chem. Phys.* **80**, 10 (1984).
- [33] J. Meixner, and F.W. Schäfke, *Mathieusche Funktionen und Sphaeroidfunktionen mit Anwendungen auf Physikalische und Technische Probleme*, Springer, Berlin (1954).
- [34] R. Miranda, *Algebraic Curves and Riemann Surfaces*, American Mathematical Society, Providence RI (1995).
- [35] P. A. Griffiths, *Annals of Mathematics*, Second Series, **90**, 460 (1969).
- [36] P. Deligne, *Equations differentielles a points singuliers reguliers* (French), Lecture Notes in Mathematics, **163**, 133 (Springer-Verlag, Berlin-New York, 1970).
- [37] D. R. Morrison, In *Yau, S.T. (ed.): *Mirror symmetry I** 185-199 [hep-th/9111025].
- [38] G. Heckman, *Tsinghua Lectures on Hypergeometric Functions*. Retrieved from <http://www.math.ru.nl/~heckman/tsinghua.pdf> (2011).
- [39] M. Abramowitz, and I.A. Stegun, *Handbook of mathematical functions, with formulas, graphs, and mathematical tables*, Dover Publications, New York (1972).
- [40] W. Bühring and H. M. Srivastava. *Approx. theory and appls.* 17-35. Hadronic Press, Florida (1998).
- [41] L. Landau and E. Lifshitz. *Quantum Mechanics: non-relativistic theory*, Pergamon Press, New York (1977).
- [42] A. Garg, E. Kochetov, K.-S. Park and M. Stone, *Jour. of Math. Phys.* **44** 1 (2003).
- [43] E. Kochetov, *Jour. of Math. Phys.* **36** 4667 (1995).
- [44] A. Garg and M. Stone, *Phys. Rev. Lett.* **92** 1 (2004).
- [45] M. Stone and K.-S. Park and A. Garg, *Jour. of Math. Phys.* **41** 12 (2000).
- [46] W.G. Harter and C.W. Patterson, *J. Chem. Phys.* **80** 4241 (1984).
- [47] W.G. Harter. *Computer Physics Reports* **8** p. 319-394 (1988).

- [48] E. Keçecioglu and A. Garg, Phys. Rev. Lett. **88** 237205 (2002).
- [49] M. Wilkinson and E.J. Austin, J. Phys. A: Math. Gen. **23** 2529 (1990).
- [50] N. Seiberg and E. Witten, Nucl. Phys. B **426** 19 (1994), Erratum-ibid. **430**, 485 (1994).
- [51] N. Seiberg and E. Witten, Nucl. Phys. B, **431** 484 (1994).
- [52] J. Liu, E. del Barco and S. Hill. *A microscopic and spectroscopic view of quantum tunneling of magnetization*, in *Molecular Magnets: Physics and Applications*, ed: *J. Bartolome, F. Luis and J. F. Fernandez*, **12** p. 77-110 (2014).
- [53] E. del Barco, A. D. Kent, S. Hill, J. M. North, N. S. Dalal, E. M. Rumberger, D. N. Hendrickson, N. Chakov and G. Christou, Jour. of Low Temp. Phys. **140** p. 119-174 (2005).
- [54] D. A. Garanin and E. M. Chudnovsky, Phys. Rev. B **56** 17 (1997).
- [55] D. Gatteschi, R. Sessoli and A. Cornia, Chem. Commun. p. 725-732 (2000).
- [56] W. Wernsdorfer and R. Sessoli, Science **284** 133 (1999).
- [57] A.-L. Barra, P. Debrunner, D. Gatteschi, C. E. Schulz and R. Sessoli, Europhys. Lett. **35** p. 133-138 (1996).
- [58] C. Sangregorio, T. Ohm, C. Paulsen, R. Sessoli and D. Gatteschi, Phys. Rev. Lett. **78** 24 (1997).
- [59] A. Garg, Phys. Rev. B **60** 9 (1999).
- [60] Y. N. Joglekar and D. Scott and M. Babey and A. Saxena. Phys. Rev. A **82** 030103(R) (2010).
- [61] A. Nanayakkara. J. Phys. A: Math. Gen. **37** 4321-4334 (2004).
- [62] C. Bender and J.-H. Chen and D. Darg and K. Milton. J. Phys. A: Math. Gen. **39** p. 4219-4238 (2006).
- [63] C. L. Kane, and E. J. Mele, Phys. Rev. Lett. **95**, 146802 (2005).

- [64] M. Z. Hasan, and C. L. Kane, Rev. Mod. Phys. **82**, 3045 (2010).
- [65] J. Moore, Nat. Phys. **5**, 378 (2009).
- [66] X.-L. Qi, and S.-C. Zhang, Rev. Mod. Phys. **83**, 1057 (2011).
- [67] A. Altland, and M. R. Zirnbauer, Phys. Rev. B **55**, 1142 (1997).
- [68] S. Ryu, A. P. Schnyder, A. Furusaki, and A. W. W. Ludwig, New Jour. Phys. **12**, 065010 (2010).
- [69] M. Stone, C. K. Chiu, and A. Roy, J. Phys. A: Math. Theor. **44**, 045001 (2011).
- [70] M. König, S. Wiedmann, C. Brüne, A. Roth, H. Buhmann, L. W. Molenkamp, X.-L. Qi, and S.-C. Zhang, Science **318**, 5851 (2007).
- [71] H. Zhang, C.-X. Liu, X.-L. Qi, X. Dai, Z. Fang, and S.-C. Zhang, Nat. Phys. **5**, 438 (2009).
- [72] A. Das, Y. Ronen, Y. Most, Y. Oreg, M. Heiblum, and H. Shtrikman, Nat. Phys. **8**, 887 (2012).
- [73] S.-Y. Xu, I. Belopolski, N. Alidoust, M. Neupane, G. Bian, C. Zhang, R. Sankar, G. Chang, Z. Yuan, C.-C. Lee, S.-M. Huang, H. Zheng, J. Ma, D. S. Sanchez, B. Wang, A. Bansil, F. Chou, P. P. Shibayev, H. Lin, S. Jia, and M. Z. Hasan, Science **349**, 6248 (2015).
- [74] P. di Francesco, P. Mathieu, and D. Senechal, "Conformal Field Theory", Springer, New York (1997).
- [75] H. W. J. Blöte, J. L. Cardy, and M. P. Nightingale, Phys. Rev. Lett. **56**, 742 (1986).
- [76] I. Affleck, Phys. Rev. Lett. **56**, 746 (1986).
- [77] T.T. Wu, B.M McCoy, C.A.Tracy and E. Barouch, Phys. Rev. B **13**, 316 (1976); B. M. McCoy, Internat. Ser. Monogr. Phys. **146**, Oxford Science Publications (2010).
- [78] P. Calabrese, and J. Cardy, J. Stat. Mech: Theor. Exp., P06002 (2004).
- [79] T. Gulden, M. Janas, Y. Wang, and A. Kamenev, unpublished.

- [80] W. P. Su, J. R. Schrieffer, and A. J. Heeger, Phys. Rev. Lett. **42**, 1698 (1979).
- [81] A. J. Heeger, S. Kivelson, J. R. Schrieffer, and W. -P. Su, Rev. Mod. Phys. **60**, 781 (1988).
- [82] A. Y. Kitaev, Phys.-Usp. **44**, 131 (2001).
- [83] J. Alicea, Rep. Prog. Phys. **75**, 076501 (2012).
- [84] A. Schnyder, Lectures at Nancy summer school (2014).
- [85] H. Zoladek, "The monodromy group", Birkhäuser, Basel-Boston-Berlin (2006).
- [86] G. M. D'Ariano, A. Montorsi, and M. G. Rasetti, "Integrable Systems in Statistical Mechanics", Series on Advances in Statistical Mechanics Volume 1, World Scientific Publishing, Singapore (1985).
- [87] R. Graham and T. Tél, Phys. Rev. A **31**, 1109 (1985).
- [88] H.R. Jauslin, Physica A **144**, 179 (1987).
- [89] M.I. Dykman, M.M. Millonas, and V.N. Smelyanskiy, Phys. Lett. A **195**, 53 (1994).
- [90] B. Derrida, J. Stat. Mech. (2007) P07023.
- [91] H. Touchette, Phys. Rep. **478**, 1 (2009).
- [92] L. Bertini, A. De Sole, D. Gabrielli, G. Jona-Lasinio, and C. Landim, Rev. Mod. Phys. **87**, 593 (2015).
- [93] L. Bertini, A. De Sole, D. Gabrielli, G. Jona-Lasinio, and C. Landim, J. Stat. Phys. 123, 237 (2006), T. Bodineau and B. Derrida, Phys. Rev. E **72**, 066110 (2005); C. R. Phys. 8, 540 (2007); P. I. Hurtado and P. L. Garrido, Phys. Rev. Lett. **107**, 180601 (2011); L. Zarfaty and B. Meerson, J. Stat. Mech. (2016), 033304.
- [94] L. Bertini, A. De Sole, D. Gabrielli, G. Jona-Lasinio, and C. Landim, J. Stat. Mech (2010), L11001.
- [95] Y. Baek and Y. Kafri, J. Stat. Mech. (2015) P08026.

- [96] H. Spohn, *Large Scale Dynamics of Interacting Particles* (Springer-Verlag, New York, 1991).
- [97] T. M. Liggett, *Stochastic Interacting Systems: Contact, Voter, and Exclusion Processes* (Springer, New York, 1999).
- [98] C. Kipnis and C. Landim, *Scaling Limits of Interacting Particle Systems* (Springer, New York, 1999).
- [99] M. Kardar, G. Parisi, and Y.-C. Zhang, Phys. Rev. Lett. **56**, 889 (1986).
- [100] T. Halpin-Healy and Y.-C. Zhang, Phys. Reports **254**, 215 (1995).
- [101] A.-L. Barabasi and H. E. Stanley, *Fractal Concepts in Surface Growth* (Cambridge University Press, Cambridge, UK, 1995).
- [102] J. Krug, Adv. Phys. **46**, 139 (1997).
- [103] I. Corwin, Random Matrices: Theory Appl. **1**, 1130001 (2012).
- [104] J. Quastel and H. Spohn, J. Stat. Phys. **160**, 965 (2015).
- [105] T. Halpin-Healy and K. A. Takeuchi, J. Stat. Phys. **160**, 794 (2015).
- [106] H. Spohn, arXiv:1601.00499.
- [107] W. M. Tong and R.W. Williams, Annu. Rev. Phys. Chem. **45**, 401 (1994); L. Miettinen, M. Myllys, J. Merikoski, and J. Timonen, Eur. Phys. J. B **46**, 55 (2005), M. Degawa, T. J. Stasevich, W. G. Cullen, A. Pimpinelli, T. L. Einstein, and E. D. Williams, Phys. Rev. Lett. **97**, 080601 (2006).
- [108] K.A. Takeuchi and M. Sano, Phys. Rev. Lett. **104**, 230601 (2010); J. Stat. Phys. **147**, 853–890 (2012), K. Takeuchi, M. Sano, T. Sasamoto, and H. Spohn, Sci. Rep. **1**, 34 (2011); K. A. Takeuchi, Phys. Rev. Lett. **110**, 210604 (2013); T. Halpin-Healy and Y. Lin, Phys. Rev. E **89**, 010103R (2014).
- [109] T. Imamura and T. Sasamoto, Phys. Rev. Lett. **108**, 190603 (2012); J. Stat. Phys. **150**, 908 (2013).

- [110] A. Borodin, I. Corwin, P.L. Ferrari, and B. Vető, Mathematical Physics, Analysis and Geometry **18**, 1 (2015).
- [111] J. Baik and E.M. Rains, J. Stat. Phys. **100**, 523 (2000).
- [112] H.C. Fogedby, Phys. Rev. E **57**, 4943 (1998).
- [113] H.C. Fogedby, Phys. Rev. E **59**, 5065 (1999).
- [114] H.C. Fogedby and W. Ren, Phys. Rev. E **80**, 041116 (2009).
- [115] I. V. Kolokolov and S. E. Korshunov, Phys. Rev. B **75**, 140201(R) (2007).
- [116] I. V. Kolokolov and S. E. Korshunov, Phys. Rev. B **78**, 024206 (2008).
- [117] I. V. Kolokolov and S. E. Korshunov, Phys. Rev. B **80**, 031107 (2009).
- [118] B. Meerson, E. Katzav, and A. Vilenkin, Phys. Rev. Lett. **116**, 070601 (2016).
- [119] A. Kamenev, B. Meerson and P.V. Sasorov, Phys. Rev. E **94**, 032108 (2016).
- [120] P. Le Doussal, S. N. Majumdar, A. Rosso, and G. Schehr, Phys. Rev. Lett. **117**, 070403 (2016).
- [121] A. Krajenbrink and P. Le Doussal, Phys. Rev. E **96** 020102 (2017).
- [122] B. Derrida and A. Gerschenfeld, J. Stat. Phys. **137**, 978 (2009).
- [123] P.L. Krapivsky and B. Meerson, Phys. Rev. E **86**, 031106 (2012).
- [124] S. Edwards and D. Wilkinson, Proc. R. Soc. Lond. A **381** 17 (1982).
- [125] J. Krug, P. Meakin and T. Halpin-Healy, Phys. Rev. A **45**, 638 (1992).
- [126] A. I. Chernykh and M. G. Stepanov, Phys. Rev. E **64**, 026306 (2001).
- [127] V. Elgart and A. Kamenev, Phys. Rev. E **70**, 041106 (2004).
- [128] R. Hirota, Phys. Rev. Lett. **27**, 1192 (1971). For a useful review see J. Hietarinta, Physics AUC **15**, 31 (2005).
- [129] C. A. Tracy and H. Widom, Comm. Math. Phys. **159**, 174 (1994).

- [130] T. Sasamoto, H. Spohn, Phys. Rev. Lett. **104**, 230602 (2010).
- [131] P. Calabrese, P. Le Doussal, A. Rosso, Europhys. Lett. **90**, 20002 (2010).
- [132] V. Dotsenko, Europhys. Lett. **90**, 20003 (2010).
- [133] G. Amir, I. Corwin, and J. Quastel, Comm. Pur. Appl. Math. **64**, 466 (2011).
- [134] A.B. Shabat, V.E. Adler, V.G. Marikhin, and V.V. Sokolov (Eds.), *Encyclopedia of Integrable Systems*, L.D. Landau Institute for Theoretical Physics, 2010 (<http://home.itp.ac.ru/~adler/E/e.pdf>), p. 303.
- [135] G. B. Whitham, *Linear and Nonlinear Waves* (Wiley, New York, USA, 1974).
- [136] M. Hairer, Annals of Math. **178**, 559 (2013).

Appendix A

Cole-Hopf transformation, kinks, solitons and ramps

As explained in Chapter 5, the optimal path at very large negative H can be approximately described in terms of a ρ -soliton and h -ramp. As we show here, this solution is a particular member of a whole family of exact multi-soliton/multi-ramp solutions of the WNT equations. Let us perform a canonical Cole-Hopf transformation from h and ρ to Q and P according to

$$Q = e^{-\frac{h}{2}}, \quad P = -2\rho e^{\frac{h}{2}}. \quad (\text{A.1})$$

The inverse transformation is $h = -2 \ln Q$ and $\rho = -(1/2)QP$. In the new variables the Hamilton equations,

$$\partial_t Q = \partial_x^2 Q + \frac{1}{4} Q^2 P, \quad (\text{A.2})$$

$$\partial_t P = -\partial_x^2 P - \frac{1}{4} Q P^2, \quad (\text{A.3})$$

have a symmetric structure and appear in “Encyclopedia of Integrable Systems” [134]. In this work we do not pursue the complete integrability aspects and limit ourselves to exact multi-kink solutions which we found using the Hirota method [128]. The multi-kink solutions in terms of Q and P become multi-soliton and multi-ramp solutions in

terms of ρ and h , respectively. The Hirota ansatz

$$Q = \frac{v}{u}, \quad P = \frac{w}{u},$$

transforms Eqs. (A.2) and (A.3) into the following form:

$$\begin{aligned} (D_t - D_x^2)(v \cdot u) &= 0, \\ (D_t + D_x^2)(w \cdot u) &= 0, \\ D_x^2(u \cdot u) &= \frac{1}{4}vw, \end{aligned} \tag{A.4}$$

where $D_t(A \cdot B) = A_tB - AB_t$ and $D_x^2(A \cdot B) = A_{xx}B - 2A_xB_x + AB_{xx}$ are the Hirota derivatives. Equations (A.4) admit two families of N -kink solutions:

$$\begin{aligned} u &= \sum_{i=1}^N \eta_i^{(+)}, \\ v &= \frac{1}{C} \sum_{i,j=1}^N (c_i - c_j)^2 \eta_i^{(+)} \eta_j^{(+)}, \\ w &= 4C, \end{aligned} \tag{A.5}$$

and

$$\begin{aligned} u &= \sum_{i=1}^N \eta_i^{(-)}, \\ v &= 4C, \\ w &= \frac{1}{C} \sum_{i,j=1}^N (c_i - c_j)^2 \eta_i^{(-)} \eta_j^{(-)}, \end{aligned} \tag{A.6}$$

where $\eta_i^{(\pm)}(x, t) = e^{\pm c_i^2 t - c_i(x - X_i)}$, the kinks are parametrized by N velocities c_i and N initial coordinates X_i , $i = 1, \dots, N$, and C is an arbitrary constant, reflecting invariance of the original WNT equations (5.5) and (5.6) with respect to an arbitrary shift of h .

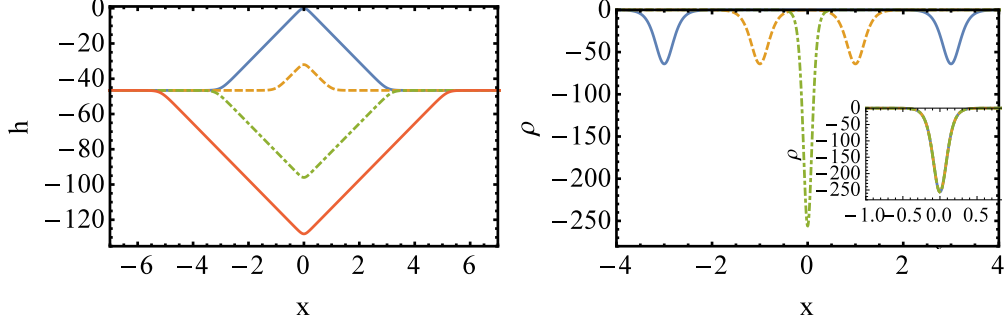


Figure A.1: Example of exact two-ramp/two-soliton solutions (A.7) and (A.7) for $h(x, t)$ and $\rho(x, t)$, respectively. Shown (for $c = 8$) are h and ρ versus x for $N = 3, c_1 = X_1 = 0, c_3 = -c_2 = c$ and $X_3 = -X_2 = -(3/8)c$. Top panel: $t = 0$ (solid), $1/4$ (dashed), $3/4$ (dash-dotted) and 1 (solid). Bottom panel: $t = 0$ (solid), $1/4$ (dashed) and 1 (dash-dotted). Inset: ρ versus x at $t = 1/2, 4/5$ and 1 . At $c \gg 1$ and $t > \tau$, ρ approaches the exact stationary one-soliton solution [112, 115, 118].

For the family of solutions (A.5) we obtain

$$h(x, t) = 2 \ln \left[\frac{C \sum_{i=1}^N e^{c_i(c_i t - x + X_i)}}{\sum_{i,j=1}^N (c_i - c_j)^2 e^{c_i(c_i t - x + X_i) + c_j(c_j t - x + X_j)}} \right],$$

$$\rho(x, t) = -\frac{2 \sum_{i,j=1}^N (c_i - c_j)^2 e^{c_i(c_i t - x + X_i) + c_j(c_j t - x + X_j)}}{\left[\sum_{i=1}^N e^{c_i(c_i t - x + X_i)} \right]^2}.$$

The particular case of $N = 3, c_1 = X_1 = 0, c_3 = -c_2 = c$ and $X_3 = -X_2 = -c\tau$, where $0 < \tau < 1$, yields the family of symmetric solutions described in the context of large negative H in Section 5.6. Here two identical counter-propagating ρ -solitons collide and merge, at $x = 0$, into a single soliton. The two ramps of h also merge, but then change their signs and expand, see Figs. A.1 and A.2. At $c \gg 1$ these solutions approximately satisfy all the boundary conditions. The arbitrary constant C can be chosen so as to impose the condition $h(x = 0, t = 0) = 0$. However, for all these symmetric solutions (at fixed c and different τ) the total action S , in the leading order, is the same and *twice as large* as S for the asymmetric solution, described in Chapter 5. Therefore, neither

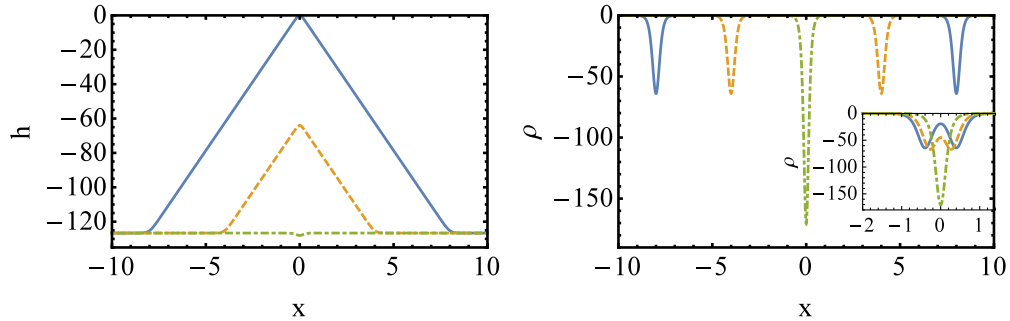


Figure A.2: Same as in Fig. A.1 but for $X_3 = -X_2 = -c$ (that is, $\tau = 1$) and $t = 0$ (solid), $1/2$ (dashed) and 1 (dash-dotted). The inset shows a blowup of the collision and merger of the two solitons at $t = 0.95, 0.965$ and 1 .

of these solutions is optimal. Finally, the single stationary ρ -soliton, and the expanding ramps, observed at $t > \tau$ is by itself an exact solution of the WNT equations, as was previously known [112, 115, 118]. This solution corresponds to $\tau = 0$ and represents the true optimal path for a whole class of *deterministic* initial conditions [119].